Theses and Dissertations

Spring 2022

Characterization of Nonequilibrium Plasma Discharge in High Water Vapor Concentration

Malik Mohammad Tahiyat

CHARACTERIZATION OF NONEQUILIBRIUM PLASMA DISCHARGE IN HIGH
WATER VAPOR CONCENTRATION

by

Malik Mohammad Tahiyat

Bachelor of Technology
West Bengal University of Technology, 2011

Master of Science
Bangladesh University of Engineering and Technology, 2015

_____

Submitted in Partial Fulfillment of the Requirements

For the Degree of Doctor of Philosophy in

Mechanical Engineering

College of Engineering and Computing

University of South Carolina

2022

Accepted by:

Tanvir I Farouk, Major Professor

Jamil A Khan, Committee Member

Sang Hee Won, Committee Member

Shamia Hoque, Committee Member

Tracey L. Weldon, Interim Vice Provost and Dean of the Graduate School

DEDICATION

This dissertation is dedicated to all the taxpayers of Bangladesh and the United States of America, whose support in the form of scholarships, teaching, and research assistantships played a momentous role in contributing to the tuition expenses for my Master of Science and Doctor of Philosophy.

ACKNOWLEDGEMENTS

The author would like to express his sincere gratitude to all the researchers, colleagues, lab members, and staff whose every contribution was of insurmountable importance in the course of this Ph.D. dissertation.

I would like to start by acknowledging the help and support from my colleagues at the "ReActing Systems and Advanced Energy Research" (RASAER) Lab in both past and present, whose unwavering assistance made this Ph.D. journey much easier to access. My heartiest thanks go to Drs. Rajib Mahamud, Fahd Alam, Farhan Ahmed, Ali Charchi, Mr. Sudipta Saha, Mr. Ejaz Ahmed, and Mr. Ebrahim Bhuiyan for their continuous guidance and support both at and outside academics. I am also indebted to the support from my undergraduate assistants in the completion of this dissertation: Damon Eddy, Gregory Belk, Isaac Yaghi, John Hill and Nathan Ramanjulu had put commendable efforts into the completion of this dissertation. I would also like to mention the graduate assistants at the collaborating research groups, namely, Ayuob Al Wahaibi, Seungjae Lim, Ackmer Robinson, Dahae Seong, and Ibrahim Sarikaya, who have been of utmost support in accomplishment in several of the endeavors in this Ph.D. research.

I offer my sincerest appreciation to the individuals at the several different machine shops who were instrumental in the fabrication of the in-house designed plasma reactors: Bill Bradley and Kyle George at the Mechanical Engineering Machine Shop, Allen Frye at Mechanical Prototype Facility, and Tom Lockart at One Ear Cow Glass.

v

ABSTRACT

In recent years, plasma discharge in liquid medium has been a topic of immense interest. Theoretical efforts have been pursued to obtain insight on physicochemical processes being influenced due to trace water vapor either being present as residual or provided at a known concentration. However, studies on discharge at high vapor content are limited. In this study, discharge characteristics of plasma in high water concentration (> 90%) are investigated experimentally for a pressure range of 1 – 15 Torr to maximize vapor loading without condensation. Voltage-current characteristics were obtained over 0-14 mA of current for each operating pressure; current density was determined to ensure a "normal" glow regime of operation. Spatially resolved optical emission spectroscopy was also conducted to determine OH, O, H_2, and H distribution in the interelectrode separation. The normalized intensities of OH and O emission lines are found to be more prominent in the positive column, whereas the emission lines of H are most intense in the cathode glow region. The electric field distribution along the discharge gap was also measured. We envision that the data obtained from this characterization study will provide valuable data for the validation of plasma kinetic schemes associated with water vapor.

In a continuation in the form of an application, a methodology involving plasma optical emission spectroscopy driven by a direct current plasma source is developed to quantify water vapor concentration in a gaseous stream. The experimental setup consists of a dc driven low-pressure plasma cell in which the emission from the plasma discharge is measured by an optical emission spectrometer. The emission from H_α at 656.2 nm – the first transition in the Balmer series was found to be the most sensitive to the water vapor concentration in the gas stream. Consistent linear trends of the emission signals with

respect to variation in concentration of water are observed for multiple combinations of operating parameters. This method has been applied to a vacuum drying process of a mock nuclear fuel assembly to quantify the concentration of water vapor during the drying process.

The third part of this dissertation tried to deduce the effect of water vapor on dc nitrogen plasma stratification. In general, plasma stratification has been studied for more than a century. Despite the many experimental studies reported on this topic, theoretical analyses and numerical modeling of this phenomenon have been mostly limited to rare gases. In this work, a one-dimensional fluid model with detailed kinetics of electrons and vibrationally excited molecules is employed to simulate moderate-pressure (i.e., a few Torr) dc discharge in nitrogen in a 15.5 cm long tube of radius 0.55 cm. The model also considers ambipolar diffusion to account for the radial loss of ions and electrons to the wall. The proposed model predicts self-excited standing striations in nitrogen for a range of discharge currents. The impact of electron transport parameters and reaction rates obtained from a solution of local two-term and a multi-term Boltzmann equation on the predictions are assessed. In-depth kinetic analysis indicates that the striations result from the undulations in electron temperature caused due to the interaction between ionization and vibrational reactions. Furthermore, the vibrationally excited molecules associated with the lower energy levels are found to influence nitrogen plasma stratification and the striation pattern strongly. A balance between ionization processes and electron energy transport allows the formation of the observed standing striations. Simulations were conducted for a range of discharge current densities from ~0.018 to 0.080 mA cm^{-2}, for an operating pressure of 0.7 Torr. Parametric studies show that the striation length increases

linearly with increasing tube radius but decreases in a non-linear fashion with increasing discharge current. The predictions from the model are compared against experimental measurements and are found to agree favorably.

The fourth part of this dissertation studies an application, which employs atmospheric pressure dielectric barrier discharge operating in moisture saturated continuous airflow as the discharge medium as a prospective method for bacterial disinfection from soft surfaces. The effect on two different strains of bacteria: *E. coli* and *B. atrophaeus* and for three different media for plasma discharge: static, airflow, moisture-saturated airflow was explored. Optical emission spectroscopy showed the generation of OH and reactive nitrogen species in the inter-electrode spacing between the dielectric and substrate for discharge in saturated air. The oxidizing ability of OH and H_2O_2 is primarily responsible for improved disinfection. The acidity of the agar medium was analyzed after a treatment duration of 25 mins. It was seen that for the case of moisture saturated air as the discharge medium, the pH change was observed for the longest radial distance from the point of influx. Compared to static conditions, the bacterial load reduction efficiency in moisture saturated air was found to be ~1.5 and ~2.5 times higher for *E. coli* and *B. atrophaeus,* respectively.

In the final segment of this dissertation, pulsed dielectric barrier discharge in He-H_2O and He- H_2O-O_2 mixture has been studied in near atmospheric conditions using time and spatially resolved photo fragmentation laser-induced fluorescence. The primary goals were to detect and quantify hydroxyl radicals and hydrogen peroxide produced in the 2-D discharge plane between the dielectric and the ground. The gas temperature was also measured via fluorescence spectroscopy of OH (A-X) rotational states and is found to be

bounded in the range of 275-300 K. The OH LIF signal is acquired from LIF (using 282 nm laser) whereas LIF from OH generated solely from H_2O_2 is measured by subtracting the OH LIF signal from the PFLIF signal (using 213 nm+ 282 nm lasers). A known concentration of H_2O_2 in He was used to calibrate for H_2O_2 whereas the OH was calibrated with a kinetic model. It is observed that for both gas mixtures, there is a gradual decay of both OH and H_2O_2 in the afterglow of the discharge. Furthermore, H_2O_2 has a prolonged existence in the afterglow (> 10 ms) compared to OH radicals, whose fluorescence signals cannot be traced after ~3 ms in the case of pure He. This may indicate that the primary sink route for OH radicals may be recombination reactions, whereas, for H_2O_2, it is the ambipolar and the convective losses since, unlike OH, H_2O_2 is not an active free radical. The addition of 5% O_2 in the He admixture increases the fluorescence intensity of both OH and H_2O_2 in the afterglow, signifying the more dissociative recombination reactions involving H, OH, and O radicals produced in the discharge compared to the case without added O_2.

PREFACE

This dissertation reports both qualitative and quantitative analyses of plasma containing high water vapor content. Some of the results from this dissertation have been published in several journals. Chapters 2 and 3 have been published in Review of Scientific Instruments and Journal of Physics D: Applied Physics, respectively. All necessary permissions have been obtained from the respective journals to include the published work in this dissertation.

Each chapter starts with its introduction. An overall introduction is included in Chapter 1 to acquaint the reader with the scope of this dissertation.

TABLE OF CONTENTS

LIST OF TABLES

LIST OF FIGURES

CHAPTER 1 :

INTRODUCTION

1.1 PLASMAS

'Plasmas' are called the fourth state of matter. In literal terms, the word *'Plasma'* means 'moldable substance' or 'jelly'. The name was first coined by Irving Langmuir in 1930. Langmuir first came across 'plasma' when he was investigating interferences in radio waves in the ionosphere.

Plasmas can have charge separation, but the sum of all charges should be neutral; any interaction with plasma will involve a collective effect. The 'collective effect' of the plasma can be construed by a thought experiment: if some isolated electrons and positive charges are moving randomly in a large vacant space and a unidirectional electric field ($\vec{E}$), the isolated electrons would be attracted to the $\vec{E}$, whereas the positive charges would be repelled. But if both the electrons and the positive have large number densities, the application of $\vec{E}$ may be negated or reduced due to the electric field generated among the charges themselves. In such cases, the ensemble of charges may be called 'plasma'. It is theorized that more than 99% of our physical universe comprises plasma, mostly in the form of interstellar ionized gases.

Plasmas exist in two primary forms: thermal (or equilibrium) and non-thermal (or nonequilibrium). Thermal plasmas are those, in which both the electrons and the ions are in temperatures higher than 1 eV (or 11,600 K). In other words, both the electrons and the ions are in thermal and chemical equilibrium with each other. Nonequilibrium plasmas are those in which the electron temperature is much 'hotter', i.e., greater than or in the vicinity of 1 eV, whereas the ion temperature is close to that of ambient temperature. Nonequilibrium plasmas are formed primarily due to the application of an electric field [1].

Due to its 'nonthermal' nature, this kind of plasma finds various applications in laboratory research and the industry. In nonequilibrium plasmas, ionization is achieved by the application of an electric field accelerating electrons and the resulting energetic electrons bombarding residual atoms to create charged species. Thus, ionization is achieved at a much 'cooler' temperature than 'thermal' plasmas and the low-temperature kinetics is also different from the 'thermal' kinetics as well [2].

1.2 LITERATURE REVIEW ON PLASMA IN LIQUIDS

Since the start of the new millennium, there has been a renewed surge in research interest in plasma-liquid interactions. Some of the industrial applications of plasma in liquids can be found in chemical synthesis, agriculture, plasma medicine, and materials synthesis [3]. But even after such a multitude of existing applications, fundamental understanding of these processes is hindered by several complexities. Some of the major complexities have been mentioned in the 2018 review of plasma physics of liquids [3]. Different plasma reactors operate in different regimes due to the difference in the plasma source itself and also since each plasma reactor is configured uniquely: direct discharge between electrodes, gas flow from one of the electrodes forming bubble-discharge, using liquid itself as one of the electrodes and many more. Thus, the reaction mechanisms of each of the reactor configurations can be vastly different. Additionally, plasma properties can be affected by physical and chemical changes to the discharge medium arising from the prolonged operation which includes an increase in the concentration of any of the active species.

There is considerable debate over the topic of plasma initiation in liquid medium for two theories [4]: either plasmas are initiated due to ionization mechanisms in the liquid

phase (like direct impact ionization, Auger effect, etc.) or due to breakdown mechanism in low density regions (microbubbles) formed due to electric field or localized Joule heating [3, 5]. Both theories are almost of the same level of credence. Additionally, the mechanism of plasma propagation post discharge is also vastly unexplored.

Plasma discharge in liquids often appeared in the form of streamers [6]. These discharge streamers supposedly originate from local thermodynamic equilibrium either in liquid or due to electron avalanches in successive bubbles [4]. Breakdown in liquids are sometimes explained by assuming that the thermodynamic properties of liquids are the same as that of a dense gas [7], however, recently this theory has been challenged as some electronic, optical, and thermodynamic properties of liquids resembled more to that of a semiconductor solid [8]. Phenomena like ionization in liquids can be modeled as the excitation of electrons from the valence shell to the conduction shell of a semiconductor atom and then accelerated by the electric field. However, while these assumptions work for short-time scales, on longer scales, properties like diffusion, drift, and evaporation might contribute to the difference between the two models [3, 9]. Additionally, the theory of solvated electrons and bubble-initiation mechanism will also not apply to the semiconductor/solid model assumption.

Currently, dielectric barrier discharge (DBD) reactors have widespread applications in plasma medicine and water treatment owing to their scalability, and ability to generate active species over a large area. However, the fundamentals of ionization wave propagation and discharge structure formation in DBD over water surface as the cathode are very less known [3, 10-13]. One of the most difficult parameters to deduce for plasma modeling that applies to both DBD and glow discharge is discerning the secondary electron

mission coefficient (γ). Unlike for metal surfaces, ion-induced γ at water cathode in glow discharge occurs is theorized to occur in multiple steps [14]: ion bombardment creating a solvated electron, solvated electron, and H_3O^+ recombination to release H, this H then diffusing to the cathode in the gas phase and then getting ionized to release a secondary electron. However, diffusion, being a slow process, sheds doubt on this model. Another mechanism postulates that the electrons are released from the anions near the cathode which is a comparatively faster process [15]. Nevertheless, the model fidelity will suffer for ionic and dielectric liquids [16] and also since these models also account for the following: conductivity, solvated electrons at the liquid surface [17], and surface charge accumulation [3].

In presence of liquid in 'mist' or 'spray' forms, plasma liquid interactions at the interface can be a vastly turbulent zone of bombardment reactions by electron-impact and heavy particle and charge transfer reactions as well as strong transport effects. All of these processes contribute to the heat and mass transfer in the discharge volume [4]. While H_2O molecule being electronegative can act as an electron scavenger[18] and thus increase breakdown potential, an opposing effect results from other processes like electron detachment, secondary electron emission from negative ions, charge transfer reactions [19], and enhanced localized electric field near droplets. However, there are still a lot of unknown phenomena to investigate in plasma processes in contact with mist including if there is any possibility of nanobubble formation [20, 21] that might explain some of the observed dynamics.

Despite all the challenges that have been described in the preceding paragraphs, the most significant obstacles since the last decade may have been the diagnosis of the

chemical kinetics that govern the initiation and supporting mechanisms of the discharge along with a comprehensive study of the species that are produced in these discharges. Additional difficulties also arise when it is further needed to deduce the gas phase ion and electron emission mechanisms.

One of the most important active species produced in plasma-water interaction is the hydroxyl radical due to its contribution as a strong oxidizing agent in water treatment and biomedical fields and as a precursor to the production of hydrogen peroxide. Some of the most promising works on OH diagnostics of the last decade have used diagnostics methods like optical emissions spectroscopy, broadband UV absorption, and laser-induced fluorescence (LIF) [4] to quantify OH in pulsed discharges containing trace water vapor in inert carrier gases. In a plasma discharge, the OH density produced is governed by several factors: the gas temperature (T_g), electron temperature (T_e), degree of ionization, electron number density (n_e), overall ion number density, the major positive and negative ionic species, vibrational temperature, and composition of carrier gases and other admixtures containing H_2O vapor [22].

LIF detection of OH in dc corona discharge in the air was studied with and without Ar gas flow [23]. It was noted that without added Ar, the discharge emission mostly adopted streamer-like structures; the emissions were almost entirely from N_2 2nd +ve, whereas the fluorescence from OH was very low. Contrary, when Ar flow was added, the discharge emission appeared filamentary. The emissions of both OH and N_2 2nd positive were detected and the OH LIF signals were stronger than that in the case without Ar. The difference in plasma morphology in the two cases is attributed to the difference in quenching interaction of OH• excited states between air and Ar* metastable.

6

The OH density had also been measured with laser-induced predissociation fluorescence (LIPF) for a pulsed positive corona discharge [24] and with LIF for a pulsed arc discharge [25] in an $H_2O+O_2+N_2$ mixture. In the case of a pulsed corona, there is a higher OH density at the anode resulting from a higher T_g, which favors the OH forming heavy-particle reactions. In the rest of the discharge volume, T_g was lesser owing to a comparative greater OH recombination reaction rates [24]. In the case of a pulsed arc system, it was further observed that the addition of O_2 decreased OH lifetime due to dissociative recombination among OH, O, and O_3 but also increased OH production rate due to new heavy particle interaction routes between O^* metastable and H_2O [25].

Dilecce et al. measured OH density using LIF in an atmospheric pressure He-H_2O DBD with LIF for different H_2O vapor partial pressures [26]. The LIF excitation de-excitation scheme employed the OH(A-X) transition: OH(X, v=0) + hv_L → OH(A, v''=0,1) → OH(X, v=0) + hv_F. The OH density was found using the LIF model as well as chemical modeling of the decay trace using rate coefficients of OH dissociative recombination to H_2O and three-body OH recombination to H_2O_2. The OH density was found to be in the order of 10^{19} m^{-3} and found to be strongly dependent on the H_2O concentration, whereas very loosely dependent on the discharge current.

Bruggeman et al. measured absolute OH density in atmospheric pressure He-H_2O rf glow discharge [27] using a 310 nm light-emitting diode and a high-resolution spectrometer. However, a maximum water concentration of only 1.1% could be studied since the discharge lost stability at higher concentrations. The desired concentration is produced in two steps: first, a stream of helium is passed through a bubbler containing water, and the outflow from the bubbler is considered to be saturated with water vapor at

room temperature; then, a metered flow of fresh helium is added to this saturated stream to obtain the desired concentration. The gas temperature (T_g) was measured from the rotational temperature (T_r) of the N_2(C-B)(0-0) state and the absolute OH concentration was determined this T_r; the Stark broadening of H-Balmer lines that could be used to measure n_e, using optical emission spectroscopy (OES) [28]. The electron number density (n_e) was found to be the order from 10^{19}-10^{20} m^{-3} and T_g was found to be between 345-410 K. Schroter et al. studied He-H_2O in an atmospheric pressure radio-frequency (rf) plasma jet with VUV Fourier Transform Absorption Spectroscopy and UB Broadband absorption spectroscopy and compared it with zero-dimensional chemical model [26]. Detailed kinetics were presented along the discharge path. Initially, OH was formed by electron impact dissociation of H_2O- which also produced H and H$^-$- as well as ion impact reaction of H_2O^+ with H_2O clusters; OH, is consumed by recombination to H_2O_2 and H_2O. In the mid discharge path, OH is formed by heavy particle reactions between H and HO_2 and consumed by dissociative recombination with H_2O_2 and HO_2. In the afterglow, OH is formed by heavy particle interaction between H + HO_2 and H+H_2O_2, however, decay reactions dominated through the same recombination reactions at earlier sections.

Du et al. studied morphology, T_g, OH, and H_2O_2 densities of atmospheric pressure dielectric barrier discharge carrying a maximum water vapor concentration of 2.5% in two different carrier gases: He and Ar via ICCD imaging, absorption spectroscopy, and colorimetric method [29]. With increasing water concentration, DBD with both gases showed more filamentary structures. T_g was observed to increase for higher power but remained independent of water loading. OH, density in He+H_2O DBD was found to be half of that with Ar+ H_2O, however, He+H_2O showed a square root dependence with H_2O

concentration, whereas Ar+H_2O DBD showed a bell-curve behavior; both discharges showed increased OH density with increased power. This is somewhat contrary to [26], which stated that OH formation is very weakly dependent on the discharge current. H_2O_2 concentration was in Ar+H_2O DBD was found to be ~ 4 times that in He+H_2O DBD. Variations of OH and H_2O_2 densities between the two gases were attributed to the respective kinetics but those had not been discussed in detail.

Some of the most prominent works on OH detection and quantification with LIF had been on atmospheric pressure He-H_2O discharges in pin-pin electrode arrangement from 2012 to 2014 [29-31]. A frequency-doubled dye laser at 282.6 nm was used to time and spatially resolved LIF from OH(A-X) state. The T_g was measured using a Boltzmann plot from exciting different rotational states of OH, [24]. This is verified by rotational temperature (T_r) obtained from spectrally resolved fluorescence from OH(A) state and fitting the spectra with Lifbase [32]. This was under a very common assumption that the rotational energy transfer rate is faster than the OH(A) de-excitation rate at atmospheric pressure conditions. The electron densities were obtained from the Van der Waals and Stark broadening of the H_β, H_α, and N emission lines at 746 nm. The OH density was measured from Rayleigh scattering and a multi-level LIF model and/or a chemical model to trace the OH decay in the afterglow. The heavy particle and charge transfer reactions factoring for OH production and recombination were discussed. In a comparative analysis, absolute OH density was quantified by four independent methods: 4-level LIF model, 6-Level LIF model, a chemical model, and UV absorption for He-H_2O discharge in pin-pin electrodes [33]. The OH densities obtained from each method were found to be within the experimental accuracy.

1.3 PROBLEM STATEMENT

Despite such attempts to explore plasma discharge in contact with liquids, the kinetics of the species involved in the discharge has remained vastly unknown. There is still considerable information to be explored regarding the charged species transfer in the gas-liquid interface in plasma. Experimental validation of kinetic and transport models of humid plasma are very limited as so are the ionic species exchange between the interfaces [4, 34]. According to a 2016 roadmap [4], there is a need for the study of several factors in plasma-liquid interactions: electron impact reactions with •OH and H_2O_2, refined ion kinetics, neutral kinetics, interfacial transport of charged species with electron impact reactions, and energy transport, extensive information on the effect of pH, temperature and electric field on liquid phase reactions and vibrational kinetics of H_2O and •OH excited states. Even though a considerable amount of work has been accomplished regarding gas phase diagnostics, the existence of unknown water vapor gradients means that LIF measurements require more detailed models regarding collisions of excited states [4]. Also, both LIF and OES have to image in multiple measurements instead of single-shot and for a non-reproducible plasma, this may create inconsistent results.

One of the most daunting obstacles with present diagnostics systems is that most are not selective to the plasma-induced liquid phase chemistry, which has very short time scales and is difficult to control [34]. Surface phenomenon studied in controlled environments may not be resemblant to all cases as there is currently a lack of understanding for standardization of these techniques [35]. Further challenges lie in reactor design for plasma-liquid applications in water treatment and plasma medicine, in which plasma-liquid interactions can be studied in a controlled environment [34]. Even though

destructive/oxidative capacities of plasmas have been studied for several contaminants, the coupling between plasma physics and chemistry associated with the processes is still yet to be extensively understood [35].

1.4 DISSERTATION OUTLINE

This dissertation attempts to address some of the research needs regarding the unknown kinetics in plasma interactions with the highest attainable concentration of water vapor. The scope of this dissertation is outlined below:

Chapter 1 introduces the general problem statement along with the outline of this dissertation work.

Chapter 2 contains the characterization study of dc discharge in low pressure water vapor with optical emission spectroscopy along the entire discharge path. It discusses the possible excitation transitions and excited metastable species present in a plasma discharge in pure water vapor. In addition, it also finds two of the fundamental properties of water vapor that had not been reported in the known literature.

Chapter 3 discusses an application for measuring the dryness of a nuclear cask by a non-intrusive method, which employs dc discharge in water vapor contained in a carrier gas.

Chapter 4 finds an observable anomaly in the stratification of positive column of dc discharge in air, which is contrary to the classical appearance of striations, which might likely be influenced by the presence of water vapor. This observable phenomenon might be either due to the quenching effect or due to vibrational kinetics of H_2O, however, since it is very challenging to model striations in a gaseous mixture of polyatomic molecules,

striations were first modeled in N_2 only. The role of vibrational excitation reactions in the forming of classical striations is discussed in detail.

Chapter 5 discusses an application for disinfection of soft surfaces using dielectric barrier discharge plasma with humid air as a discharge medium. A comparison between OES and pH characterization of the treatment media is used to imply what species might be produced in the discharge.

Chapter 6 discusses a modified DBD application of that used in the previous chapter to study OH and H_2O_2 produced in a DBD with He-H_2O mixture as discharge medium. The OH is measured through a laser-induced fluorescence method with 282.6 nm. The H_2O_2 is measured with photofragmentation laser-induced fluorescence with 213 nm and 282.6 nm beams. From the known literature, there had been no known previous application of photofragmentation LIF to diagnose hydrogen peroxide or any other chemical species in the plasma. Finally, the dissertation ends with Chapter 7 as a conclusion with how the work done on this dissertation can be continued in the future for research.

1.5 REFERENCES

1.   Fridman, A. and L.A. Kennedy, *Plasma physics and engineering*. 2004: CRC Press.

2.   Staack, D.A., *Characterization and stabilization of atmospheric pressure DC microplasmas and their application to thin film deposition.* 2009.

3.   Vanraes, P. and A. Bogaerts, *Plasma physics of liquids—A focused review.* Applied Physics Reviews, 2018. **5**(3): p. 031103.

4.   Bruggeman, P., M.J. Kushner, B.R. Locke, J.G. Gardeniers, W. Graham, D.B. Graves, R. Hofman-Caris, D. Maric, J.P. Reid, and E. Ceriani, *Plasma–liquid interactions: a review and roadmap.* Plasma sources science and technology, 2016. **25**(5): p. 053002.

5.   Zhou, L. and Y. Jiang, *Recent progress in dielectric nanocomposites.* Materials Science and Technology, 2020. **36**(1): p. 1-16.

6.   Bruggeman, P., D. Schram, M.Á. González, R. Rego, M.G. Kong, and C. Leys, *Characterization of a direct dc-excited discharge in water by optical emission spectroscopy.* Plasma Sources Science and Technology, 2009. **18**(2): p. 025017.

7.   Fortov, V., I. Iakubov, and A. Khrapak, *Physics of strongly coupled plasma*. Vol. 135. 2006: OUP Oxford.

8.   Boates, B. and S.A. Bonev, *Electronic and structural properties of dense liquid and amorphous nitrogen.* Physical Review B, 2011. **83**(17): p. 174114.

9.   Martinez-Vega, J., *Dielectric materials for electrical engineering*. 2013: John Wiley & Sons.

10.   Vanraes, P., A. Nikiforov, A. Bogaerts, and C. Leys, *Study of an AC dielectric barrier single micro-discharge filament over a water film.* Scientific reports, 2018. **8**(1): p. 1-11.

11.   Setsuhara, Y., *Low-temperature atmospheric-pressure plasma sources for plasma medicine.* Archives of biochemistry and biophysics, 2016. **605**: p. 3-10.

12.   Miralai, S., E. Monette, R. Bartnikas, G. Czeremuszkin, M. Latreche, and M. Wertheimer, *Electrical and optical diagnostics of dielectric barrier discharges (DBD) in He and N2 for polymer treatment.* Plasmas and Polymers, 2000. **5**(2): p. 63-77.

13.   Li, X., D. Niu, P. Jia, N. Zhao, and N. Yuan, *Investigation on the Micro-Discharge Characteristics of Dielectric Barrier Discharge in a Needle-Plate Geometry.* Plasma Science and Technology, 2011. **13**(2): p. 213.

14.   Cserfalvi, T. and P. Mezei, *Operating mechanism of the electrolyte cathode atmospheric glow discharge.* Fresenius' journal of analytical chemistry, 1996. **355**(7): p. 813-819.

15.   Gaisin, A.F. and E.E.e. Son, *Vapor-air discharges between electrolytic cathode and metal anode at atmospheric pressure.* High temperature, 2005. **43**(1): p. 1-7.

16.   Baba, K., T. Kaneko, and R. Hatakeyama, *Ion irradiation effects on ionic liquids interfaced with rf discharge plasmas.* Applied physics letters, 2007. **90**(20): p. 201501.

17.   Yamamoto, Y.-i., Y.-I. Suzuki, G. Tomasello, T. Horio, S. Karashima, R. Mitríc, and T. Suzuki, *Time-and angle-resolved photoemission spectroscopy of hydrated*

electrons near a liquid water surface. Physical review letters, 2014. **112**(18): p. 187603.

18.   Verhaart, H. and P. Van der Laan, *The influence of water vapor on avalanches in air.* Journal of applied physics, 1984. **55**(9): p. 3286-3292.

19.   Gallimberti, I., *The mechanism of the long spark formation.* Le Journal de Physique Colloques, 1979. **40**(C7): p. C7-193-C7-250.

20.   Liu, S., S. Oshita, S. Kawabata, Y. Makino, and T. Yoshimoto, *Identification of ROS produced by nanobubbles and their positive and negative effects on vegetable seed germination.* Langmuir, 2016. **32**(43): p. 11295-11302.

21.   Vanraes, P., A. Nikiforov, M. Lessiak, and C. Leys. *Time-resolved characterization of a pulsed discharge in a stationary bubble*. in *Journal of Physics: Conference Series*. 2012. IOP Publishing.

22.   Bruggeman, P. and D.C. Schram, *On OH production in water containing atmospheric pressure plasmas.* Plasma Sources Science and Technology, 2010. **19**(4).

23.   Kanazawa, S., H. Tanaka, A. Kajiwara, T. Ohkubo, Y. Nomoto, M. Kocik, J. Mizeraczyk, and J.-S. Chang, *LIF imaging of OH radicals in DC positive streamer coronas.* Thin Solid Films, 2007. **515**(9): p. 4266-4271.

24.   Ono, R. and T. Oda, *Measurement of gas temperature and OH density in the afterglow of pulsed positive corona discharge.* Journal of Physics D: Applied Physics, 2008. **41**(3): p. 035204.

25. Ono, R. and T. Oda, *OH radical measurement in a pulsed arc discharge plasma observed by a LIF method.* IEEE Transactions on Industry applications, 2001. **37**(3): p. 709-714.

26. Schröter, S., A. Wijaikhum, A.R. Gibson, A. West, H.L. Davies, N. Minesi, J. Dedrick, E. Wagenaars, N. De Oliveira, and L. Nahon, *Chemical kinetics in an atmospheric pressure helium plasma containing humidity.* Physical Chemistry Chemical Physics, 2018. **20**(37): p. 24263-24286.

27. Bruggeman, P., G. Cunge, N.J.P.S.S. Sadeghi, and Technology, *Absolute OH density measurements by broadband UV absorption in diffuse atmospheric-pressure He–H2O RF glow discharges.* 2012. **21**(3): p. 035019.

28. Laux, C.O., T. Spence, C. Kruger, and R. Zare, *Optical diagnostics of atmospheric pressure air plasmas.* Plasma Sources Science and Technology, 2003. **12**(2): p. 125.

29. Du, Y., G. Nayak, G. Oinuma, Z. Peng, and P.J. Bruggeman, *Effect of water vapor on plasma morphology, OH and H2O2 production in He and Ar atmospheric pressure dielectric barrier discharges.* Journal of Physics D: Applied Physics, 2017. **50**(14): p. 145201.

30. Verreycken, T., N. Sadeghi, and P.J. Bruggeman, *Time-resolved absolute OH density of a nanosecond pulsed discharge in atmospheric pressure He–H2O: absolute calibration, collisional quenching and the importance of charged species in OH production.* Plasma Sources Science and Technology, 2014. **23**(4): p. 045005.

31. Verreycken, T., R. Van der Horst, A. Baede, E. Van Veldhuizen, and P. Bruggeman, *Time and spatially resolved LIF of OH in a plasma filament in atmospheric pressure He–H2O.* Journal of Physics D: Applied Physics, 2012. **45**(4): p. 045205.

32. Luque, J., *LIFBASE, Database and spectral simulation for diatomic molecules.* SRI International Report, 1999. **99**.

33. Verreycken, T., R. Van Der Horst, N. Sadeghi, and P. Bruggeman, *Absolute calibration of OH density in a nanosecond pulsed plasma filament in atmospheric pressure He–H2O: comparison of independent calibration methods.* Journal of Physics D: Applied Physics, 2013. **46**(46): p. 464004.

34. Adamovich, I., S. Baalrud, A. Bogaerts, P. Bruggeman, M. Cappelli, V. Colombo, U. Czarnetzki, U. Ebert, J. Eden, and P. Favia, *The 2017 Plasma Roadmap: Low temperature plasma science and technology.* Journal of Physics D: Applied Physics, 2017. **50**(32): p. 323001.

35. Bruggeman, P. and C. Leys, *Non-thermal plasmas in and in contact with liquids.* Journal of Physics D: Applied Physics, 2009. **42**(5): p. 053001.

CHAPTER 2 :

DC DRIVEN LOW PRESSURE GLOW DISCHARGE IN HIGH WATER

VAPOR CONTENT:

A CHARACTERIZATION STUDY

2.1 INTRODUCTION

In recent years, plasma discharge in liquid medium has been a topic of immense interest [35]. Theoretical efforts have been pursued to obtain insight into physicochemical processes being influenced by trace water vapor either being present as residual or provided at a known concentration [36, 37]. However, studies on discharge at high vapor content are limited.

Wilson et al. [38] studied atmospheric glow discharge over a liquid electrode. They were able to visualize all the prominent structures of a glow discharge: the anode glow, the positive column, and the negative glow. It was found that the discharge was unstable when the liquid surface was used as the cathode and vice versa. This is attributed to the negative glow being on the liquid surface in such cases. Since the negative glow is at a higher temperature, it causes more evaporation which renders the discharge unstable. It was also suggested that the chemical mechanisms resulting in the formation of electronegative species are a possible cause for the rotation of the discharge structure on the liquid surface.

Bruggeman et al. [6] studied plasma discharge in liquid for different conductivities with the powered electrode shrouded with insulation except for the tip. It was observed that for liquid of low conductivity, streamers are directly initiated in the liquid. The optical emission spectroscopy (OES) of these streamers shows the OH(A-X), H-Balmer, and O lines on the spectrum. For moderate conductivity, heat transfer is facilitated to form a bubble at the tip of the powered electrode and the streamers are initiated inside the bubble. In addition to the spectral lines viewed for liquid streamers, streamers in bubbles also emit spectral lines for nitrogen, namely, N_2(C-B) N_2^+ and N_2(B-A). For even higher conductivity, bubbles are initiated at the tip of the powered electrode, but the streamers

mostly formed in the liquid-bubble interface rather than in the bubble itself. The OES is similar to that observed for liquid streamers. The electron number density is calculated from the broadening of the H_β spectral line. The rotational temperature measurement from OH(A-X) lines was discouraged owing to the low accuracy and the N_2(C-B)(0-2) band at 360–381 nm was recommended instead. Verreycken et al. [39] studied the OES of a pin-liquid dc glow discharge for different filling gases. It was stated that the most dominant OH(A) producing reactions are the electron impact dissociation of H_2O^+ and the electron impact dissociation of H_2O to OH(X) and then subsequent electron impact excitation of OH(X) to OH(A). Several heavy particle reactions involving metastable of the filler gas molecules with H_2O producing OH(A) are provided. He metastables are deemed to be highly energetic and these directly ionize H_2O on impact contrary to form OH. Electron temperature (T_e) is calculated from balancing recombination losses of electrons to ionization reactions, ignoring diffusion losses. In the positive column, the n_e and T_e are stated to be of the order of 10^{19} m^{-3} and 1 eV respectively. Xiong et al. [40] spatially resolved absolute OH densities for a similar apparatus via broadband absorption spectroscopy. It was assumed that both n_{OH} and T_g have symmetric 2D Gaussian distribution in the discharge. For both the water cathode and the water anode, the OH had the highest density at the cathode. For the water cathode, the OH density progressively decreased from the cathode to the anode as moved further away from the water. However, even for the water anode, the highest OH density is observed at the cathode as the highest energetic electrons are found in this region compared to the rest of the discharge regime. Verreycken et al. [31] spatially resolved OH density in a pulsing discharge in helium with an admixture of 0.9% H_2O in a pulsing discharge. A high voltage pulser at a frequency of

1kHz and pulse duration of 170 ns was used. A Frequency-doubled dye laser (Sirah CBR-LG-24-HRR), with Rhodamine 6G as the dye, pumped by an Nd:YAG laser at 532 nm was used. The laser had a pulse frequency of 1 kHz and an FWHM of 6ns. P1(2) transition of the OH[(X, $v"= 0$) $\rightarrow$(A, $v' = 1$)] at 282.6nm is used to study LIF. A bandpass filter of 313 nm $\pm$ FWHM 10 nm was used to filter other signals coming from the plasma. Instead of calibration, known reaction rate coefficients were used to measure absolute OH density from LIF signals. An OH spike in the afterglow is observed even at lower T_g and is attributed to recombination reactions since in the afterglow T_g is not enough to sustain electronic excitation.

In this study, discharge characteristics of plasma in high water concentration (> 90%) are investigated experimentally for a pressure range of 1 – 15 Torr to maximize vapor loading without condensation. Voltage-current characteristics were obtained over 0-14 mA of current for each operating pressure; current density was determined to ensure a "normal" glow regime of operation. Spatially resolved optical emission spectroscopy was also conducted to determine OH and H distribution in the interelectrode separation. The normalized intensities of OH emission lines are found to be more prominent in the positive column and anode, whereas the emission lines of H are most intense in the cathode glow region. The electric field distribution along the discharge gap was also measured. We envision that the data obtained from this characterization study will also provide valuable data for the validation of plasma kinetic schemes associated with water vapor.

2.2 EXPERIMENTAL SETUP
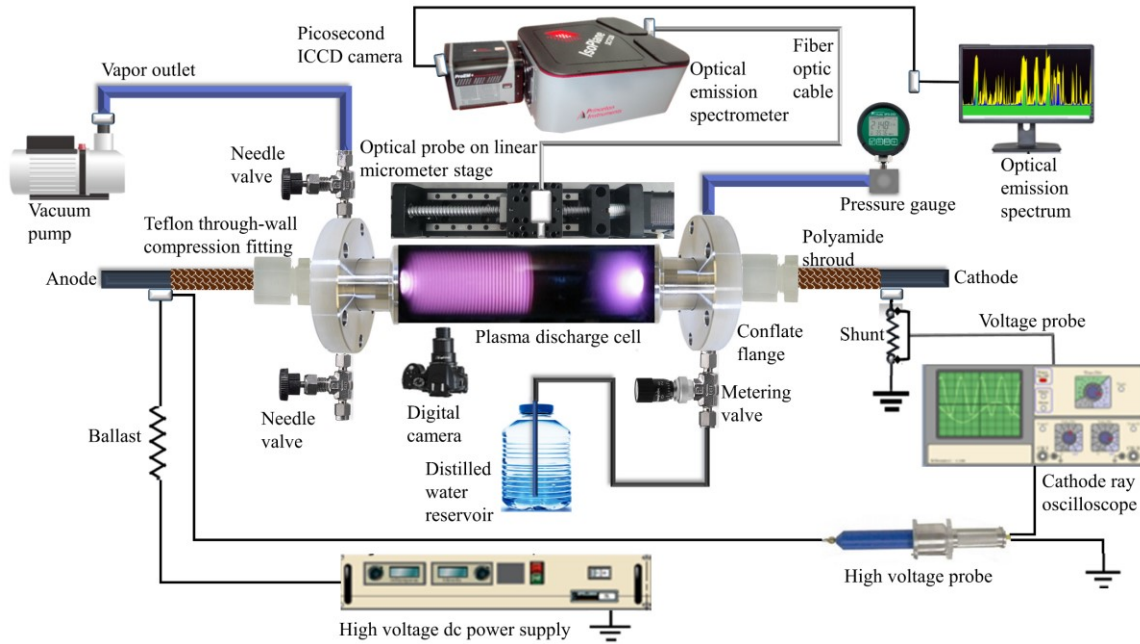
Figure 2.1 Experimental setup for low pressure water vapor characterization study

Figure 2.2 Plasma discharge structure showing negative glow and weak positive column

The experimental setup for water vapor characterization is shown in Figure 2.1. A dc power supply (Glassman 0-20kV, 300W) is connected in series to a ballast resistor (100 kΩ), the low-pressure plasma cell, and a shunt resistor (10 kΩ) to measure the discharge current. A high voltage probe (North star PVM-4) and an oscilloscope probe (Tektronix M12) are used to measure the voltage drops across the discharge and the shunt respectively; both the probes are connected to a mixed-signal oscilloscope (Keysight MSO7054B). The

discharge is enclosed in a cylindrical plasma cell consisting of a 16.0 cm (maximum operable length of 20 cm) long and 3.71 cm outer diameter cylindrical tube of borosilicate glass with two stainless steel disc electrodes on the opposite ends.

The electrodes have a diameter of 0.95 cm. The electrode arrangements are such that before conducting the experiments, the inter-electrode distance can be varied. The discharge cell is connected to the vacuuming system through ultra-torr conflate flanges. Additional fittings include a pressure gauge, a valve connecting the vacuum pump, and an inlet valve for supplying freshwater vapor from a liquid reservoir. The pressure is measured with a Teledyne Hastings 760s gauge. The vacuum is attained and maintained with an Agilent IDP-15 dry scroll vacuum pump. The outer periphery of each stainless-steel electrode is wrapped with polyamide tape (Kapton) on the sides to prevent the discharge from diffusing in between the glass tube and electrode gap at low pressures. A Nikon D7000 digital camera is used to image the discharge over a range of discharge current conditions. Each image was captured over an exposure time of 3 seconds with a NIKKOR 18-55mm f/3.5-5.6G lens with focal length, aperture, and ISO set to 32mm, f/4.5, and ISO-200 respectively.

The optical emission spectrum is taken with Princeton Instruments Isoplane SCT-320 spectrometer with 4 Picos ICCD camera, connected to an optical cable. A weak positive column and an anode glow are observed at larger gaps, whereas, at shorter distances only a constricted negative glow is present. The optical emission spectrometer constantly monitors N_2 (second positive, $C^3\Pi$- $B^3\Pi$) peaks in the spectrum to check for the presence of air; the leakage of air is mitigated by periodically flushing the system with water vapor.

2.3 VOLTAGE-CURRENT (V-I) CHARACTERISTICS

The V-I characteristics of the system are studied for 5 different pressures for an inter-electrode spacing of 20 cm as shown in Figure 2.3. V-I characteristics for nine inter-electrode spacings for each at two different pressures are shown in Figure 2.4. The behavior is typical of that of glow discharge in the sense that the discharge voltage (V_d) has a weak dependence on the discharge current (I_d). In both figures, discharge voltage increases with an increase in either pressure (p) or inter-electrode spacing (d) or both. This is because, with an increase of either of these parameters, the breakdown voltage increases as depicted by p*d going further to the right of the Paschen curve.
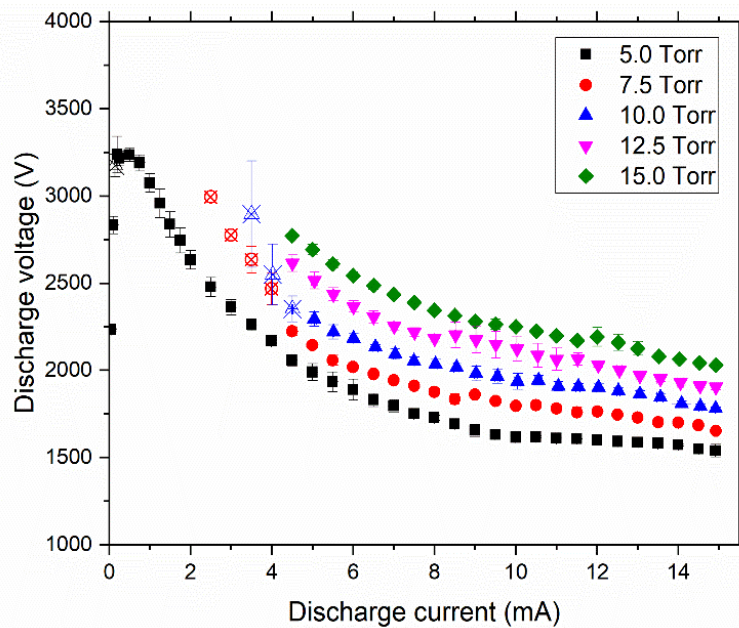
Figure 2.3 V-I characteristics of water vapor at electrode spacing of 20 cm
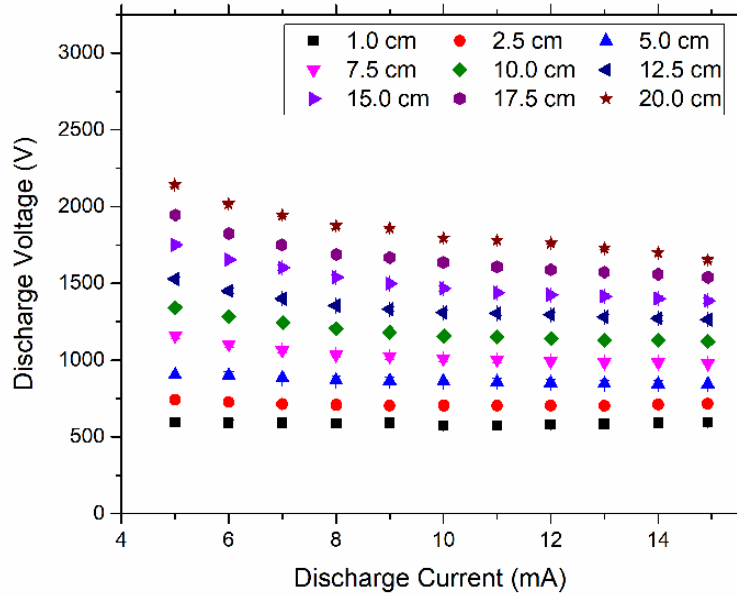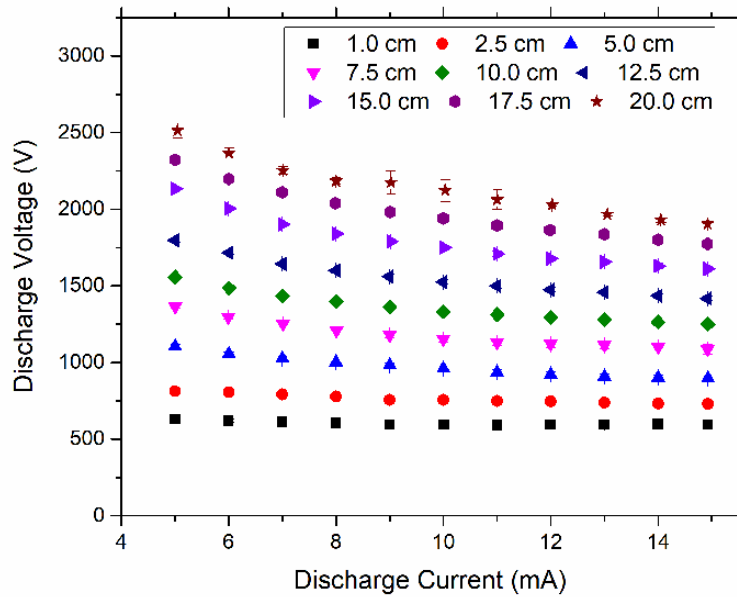
Figure 2.4 (a) V-I characteristics of water vapor for various electrode spacings at 7.5 Torr, **(b)** V-I characteristics of water vapor at various electrode spacings at 12.5 Torr

2.4 PRESSURE-NORMALIZED CURRENT DENSITY

It is observed that for pressures of 12.5, 15, 17.5, and 20 Torr(s), the cathode glow does not cover the entire electrode surface area and with increasing discharge current, an

25

increase in the area of the cathode spot is evident (Figure 2.5a). Calculation of current density (J) shows that the current density remains constant throughout the operation (not shown here). Calculation of pressure-normalized current density shows that it remains fairly constant irrespective of discharge current and operating pressure, Figure 2.5b. Such value for water vapor was not present in the literature. Thus, the pressure-normalized current density for water with stainless steel electrodes was found to be **0.0954 mA/(cm². Torr²)**.

(a)   (b)
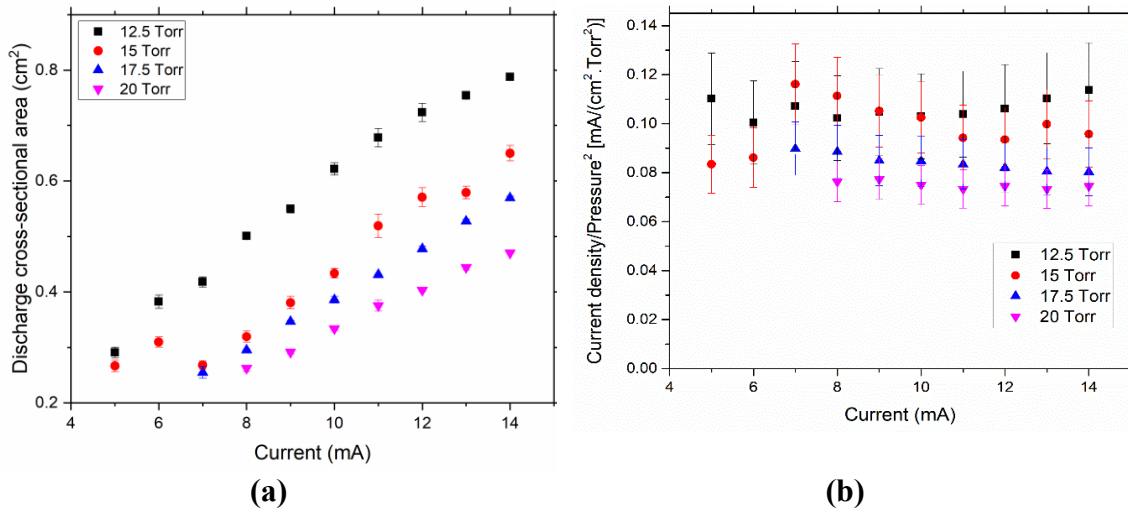
Figure 2.5 Measurements of pressure normalized current density for H_2O over SS electrodes: **(a)** Variation of cathode discharge area with discharge current and pressure, **(b)** Variation of pressure-normalized current density with discharge current and pressure

2.5 ELECTRIC FIELD AND NORMAL CATHODE POTENTIAL DROP

The electric field ($\vec{E}$) is calculated by measuring the gradient of discharge voltage (V_d) over several electrode spacings (d) at varying pressure conditions. It is seen that for the same I_d, $\vec{E}$ has a very weak dependence on d, Figure 2.6a. This may be explained by the fact that a lower d, p*d gets less and move towards the left of the Paschen curve lowering

26

V_d. Thus, since both V_d and d are decreasing, $\vec{E}$ stays unchanged. However, $\vec{E}$ is shown to

increase with increasing current and pressure, Figure 2.6b. In both cases, V_d has to increase

to provide a larger current and to compensate for higher collisions, respectively.
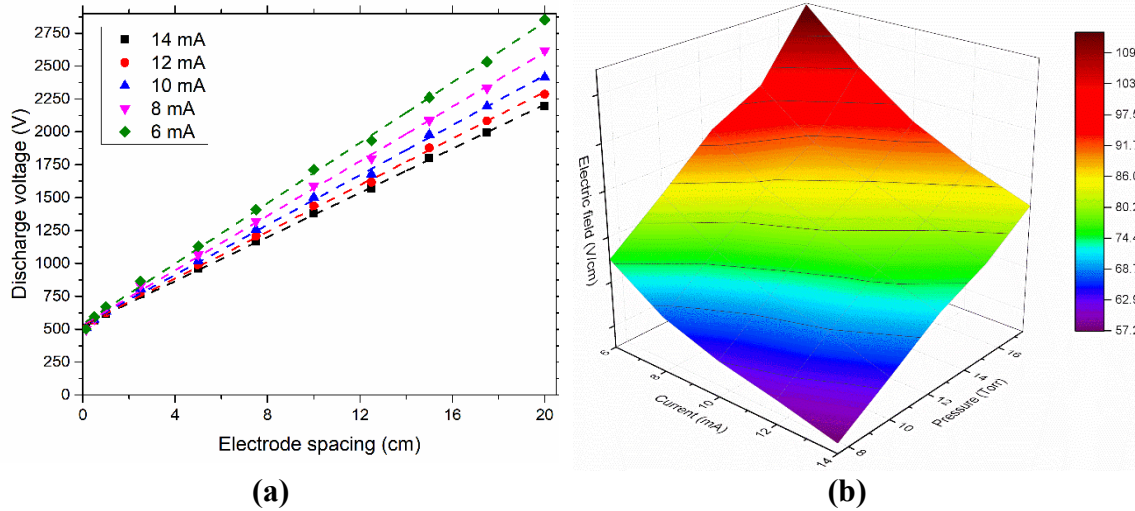
Figure 2.6 (a) Variation of V_d vs d for several I_d at 17.5 Torr, **(b)** Variation of $\vec{E}$ with
I_d and pressure

Nominal cathode potential drop (V_n) is a fundamental property of a specific gas in

glow discharge over a specific electrode material. In our experiment, V_n for H_2O over SS

electrodes is measured at the lowest inter-electrode spacing physically adjustable. In our

case, it was 0.15 cm from the cathode. It is measured to be 535 V for water vapor over

stainless steel electrodes. This is corroborated by Figure 2.7.

27
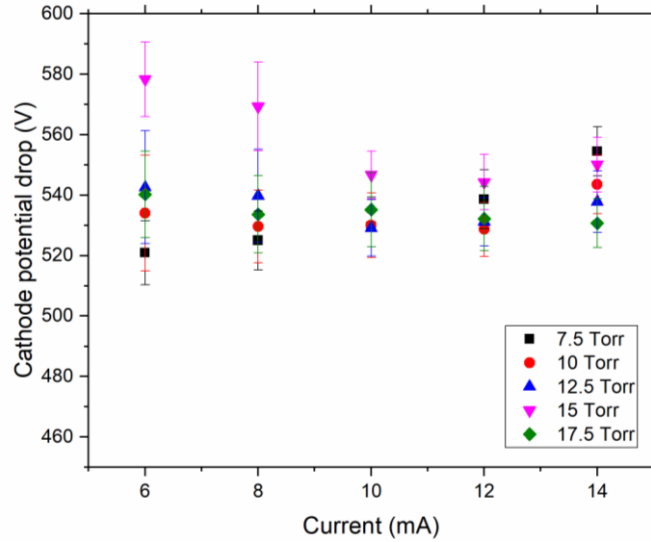
Figure 2.7 Variation of V_n over I_d and operating pressure

2.6 SPATIAL DISTRIBUTION OF H_α AND OH

Figure 2.8 shows the variation in optical emission spectra of the OH (A-X) band and the H_α spectral lines. It is observed that the OH(A-X) emission is the strongest at the anode whereas the H_α emission is the strongest at the cathode. This might be due to the fact that OH is electronegative and thus would be electrostatically attracted to the anode and vice versa. However, another pertinent fact to be noticed is that in the positive column, emission from H_α is virtually undetectable, whereas there is still noticeable detection of OH (A-X). This might be due to OH having low -temperature kinetics that sustains it at the positive column. This can be verified from electron impact cross-sections with H_2O, which show that the excitation potentials of OH(X) and OH(A) states are ~10 eV whereas that of H_α is ~20 eV [41]. All of these cross-sections follow a similar pattern to that of a bell curve. It is seen that the maxima of cross-sections of OH(A) is at an electron energy of ~15 eV, after which it starts to descend whereas that of H_α is ~100 eV. Since in a dc discharge, T_e is the highest at the cathode sheath, this may also corroborate why the emission intensity

of H_α is the highest in this region. Since at the positive column and at the anode sheath, T_e is comparatively lower than that at the cathode sheath, emissions from OH(A-X) are the highest in these regions since both OH(A) and OH(X) transitions have the larger cross-sections at comparatively lower electron energy.
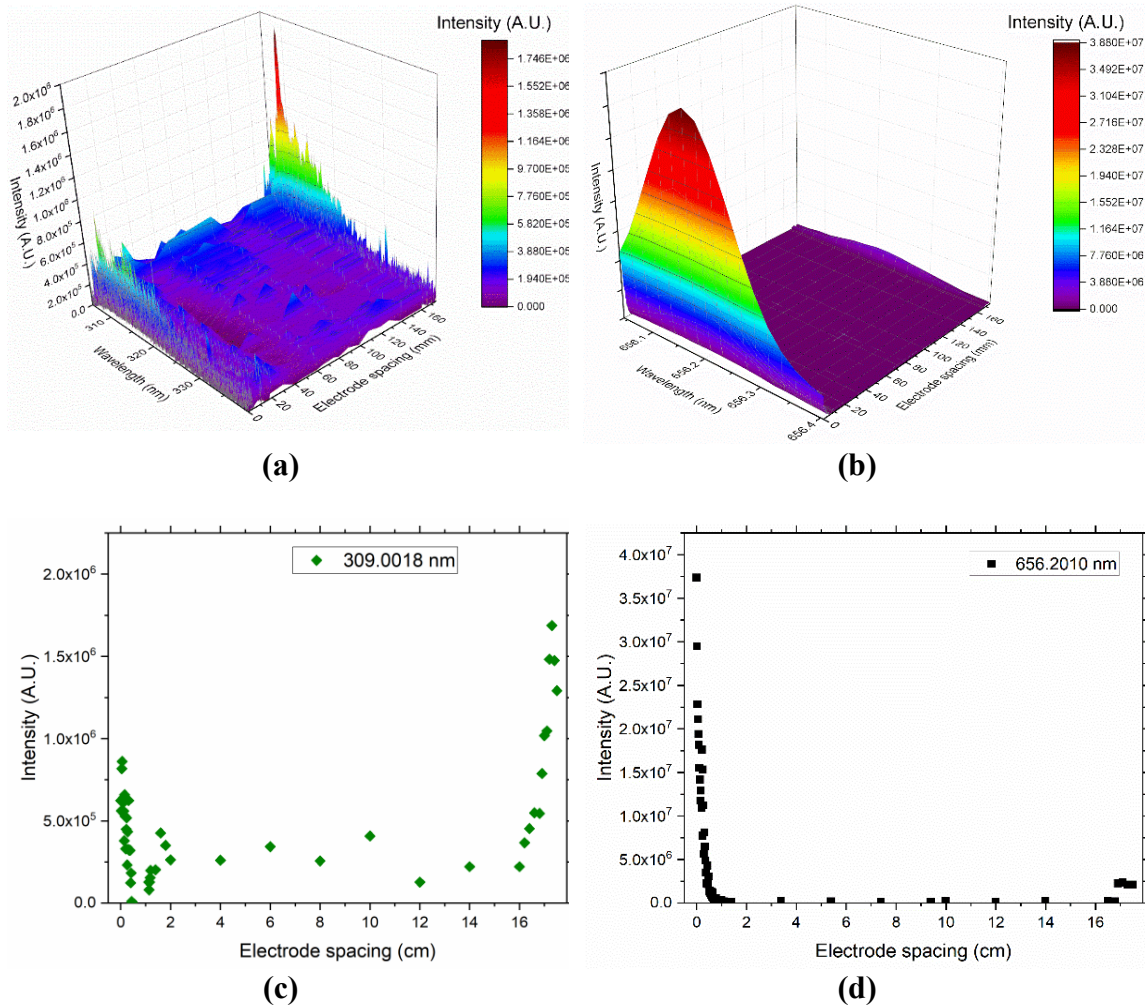
Figure 2.8 Spatial distribution of **(a)** OH(A-X) band, **(b)** H_α peak, **(c)** OH point peak at 309 nm, **(d)** H_α point peak at 656.20 nm across the inter-electrode spacing from the anode (left) to the cathode (right)

2.7 CONCLUSION

In the case of characterizing and spatially resolving the optical emissions spectrum in high water loading, V-I characteristics for 9 different electrode spacing(s), each for 5 different pressures(s) were recorded. Discharge area was measured; pressure normalized current density (J_n/p^2) was recorded and shown to be constant. J_n/p^2 of water vapor for stainless steel electrodes was found to be 0.0954 mA/(cm^2. Torr^2), which was previously unreported in the known literature. The electric field was calculated for several electrode spacings, and the normal cathode spot (V_n) was calculated for each reading and shown to be constant. V_n of water vapor for stainless steel electrodes was measured to be 535 V. A spatial distribution of normalized intensities of two major transitions from electron-impact H_2O dissociation was accomplished.

Future work will deal with calculating the gas temperature from optical emission spectroscopy and finding the distribution of electron number density across the discharge path from Stark broadening with an appropriate model that can handle the low electron number density as in low pressure conditions. This poses a somewhat challenge since the electron number density at low pressure is too less to be accurately resolved by the broadening of H-Balmer lines.

2.8 REFERENCES

6. Bruggeman, P., D. Schram, M.Á. González, R. Rego, M.G. Kong, and C. Leys, *Characterization of a direct dc-excited discharge in water by optical emission spectroscopy.* Plasma Sources Science and Technology, 2009. **18**(2): p. 025017.

31. Verreycken, T., R. Van der Horst, A. Baede, E. Van Veldhuizen, and P. Bruggeman, *Time and spatially resolved LIF of OH in a plasma filament in atmospheric pressure He–H2O.* Journal of Physics D: Applied Physics, 2012. **45**(4): p. 045205.

35. Bruggeman, P. and C. Leys, *Non-thermal plasmas in and in contact with liquids.* Journal of Physics D: Applied Physics, 2009. **42**(5): p. 053001.

36. Liu, D.-X., P. Bruggeman, F. Iza, M.-Z. Rong, and M.G. Kong, *Global model of low-temperature atmospheric-pressure He+ H2O plasmas.* Plasma Sources Science and Technology, 2010. **19**(2): p. 025018.

37. Sakiyama, Y., D.B. Graves, H.-W. Chang, T. Shimizu, and G.E. Morfill, *Plasma chemistry model of surface microdischarge in humid air and dynamics of reactive neutral species.* Journal of Physics D: Applied Physics, 2012. **45**(42): p. 425201.

38. Wilson, A., D. Staack, T. Farouk, A. Gutsol, A. Fridman, and B. Farouk, *Self-rotating dc atmospheric-pressure discharge over a water-surface electrode: regimes of operation.* Plasma Sources Science and Technology, 2008. **17**(4): p. 045001.

39. Verreycken, T., D. Schram, C. Leys, and P. Bruggeman, *Spectroscopic study of an atmospheric pressure dc glow discharge with a water electrode in atomic and molecular gases.* Plasma Sources Science and Technology, 2010. **19**(4): p. 045004.

40. Xiong, Q., Z. Yang, and P.J. Bruggeman, *Absolute OH density measurements in an atmospheric pressure dc glow discharge in air with water electrode by broadband UV absorption spectroscopy.* Journal of Physics D: Applied Physics, 2015. **48**(42): p. 424008.

41. Itikawa, Y. and N. Mason, *Cross sections for electron collisions with water molecules.* Journal of Physical and Chemical reference data, 2005. **34**(1): p. 1-22.

CHAPTER 3 :

PLASMA OPTICAL EMISSION SPECTROSCOPY FOR WATER

VAPOR QUANTIFICATION AND DETECTION [1]

3.1 INTRODUCTION

Spent fuel rods from nuclear reactors are kept in spent fuel pools to lower the temperature and radioactivity of the rods. The rods are then transferred to dry cask storage where these are shrouded in inert gas and radiation-shielded [42]. Despite being a standard industry practice, monitoring moisture content inside dry casks is still hindered by several limitations [43] and therefore remains a topic of research interest.

Many low-temperature processes have been investigated earlier with non-thermal non-equilibrium plasma systems, more specifically by the application of helium and air plasma jet(s) [44-52]. Yonemori et al. [49] attempted to measure OH density in the air-helium mixture in an atmospheric pressure plasma helium jet using the laser-induced fluorescence (LIF) technique for quantifying OH radicals. Two methods of OH generation were considered: OH, from the water vapor in the ambient air due to relative humidity, and OH generation from the water vapor present as an impurity in the helium gas. The OH radicals produced from ambient water vapor were not observed by LIF. It was proposed that this was due to the boundary region between a plasma jet and ambient air containing numerous active species, namely O, which rapidly react with the OH radical. Thus, this region acted as a fast sink of the OH radicals being produced. Production of OH in a nanosecond pulsed filamentary discharge in a He–H_2O mixture had also been studied by LIF [53]. It was reported that in the low electron-density ($\sim 10^{21}$ m^{-3}) mode of discharge, the maximum OH density was at the center of the discharge filament, while in high electron density mode ($\sim 10^{22}$ m^{-3}), the largest OH density was observed on the periphery of the discharge and the core was highly dissociated into atomic ions and OH^{+}. Low-pressure helium/water (He/H_2O) vapor discharge had been studied for a mercury-free source of

ultraviolet (UV) emission [50]. Even though it was found that the He-H_2O mixture performed better than pure water for generating UV emissions, the optimum conditions for maximum vacuum ultra-violet (VUV), ultraviolet (UV) and visible radiations were yet to be researched. Furthermore, the dependence of emission intensity as a function of water loading was not investigated. A detailed global model of low-temperature atmospheric-pressure He+H_2O plasmas was been presented in [54]. The ionization mechanisms stated, however, were the ones, chiefly predominant below 3000 ppm of water in the He+H_2O mixture. It was conjectured that at higher concentrations of water, 'electron detachment' could be the decisive factor but it was not elaborated upon in the model.

In pharmaceuticals research, the freeze-drying process was monitored with a cold plasma ionization device [55]. The plasma device consisted of a probe and relied on ionization and excitation of nitrogen and water molecules and collecting the associated spectrometric signals. However, no calibration for moisture content with signal intensity was given. Also, the procedure was localized and offered more of a qualitative determination of the critical stages in a freeze-drying cycle – providing information on water presence only. Nanosecond repetitively pulsed (NRP) discharges at atmospheric pressure had been studied previously in pure water vapor [56]. The dissociation products were analyzed via optical emission spectroscopy and hydrogen production was measured as a function of the discharge input power. The strength of the intensity of the H_α line in the optical emission spectrum was also emphasized. The temporal evolution of temperature and OH density produced was also studied in NRP discharges in pure water vapor [57]. Determination of water traces in gaseous samples via gas chromatography (GC) had been studied with helium ionization detection [51]. However, the pressure dependence and the

variation of signal strength at higher concentrations of water were yet to be investigated. Hanamura et al. [52] employed a microwave plasma for determining trace water present in a solid sample via emission spectroscopy. The study showed that for water analysis, hydrogen emission appears to be the most prominent emission line. Oxygen emission was useful in cases when sufficient C- containing species do not simultaneously participate in reacting with O-containing species. This method, however, suffered from the drawbacks that it was not as accurate as more conventional approaches, namely, electrochemical methods, nuclear magnetic resonance spectroscopy, mass spectrometry, and gas chromatography. Additionally, the calibration needed to be updated/cross-checked on a daily basis.

Thus, there do exist methods in the literature that showed that plasma discharge could be used to detect trace amounts of water on a multitude of occasions. In this paper, we propose a direct current (DC) driven plasma discharge in conjunction with optical emission spectroscopy to not only detect but also give a temporal quantification of water vapor in a binary mixture of helium and water vapor. The proposed system is envisioned to overcome some of the limitations posed by the previous methods [43].

3.2 DESCRIPTION OF THE EXPERIMENTAL APPARATUS

Figure 3.1 depicts the schematic of the experimental setup for a plasma discharge cell together with the ancillaries for the water detection purpose. The plasma chamber consists of two solid cylindrical copper electrodes, each with a diameter of 9.53 mm, typically maintained at a fixed separation distance of 4 mm. The pressure inside the plasma chamber is varied by a vacuum pump. For calibration of water vapor, the carrier gas mixed with water vapor was injected into the vacuum chamber as a result of the negative pressure

differential created by the vacuum to eliminate the possibility of gas accumulation in the piping network. Two calibrated mass flow controllers (MFCs) from MKS Instruments, were employed for varying the gas mixture composition for the calibration of the emission spectrum. The respective operating ranges of the MFCs for helium gas are 0-200 standard cubic centimeters per minute (sccm) and 0-500 sccm. For both the MFCs, the control range is from 2 to 100% of full scale (F.S.) with an accuracy of $\pm$ 1% of F.S. and repeatability of $\pm$ 0.2 % of F.S.
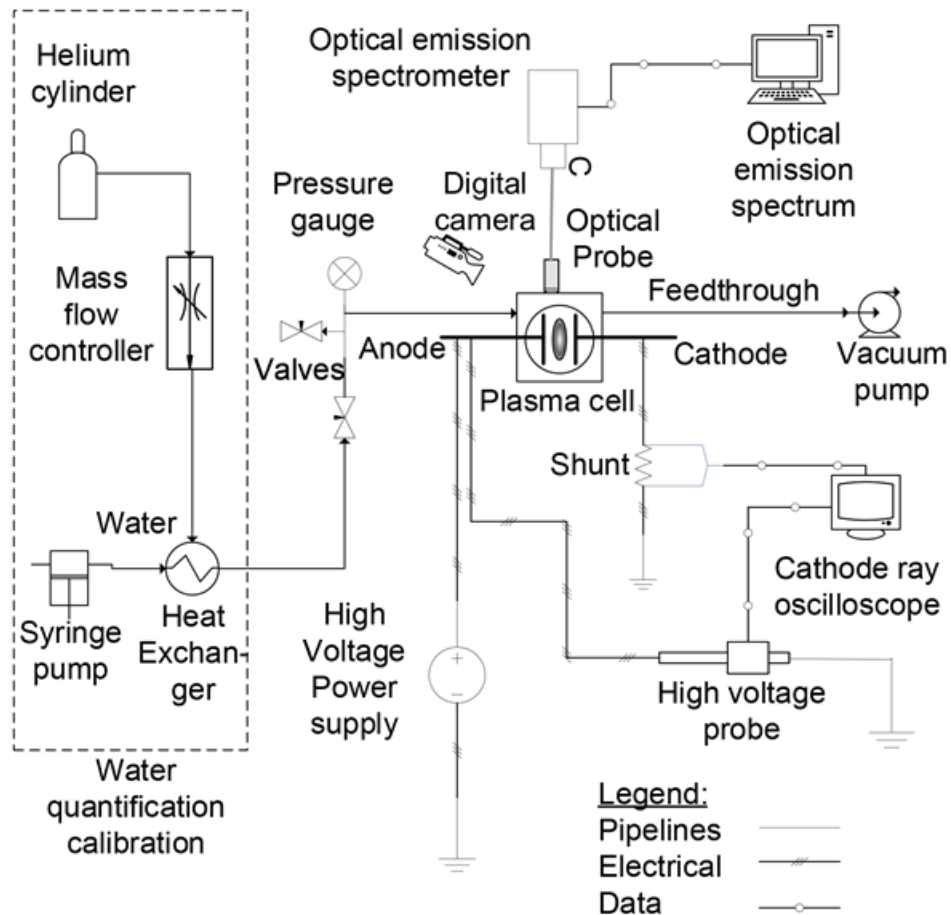
Figure 3.1 Schematic representation of the proposed setup for water detection

The electrode spacing is varied utilizing bellows. A variable inter-electrode spacing provides the capability of striking the plasma over a wide range of pressures, measured with a digital pressure gauge (Teledyne Hastings 760s), with a single power supply unit. The voltage across the plasma discharge and the shunt is measured with a cathode ray oscilloscope (Agilent Technologies InfiniiVision MSO7054B) and a high voltage probe (North Star high voltage PVM-4). The emission from the plasma discharge is acquired by an optical emission spectrometer (Ocean Optics HR 4000CG-UV-NIR) via an optical fiber (QP450-2-XSR) and the emission spectrum is observed and recorded using spectroscopy software ('Oceanview' from Ocean Optics). A complete list of instruments has been listed in Appendix B.

The pressure inside the plasma chamber is varied using a two-stage mechanical vacuum pump and is measured with a digital pressure gauge. For calibration, the carrier gas helium (Praxair UHP 5.0) is mixed with water vapor and then injected into the vacuum chamber as a result of the negative pressure differential created by the vacuum to eliminate the possibility of gas/water vapor accumulation in the piping network. For formulating mixtures having a higher concentration of water, typically the flow of helium is kept low, resulting in requiring a subsequently small amount of water to be pumped through the syringe (Hamilton 10 ml) via a syringe pump (KD Scientific KDS 200). This ensures the complete vaporization of water using the in-house vaporizer. For smaller concentrations of water, a higher flow rate of helium is maintained. The liquid water amount is regulated by the programmable syringe pump, which injects water directly into the co-current heat exchanger where it undergoes flash vaporization and simultaneously mixes with the helium gas, producing a gaseous helium-water mixture of known composition(s). Two calibrated

mass flow controllers (MFCs), one from MKS Instruments (0-500 sccm) and the other from Coastal Instruments (0-200 sccm), were employed independently for varying the mass flow rate of helium. The two mass flow controllers were utilized to cover both the low and high flow rate (or concentration) regimes. The plasma discharge is initiated and maintained via a Spellman (SL60P300) power supply unit. A high voltage probe (North Star PVM-4) was used to measure the discharge voltage (V_d) across the plasma. The discharge current (I_d) was read off by measuring the voltage across a 10kΩ shunt, close to the ground. Both V_d and I_d were acquired with a cathode ray oscilloscope.

For detecting water vapor concentration, the emission from H_α at 656.2 nm was employed. The H_α emission is the red visible spectral line generated by a hydrogen atom when an electron falls from the third lowest to second lowest energy level; this is the first transition in the Balmer series. The H_α is formed by the dissociation of water vapor to OH and H which undergoes further electronic excitation via electron impact reactions. The emission from H_α was chosen for detection purposes because of its very high sensitivity. Our experiments showed that even at a concentration of 2 ppm of water vapor, an emission from H_α was observed. It was found that the emission intensity of H_α was directly related to the water concentration level and thus was acquired for a range of water vapor concentration(s) in the calibration experiments, in which, the water vapor concentration was systematically increased in the gas mixture by injecting a higher amount of water vapor into the helium stream a had been explained earlier.

3.3 RESULTS AND DISCUSSION

3.3.1 CURRENT DENSITY MEASUREMENTS

The first set of experiments was conducted at 16.5 Torr and 2.0 mA since, at these conditions, a well-defined structure of plasma is observed, which includes a distinct positive column and a negative glow (Figure 3.2). With increasing water content, the discharge was observed to radially constrict and at the same time, show reduced emission intensity. Since water vapor has lower diffusivity than helium, the discharge undergoes radial constriction. The radial constriction also increases the current density resulting from a constant discharge current but a far more reduced cathode spot of the negative glow (i.e., the cross-sectional area of the negative glow). Furthermore, a higher water concentration also results in a diminished positive column.

| 0.0% H_2O | 1.8 % H_2O | 11.1 % H_2O | 16.1 % H_2O | 25.2 % H_2O |
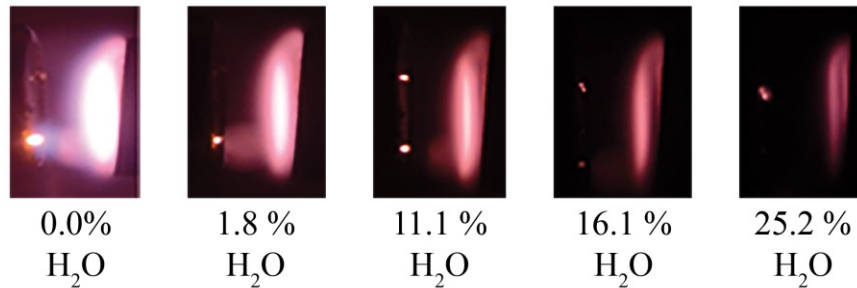
Figure 3.2 Structure of plasma discharge at different water concentrations in the gas mixture at operating pressure of 16.5 Torr and discharge current of 2.0 mA

It was observed that for a constant discharge current in the system, the discharge constricted almost by a factor of 3.75 for the entire range of moisture loading. Figure 3.3(a) shows that the current density follows a fairly strong linear correlation as a function of the molar fraction of water. Since the current density of a species is constant for a given

composition of the electrode and at a given pressure, this property also has the potential to be used for the quantification of water.

(a)

(b)
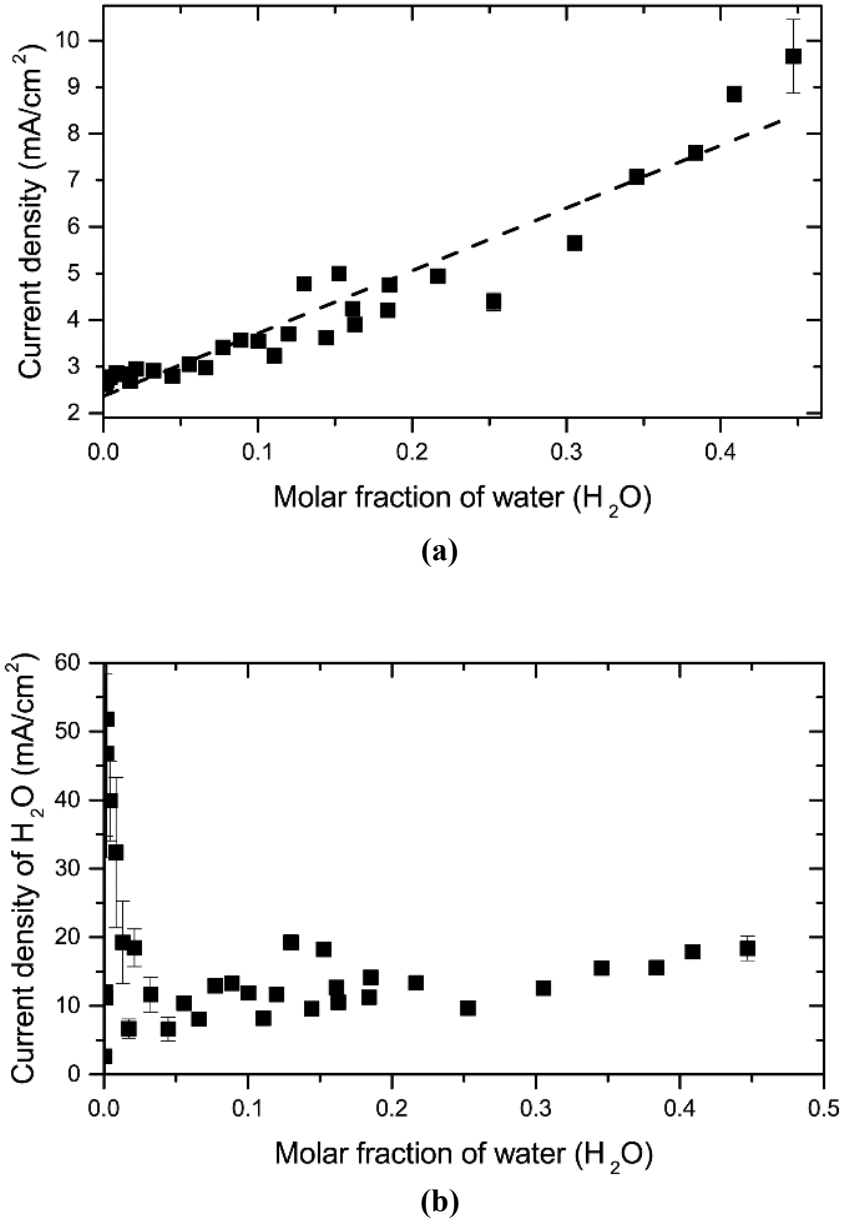
Figure 3.3 (a) Variation of the current density of the mixture with increasing water content, **(b)** Variation of the current density of H_2O with increasing water content

For validation of the calculated total current density of the system over the operational range, the current density of water is calculated from the equation: $J_{total} = (J_{He}).(X_{He}) + (J_{H_2O}).(X_{H_2O})$, assuming that the total current density is the algebraic sum of the molar fraction of the current densities of each component. Figure 3.3(b) shows that the current density of the water remains virtually independent of the molar fraction of water in the system, thus, validating the experimentation.

3.3.2 CALIBRATION PLOTS

Since helium gas contained 2 ppm of moisture as an impurity, the emission from the pure helium plasma discharge showed a peak at 656.2 nm in the optical emission spectrum resulting from H_α even when no water vapor is added to the stream. The H_α emission is the red visible spectral line created by a hydrogen atom when an electron falls from the third lowest to second lowest energy level; this is the first transition in the Balmer series. The emission from H_α at different water loading was recorded and the ratio of H to He emission intensity is chosen as a calibration marker. The variation in the calibration marker at different water loading(s) was recorded.

Figure 3.4 shows that the calibration marker follows a very strong linear correlation as a function of water and helium flow rate. For sensitivity purposes, the emission of helium excited states at different wavelengths was also looked into – the ratio of H_α at 656 nm with respect to the other dominant peaks of He(3^3D) at 587.6, He(3^1D) 667.8 and He(3^3S) 706.5 nm. At lower concentrations, the 667.8 nm and 587.6 nm behave almost identically since both these wavelengths pertain to similar electron transitional energies (1s.2p-1s.3d). The wavelength at 706.5 nm pertains to a higher electron transition (1s.2p-1s.3s) than the other two [2]. Therefore, as the helium concentration is reduced in the gas mixture, the intensity

at 706.5 nm decreases significantly faster. The correlation starts to deviate from its strong linear behavior with a subsequent increase in the error bars as the water to helium flow ratio is increased beyond 0.5. The non-linearity and increase in the uncertainty are attributed to the fact that since the partial pressure of water at atmospheric temperature is approximately 15 Torr, condensation of water inside the OES chamber occurs at higher concentrations, which induces nonlinearity in the system. It should be noted that a slight nonlinearity in the emission is observed for the low water mole fraction range (i.e., 0 – 0.025). Presumably, this is related to the heavy particle reactions between helium and water (e.g., Penning ionization, charge transfer, etc.). A definitive understanding of this behavior is still being pursued at this stage. Exemplar false-colored images of the plasma discharge are also presented in Figure 3.4 as insets. It is apparent that with an increase in the water vapor content, the discharge radially constricts and its emission intensity decreases owing to both the transport and electronegative behavior of water. The introduction of water in plasma reduces the electron density via attachment reactions. The attachment reactions also act as an energy sink and reduce the electron temperature, leading to reduced emission. In addition, compared to helium, water has lower diffusivity, which contributes to the observed constriction as well (Graham's law of diffusion). However, the emission intensity of H_α decreases at a lesser gradient than that of excited states of helium, thus rendering the fractional intensity ratio of H_α to that of $[H_\alpha + He(x)]$ to attain a positive slope.

Four independent experiments were conducted, and the error bars represent the standard deviation of the four experimental data set(s). The standard deviation of H/He at each molar flow ratio is set as the magnitude of the vertical error bars. Since the actual independent variable is the flow rate of water; there is a minor variation in the molar flow

ratios of water to helium for the same input flow rate of water in each run. This variation results from the manual positioning of the valves to vary the initial flow rate of helium at the desired pressure through the OES cell. The standard deviation in the molar flow ratio for the respective water flow rate(s) is set as the magnitude of the horizontal error bar.
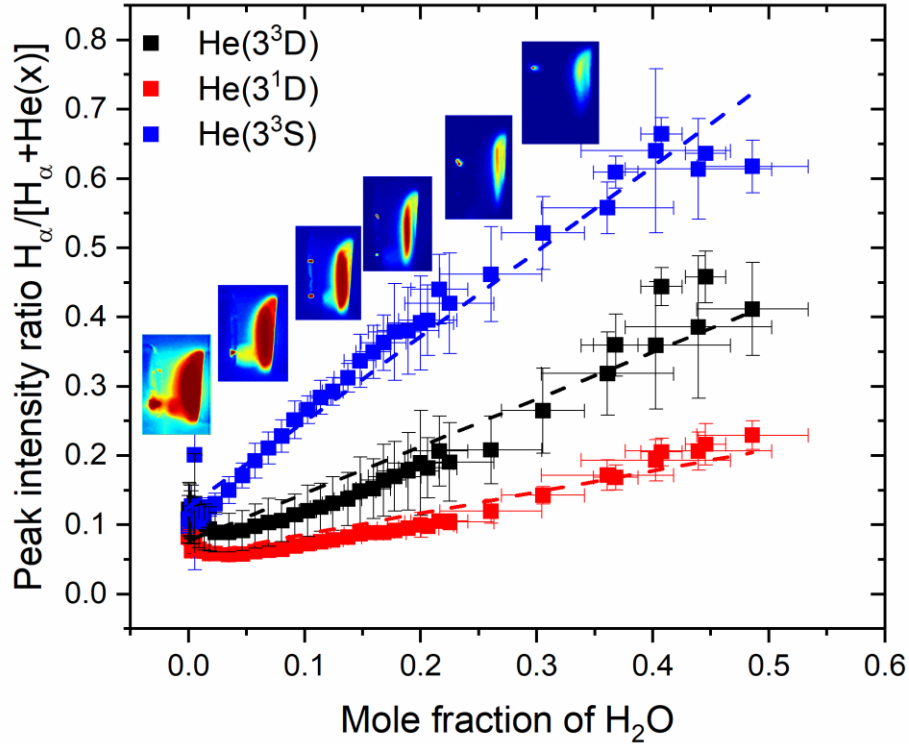
Figure 3.4 Peak normalized emission intensity of H_α as a function of water mole fraction at an operating pressure of 16.5 Torr and discharge current of 2.0 mA. The H_α emission intensity is normalized by $[H_\alpha+He(3^3D)]$, $[H_\alpha+He(3^1D)]$ and $[H_\alpha+He(3^3S)]$ separately

To increase the maximum limit of water loading without possible condensation taking place, additional experiments were conducted at 2.0 Torr for 2.0 mA discharge current. Under low operating pressure(s), the emissions from the helium excited states are slightly different. The emission from $He(3^3S)$ decreases sharply compared to those from

He(3^3D) and He(3^1D). At higher water loading the magnitude of emission intensity at He(3^3S) at 706.5 nm reduces to that of background noise. As a result, at lower pressure and higher water loading, the emission from He(3^3D) and He(3^1D) are employed as detection markers.
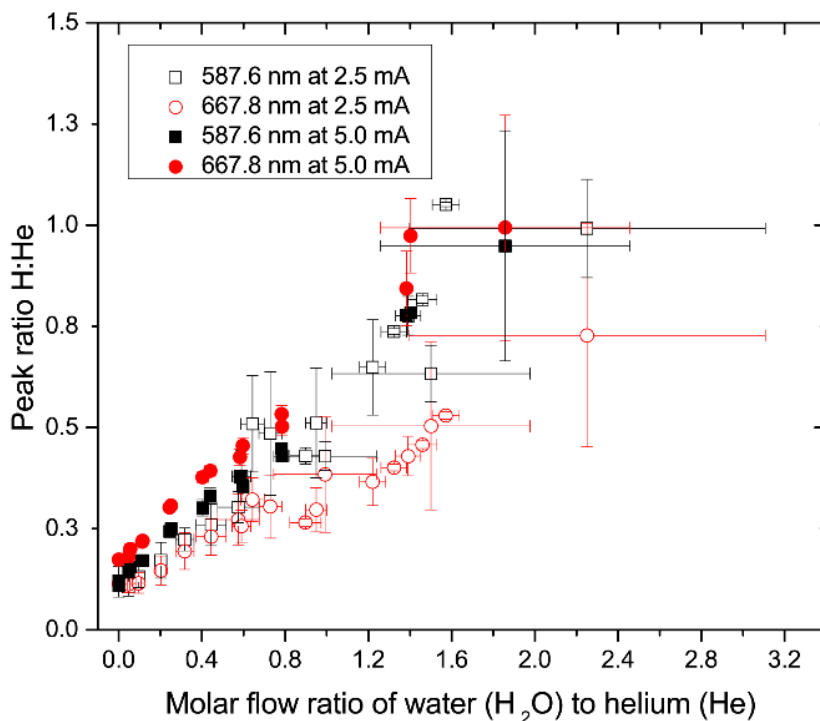
Figure 3.5 Peak ratio of H to He as a function of water to helium molar flow ratio considering the emission intensities from, He(3^3D) and He(3^1D) at discharge currents of 2.5 mA and 5.0 mA

To determine if the calibration will remain independent of the discharge current, the data for two different discharge currents are plotted in the same viewgraph. Figure 3.5 shows the calibration viewgraphs at a 2.0 Torr operating pressure and discharge currents of 2.5 mA and 5.0 mA respectively, considering only the He(3^3D) and He(3^1D) emission intensities. The role of discharge current on the calibration is investigated owing to the fact

that at a higher water concentration, the emission intensity of the helium excited states is found to decrease at a constant discharge current. Increasing the discharge current results in an increase in the cross-sectional area of the negative glow. This is because the experiments were conducted at the 'normal glow' regime in which the current density of the discharge maintains a constant electron, ions, and excited states number density value [58]. Thus, a higher current means the cross-sectional area of the discharge must also increase to keep the current density constant. A larger cross-sectional area/volume of the discharge results in a higher spatially averaged emission intensity acquired by the optical probe but the relative increase in the intensity of H_α with respect to that of each of $He(3^3D)$, $He(3^1D)$, and $He(3^3S)$ is similar. As a consequence, the normalized intensity remains insensitive to the discharge current and pressure. Figure 3.5 shows that for both discharge currents, a linear correlation is maintained well up to the water to helium flow ratio of 1.0. The discontinuity in the 1.0 flow ratio region for both the data is due to the experimental limitation of supplying a continuous flow of water to the discharge cell. Consequently, the experiment cannot be transitioned smoothly from lower to higher concentration range as the flow of helium requires adjustments to allow the formulation of higher concentration mixtures as well as due to the limitation on the capacity of syringes for maintaining a continuous quantifiable flow of water. Water needs to be refilled at around a flow ratio of 1.0. Thus, the linear pattern is slightly perturbed at that point. Similar to the 16.5 Torr pressure condition, when the ratio of water to helium exceeds a certain limit, which in both cases appears to be 1.5, the linear correlation starts to deviate. It is also observed from Figure 3.5 that for 587.6 nm, the calibration curves at both the currents overlap, denoting a discharge current independent calibration process. It further indicates that under

circumstances in which, the intensity magnitude of the signature peaks is reduced, the discharge current can be increased maintaining the same calibration equation for 587.6 nm. Such strong overlapping is not observed in the case of 667.8 nm even though a slight overlapping seems to exist at lower concentrations. For clarity, the regression lines have not been plotted for these graphs.
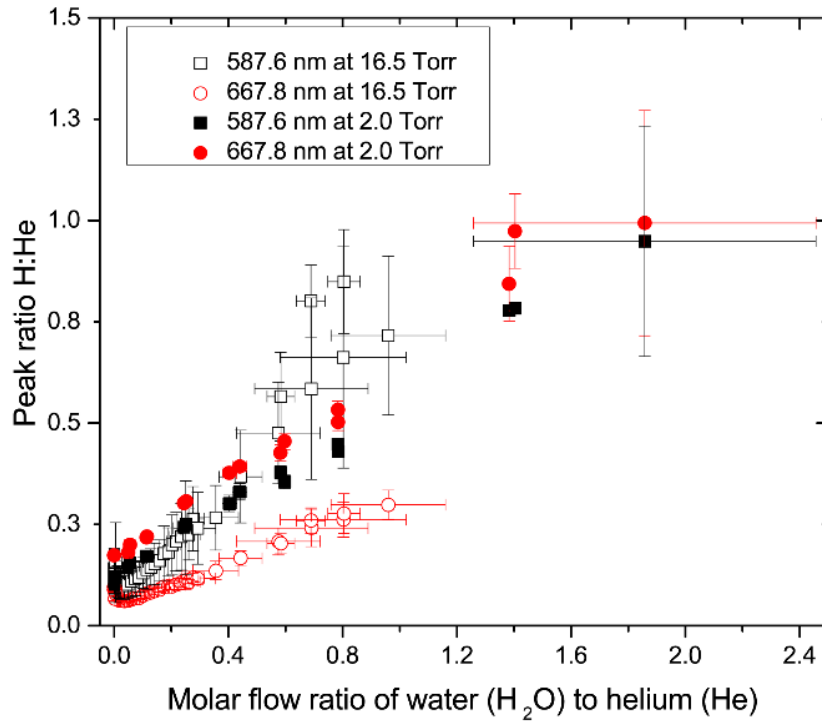
Figure 3.6 Peak ratio of H to He as a function of water to helium molar flow ratio considering the emission intensity from, He(3^3D) and He(3^1D) at operating pressure(s) of 16.5 Torr and 2.0 Torr

The dependence of operating pressure on the calibration was investigated by comparing two sets of data at 2.0 Torr and 16.5 Torr. Figure 3.6 shows that for 587.6 nm, the calibration curves for both pressures collapse on top of each other. However, 667.8 nm shows no such overlapping. Thus, it can be said that the signal strength at 587.6 nm has

fairly strong pressure independence. It is noted that even though the experiments at 16.5 Torr were carried out at 2.0 mA in contrast to 2.5 mA for the 2.0 Torr case, it had been found previously that the 587.6 nm shows discharge current independence. As such, comparing experiments run at different currents for establishing pressure independence is justified. From a different perspective, Figure 3.6 also corroborates the current independence of 587.6 nm since both the plots, even though at different discharge currents, have overlapped with each other.

Conducting the above experiments at 1.0 Torr posed a significant challenge since the carrier gas flow had to be kept very small in a continuous flow system to maintain the pressure at 1.0 Torr. This also caused the reading from the mass flow controller to go into a nonlinear mode of operation.
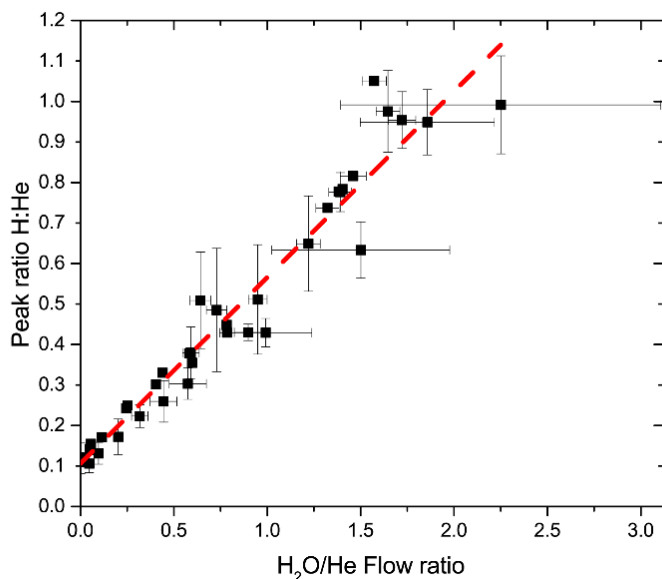
Figure 3.7 Calibration curve encompassing data from discharge currents of 2.5 mA and 5.0 mA at a pressure of 2.0 Torr

A combined calibration curve is plotted from data points of 587.6 nm for 2.5 mA and 5.0 mA, at a pressure of 2.0 Torr in Figure 3.7 since we are mostly interested in the behavior at the low-pressure regime. Again, a strong linear relationship is observed with a correlation of 97%.
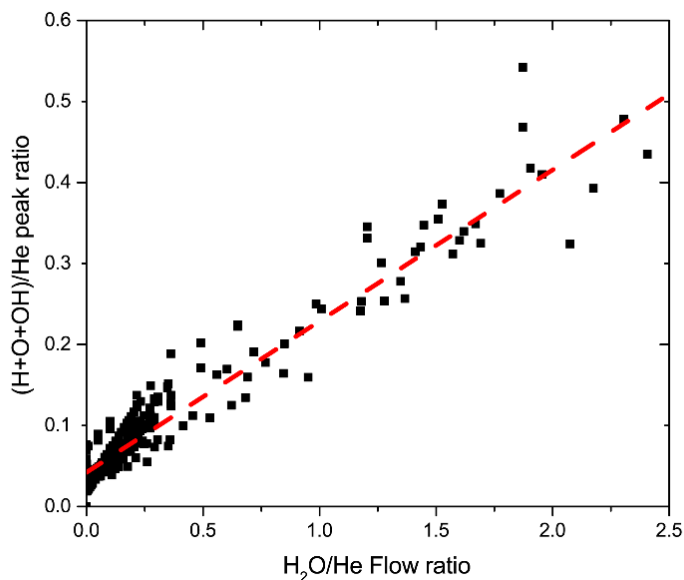
Figure 3.8 Calibration plot encompassing data from every excited species from water and helium from all conditions

A final calibration plot is made by encompassing the wavelengths from each excited species resulting from helium atoms and dissociation of water molecules. The corresponding wavelengths have been tabulated in Appendix A. Figure 3.8 shows the calibration plot by taking into account the ratio of emission intensities from H, O, and OH with respect to those from the excited state of He for every operating pressure and discharge current, studied so far. Since, from previous plots, it had been noted that for 16.5 Torr, condensation causes the data points to deviate beyond the flow ratio of 0.5, those corresponding data points have been omitted. This is depicted by data points being crowded

in the lower concentration regime of the plot. A strong linear correlation is prevalent

between the peak ratio and the molar flow ratio in Figure 3.8 and thus, it can be used as a

measure to cross-validate the calibration plot in Figure 3.7.

3.3.3 HUMIDITY MEASUREMENT
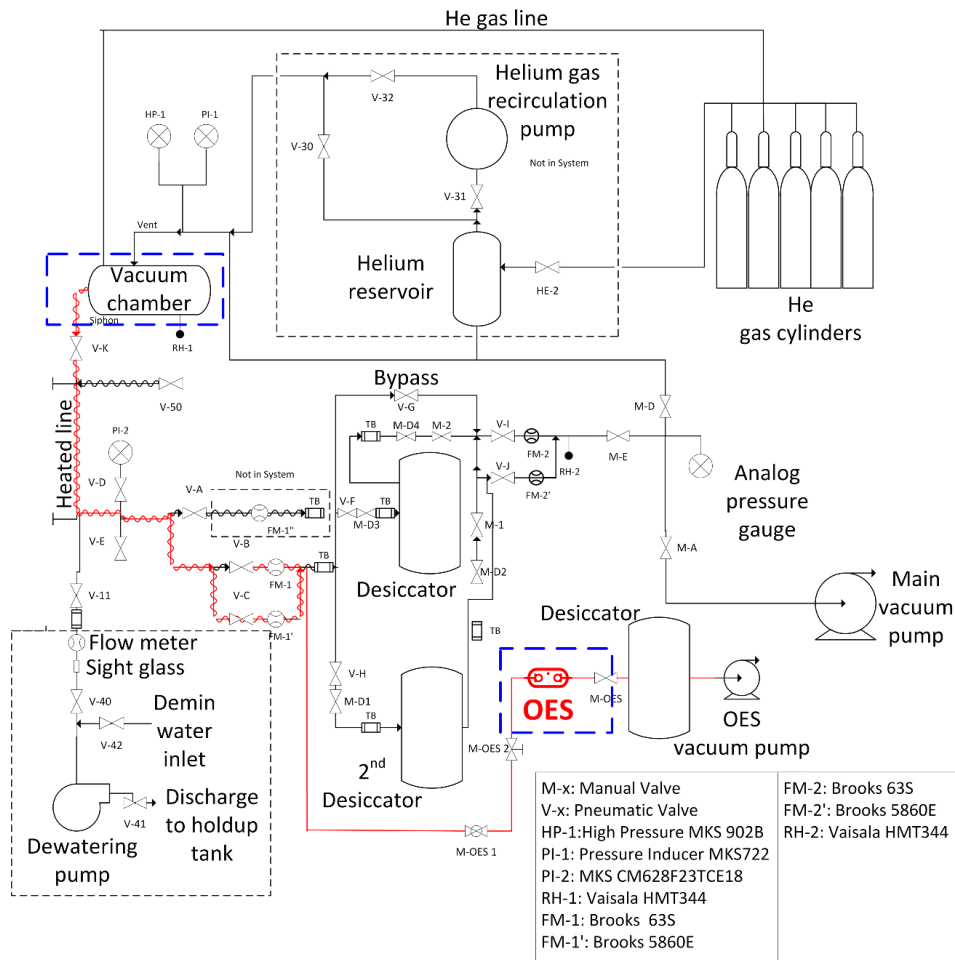
Figure 3.9 Diagram illustrating the flow path and components involved in the vacuum drying process in a mock nuclear fuel rod assembly. The blue dashed boxes denote the location of the vacuum chamber (left) and the plasma OES cell (right)

The plasma discharge cell and the associated diagnostics are connected to a mock

nuclear fuel rod assembly to acquire and detect real-time gas composition data,

representative of a vacuum drying process. A schematic of the large-scale experiment with

the plasma OES cell connected to it is shown in Figure 3.9. Details of the mock nuclear

fuel rod drying experiment are provided in [59]. The fuel rod assembly cask, which has a

volume of 484 liters is wetted with a known amount of water. The cask is then purged and

pressurized to one atmosphere with helium and then progressively vacuumed in multiple

stages to promote the drying process. A small stream of outflow gas from the cask is bled

off into the OES cell, maintained at a pressure of 2 Torr in which, the emission intensity is

measured. The details of this experimental setup and procedure have been discussed in

[59, 60]
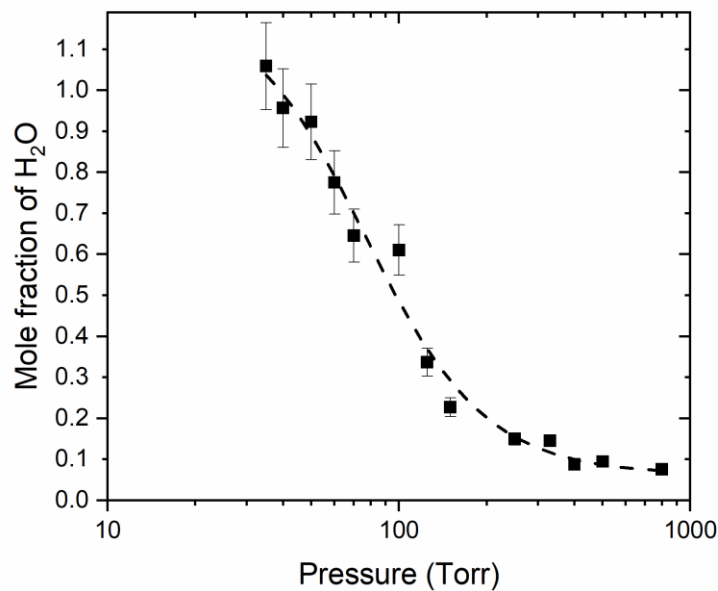
Figure 3.10 Variation of water concentration as a function of different pressure
conditions observed by the fuel casket during the vacuum drying process

Figure 3.10 shows the water vapor concentration as a function of vacuum pressure

in the mock fuel rod assembly. The water concentration was determined from the extensive

database of the water vapor emission signals for water vapor quantification for ranges of

current and pressure showing the variation of H_α to $[H_\alpha + He(3^3D)]$. It is observed that up to ~250 Torr, the concentration of water vapor remains mostly unchanged but increases exponentially thereafter. The plot also shows that below 30 Torr, the resulting pressure is predominantly the partial pressure of water vapor; reconfirmed by measurements by relative humidity sensors. It is to be noted that even though the existing signal marker database accounts for a maximum of 0.65 mole fraction of water, this database has been extrapolated to quantify mole fractions as high as 1.0. The validity of this extrapolation stems from the strong linear correlation between the normalized ratio of the signal intensity and the concentration of water.

3.4 CONCLUSIONS

In summary, a plasma based optical emission spectroscopy technique has been developed for detecting and quantifying water vapor concentration in moisture enriched flow conditions. The normalized fractional intensity of H_α was identified to have a strong linear dependency on the water vapor content in the gas stream and therefore was selected as a detection and quantification marker. It was further found that the normalized intensity was independent of the plasma discharge current conditions in the "normal glow" regime of operation of the discharge as well as the vacuum operating pressure.

The proposed method has been applied to characterize outflow gases from a mock nuclear used fuel assembly. Based on the experimental outcome, it has been observed that the OES has been successful in capturing the physics of the system by portraying the trend in the composition of the gaseous mixture with decreasing pressure.

In the future, there is scope to investigate the capability of the OES as a mass flow meter (MFM) for water vapor. For a fixed setting of the valves, which will allow a specific amount of flow of carrier gas, it is potentially possible to calibrate the signals in the OES with respect to the absolute amount of water flow rate. The advantage of OES over conventional MFM(s) is that OES is not limited by the temperature it can be subjected to. The current OES system can also be applied to different gas mixtures like air-water for measuring humidity in a non-intrusive method.

3.5 ACKNOWLEDGEMENT

3.6 REFERENCES

2.   Staack, D.A., *Characterization and stabilization of atmospheric pressure DC microplasmas and their application to thin film deposition.* 2009.

42.   Commission, U.S.N.R., *Standard Review Plan for Dry Cask Storage*. 1997, Office of Nuclear Material Safety and Safeguards: Washington, DC 20555-0001.

43.   X. He, R.B., Y.-M. C. L. Pan, P. Shukla, K. Chiang, R. Pabalan, G. Willden and D. Vickers, *Available Methods for Functional Monitoring of Dry Cask Storage Systems*. 2014, U.S. Nuclear Regulatory Commission Contract NRC–HQ–12–C–02–0089.

44.   Ren, Y., C. Wang, and Y. Qiu, *Aging of surface properties of ultra high modulus polyethylene fibers treated with He/O 2 atmospheric pressure plasma jet.* Surface and Coatings Technology, 2008. **202**(12): p. 2670-2676.

45.   O'Connell, D., L. Cox, W. Hyland, S. McMahon, S. Reuter, W. Graham, T. Gans, and F. Currell, *Cold atmospheric pressure plasma jet interactions with plasmid DNA.* Applied Physics Letters, 2011. **98**(4): p. 043701.

46.   Tian, L., H. Nie, N.P. Chatterton, C.J. Branford-White, Y. Qiu, and L. Zhu, *Helium/oxygen atmospheric pressure plasma jet treatment for hydrophilicity improvement of grey cotton knitted fabric.* Applied Surface Science, 2011. **257**(16): p. 7113-7118.

47.   H. S. Uhm, Y.C.H., *Various microplasma jets and their sterilization of microbes.* Thin Solid Films, 2011. **519**: p. 6974-6980.

48.   Fukuhara, D., S. Namba, K. Kozue, T. Yamasaki, and K. Takiyama, *Characterization of a Microhollow Cathode Discharge Plasma in Helium or Air with Water Vapor.* Plasma Science and Technology, 2013. **15**(2): p. 129-132.

49.   Yonemori, S., Y. Nakagawa, R. Ono, and T. Oda, *Measurement of OH density and air–helium mixture ratio in an atmospheric-pressure helium plasma jet.* Journal of Physics D: Applied Physics, 2012. **45**(22): p. 225202.

50.   Levko, D., A. Shuaibov, I. Shevera, R. Gritzak, and A. Tsymbaliuk, *Use of a low pressure helium/water vapor discharge as a mercury-free source of ultraviolet emission.* Journal of Applied Physics, 2014. **116**(11): p. 113303.

51.   Andrawes, F.F., *Determination of trace levels of water in gaseous samples by gas chromatography with helium ionization detection.* Analytical Chemistry, 1983. **55**: p. 1869-1872.

52.   S. Hanamura, B.K., J. D. Winefordner, *Determination of trace levels of water in solid samples by evolved gas analysis/helium microwave plasma emission spectrometry.* Analytical Chemistry, 1985. **57**: p. 9-13.

53.   Verreycken, T., R.M. van der Horst, A.H.F.M. Baede, E.M. Van Veldhuizen, and P.J. Bruggeman, *Time and spatially resolved LIF of OH in a plasma filament in atmospheric pressure He–H2O.* Journal of Physics D: Applied Physics, 2012. **45**(4): p. 045205.

54.   Liu, D.X., P. Bruggeman, F. Iza, M.Z. Rong, and M.G. Kong, *Global model of low-temperature atmospheric-pressure He + H 2 O plasmas.* Plasma Sources Science and Technology, 2010. **19**(2): p. 025018.

55.	Mayeresse, Y., R. Veillon, P. Sibille, and C. Nomine, *Freeze-drying process monitoring using a cold plasma ionization device.* PDA Journal of Pharmaceutical Science and Technology, 2007. **61**(3): p. 160.

56.	Sainct, F., D. Lacoste, M. Kirkpatrick, E. Odic, and C. Laux, *Experimental study of nanosecond repetitively pulsed discharges in water vapor.*

57.	Sainct, F.P., D.A. Lacoste, M.J. Kirkpatrick, E. Odic, and C.O. Laux, *Temporal evolution of temperature and OH density produced by nanosecond repetitively pulsed discharges in water vapour at atmospheric pressure.* Journal of Physics D: Applied Physics, 2014. **47**(7): p. 075204.

58.	Farouk, T., B. Farouk, D. Staack, A. Gutsol, and A. Fridman, *Simulation of dc atmospheric pressure argon micro glow-discharge.* Plasma Sources Science and Technology, 2006. **15**(4): p. 676.

59.	Knight, T.W., J. Khan, T. Farouk, J. Tulenko. *Experimental Determination of Used Fuel Vacuum Drying Using a Mock Fuel Assembly*. in *International High-Level Radioactive Waste Management Conference*. 2017. Charlotte, NC: American Nuclear Society.

60.	Shalloo, M., T. Knight, J. Khan, T. Farouk, J. Tulenko. *Vacuum Drying Experiments using a Mock Used Fuel Assembly*. in *Transactions Of the American Nuclear Society 2017 Winter Meeting*. 2017. Washington, DC: American Nuclear Society.

CHAPTER 4 :

INSTABILITIES IN MODERATE PRESSURE DC DRIVEN NITROGEN GLOW DISCHARGE[2]

4.1 INTRODUCTION

The self-organized formation of spatial light emission patterns has been a research topic due to its impact on various plasma systems operating in low to atmospheric pressure range, with either a dc or rf source for a wide range of discharge parameters [61-63]. Self-organized spatial multi-layered structures – appearing as alternating bright and dark areas along the discharge current are usually termed '*stratification*'. Two types of striations have been observed: '*standing*' striations exist in the form of stationary damping oscillations in the vicinity of electrodes; '*moving*' striations exist in the form of traveling waves with speeds in the order of 10-10^3 ms^{-1} [64]. These striations have been observed at low and high gas pressures for dc and rf glow discharges [65-69]. One of the most commonly observed striation patterns is the striated positive column of a dc glow discharge. The ionization waves or ion-acoustic waves have been identified to drive the observed phenomenon [62, 70]. Plasma stratification in dc discharges has been studied extensively in the past [71, 72] for low and moderate pressures, at $PR < 10$ Torr-cm (P is operating pressure and R is the discharge tube radius). In recent years, studies have been conducted for high-pressure micro glow discharges at PR up to ~ 25 Torr-cm [68]. Mathematical models, including both fluid [73, 74] and kinetic models [62, 65, 69, 75, 76], have been developed to simulate the striations phenomena. A comprehensive review of instabilities in molecular and electronegative plasmas was presented by Haas [74], who emphasized the importance of negative ions in the formation of the striated structures. Nighan and Wiegand [73] further demonstrated conditions conducive to electron-attachment processes forming negative ions comparable to the electron number density in the system to trigger striations. Recent studies

58

considering kinetic effects [75, 77] have predicted moving striations for monoatomic gases where negative ions are not present.

Arslanbekov and Kolobov [75] conducted two-dimensional simulations of an argon dc glow discharge operating at moderate pressure (2 Torr) and high currents (~ 100 mA). The model predicted the formation of moving striations near the Pupp boundary resulting from the nonlinear dependence of the ionization and excitation rates on electron density caused by the "Maxwellization" of the high energy part of the electron energy distribution function. In a recent study, the same authors [78] demonstrated the influence of the volumetric recombination rate on the striation patterns and structures under similar operating conditions. Kawamura et al. [69] conducted particle in cell (PIC) simulations of atmospheric pressure dc and rf discharges operating in helium with trace water vapor (He/H_2O). It was found that bulk recombination and non-local effects can trigger instability and plasma stratification.

Desangles et al. [79] studied the striations in the argon rf discharge using a modified electron fluid model with a 0-d Boltzmann solver. A linear stability analysis showed that the stratification is driven by Soret and Dufour effects in the electron and electron energy transport. The analysis also shows that the striation phenomena strongly depend on the sign (i.e., negative versus positive) of the Soret and Dufour fluxes. In earlier work, Urbankova et al. [80] conducted a similar analysis and identified that for moderate/low-pressure dc discharge operating in a diatomic gas, the thermal diffusion of electrons plays the most critical role in triggering standing wave striations. Hjalmar et al. [81] had computationally studied striations in low-pressure rf argon plasma and compared them with experiments; however, no discerning factor regarding the formation mechanism of the striations was

identified. Computational analysis of striations in capacitively coupled rf plasma for CF_4 gas was conducted by Liu et al. [82]; the authors attributed the formation of the striation structures to the spatially generated local space charge that is formed from the periodic acceleration of ions by the rf electric field [82]. Iza et al. [83] conducted two-dimensional PIC simulations of plasma display panels, where striations were formed due to a combined effect of volume processes and surface charge accumulation. In magnetized micro discharges, striations have been observed to appear in both homogeneous and non-homogeneous magnetic fields [84]. Their analysis shows that the growth of the instability is connected to the ionization process and can be suppressed by either increasing the plasma density or decreasing the magnetic field. Several numerical studies on the non-local electron kinetics leading to striations have also been reported in the literature [85-87]. In a recent study, Levko [88] conducted one-dimensional PIC simulations of standing and moving striations in low-pressure dc and rf argon discharges; however, no mechanism of stratification has been identified.

Despite many theoretical and modeling studies conducted to elucidate striation behavior for several feed gases, modeling striations in diatomic gases has been very limited. Sigeneger et al. [89] attempted to study the non-local electron kinetics in spherical glow discharges in nitrogen (N_2) by solving a spatially inhomogeneous Boltzmann equation for a given distribution of the electric field. Thus, self-consistent numerical modeling of striations in diatomic gases has not been performed so far.

In this work, we report the results of a one-dimensional model to simulate low/moderate pressure dc glow discharge in nitrogen. A detailed chemistry model is assembled that includes elastic scattering, ionization, volumetric recombination, multi-

level vibrational excitation, and de-excitation, as well as electronic excitation and de-excitation. The reaction rate constants and transport coefficients of electrons have been obtained from a multi-term Spherical Harmonics Expansion (SHE) solution of the local Boltzmann equation. This study aims to understand the physicochemical processes responsible for plasma stratification in dc nitrogen glow discharge. Experiments are conducted to obtain the voltage-current characteristics and record the visual appearance of the striations. The presentation in this paper is as follows: Section 2 provides a brief description of the discharge system that is being simulated and the mathematical model for the same; section 3 details the chemical kinetics; section 4 discusses the experimental setup, followed by results and discussions in section 5 and a summary with conclusions in section 6.

4.2 MATHEMATICAL MODEL AND PROBLEM GEOMETRY

The mathematical model employed provides a 1-D representation of the discharge phenomena. The model resolves the temporal and spatial variation/distribution of the discharge in the direction perpendicular to the electrode plane (Figure 4.1). The discharge model consists of coupled conservation equations for the different species – electrons, ions, and neutrals, as well as electron energy. The electric field is self consistently obtained from the solution of Poisson's equation. An external circuit model is utilized to vary the plasma load. The external circuit consists of a simple RC circuit, in which the cathode is grounded, and the voltage is applied to the anode through the circuit (Figure 4.1). The capacitance, C_p represents the parasitic capacitance (0.1 pF) of the connecting wires in the circuit. The ballast resistance, $R_{Ballast}$, is varied to control the discharge current, hence, the plasma density. The inter-electrode separation distance (L) is fixed at 15.5 cm and the

diameter of each electrode is set as 1.1 cm resulting in a surface area of 0.95 cm^2, required for calculating the discharge current of the system. Widely used flux boundary conditions for electrons, ions, and electron energy is prescribed. $\gamma = 0.1$ is used as the secondary electron emission coefficient.
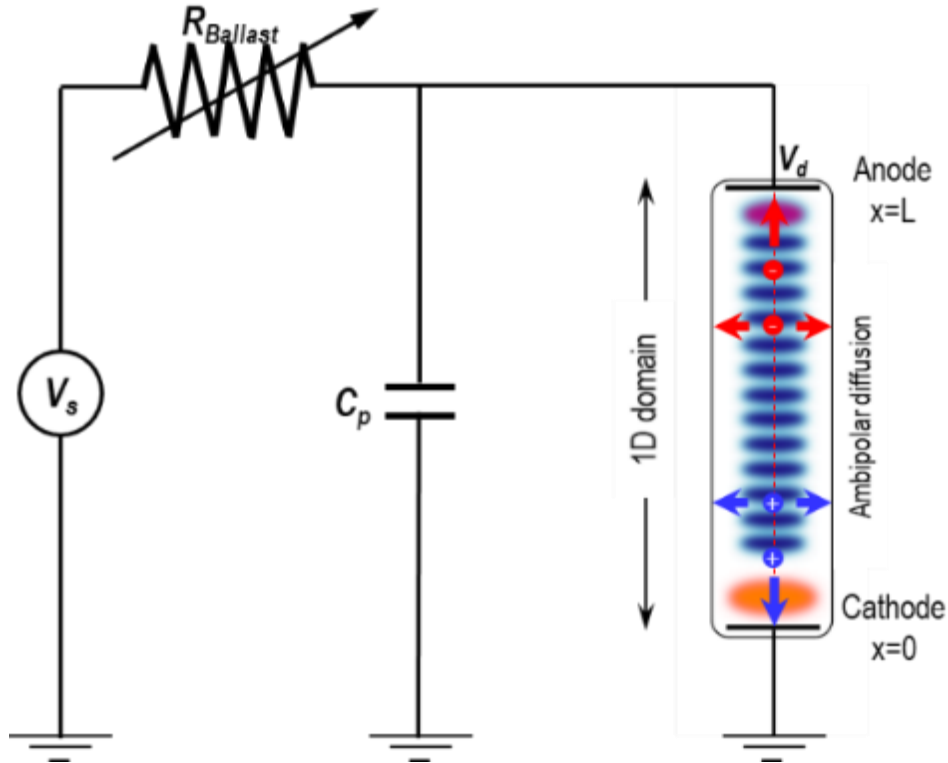
Figure 4.1 Schematic of the parallel plate plasma glow discharge circuit together with the 1-D computational domain

4.3 MATHEMATICAL MODEL OF THE DISCHARGE

The details of all the governing equations, boundary conditions, and the external circuit model coupling have been reported in our prior publications [90, 91]. Additional source terms include the ambipolar losses of electrons, ions, and mean electron energy, which are incorporated into the species conservation equation as: $\frac{n_e}{\tau_d}, \frac{n_i}{\tau_d}, \frac{n_e\varepsilon}{\tau_d}$, where, n is

species number density, subscripts e and i denote electrons and ions respectively, and ε is the mean electron energy. The ambipolar diffusion time scale is denoted by $\tau_d(x) = \frac{\Lambda^2}{D_a(x)}$, where $\Lambda = \frac{R_{tube}}{2.4}$ is the transverse discharge length (R_{tube} is the tube or discharge radius) [88, 92], and $D_a(x)$ is the ambipolar diffusion coefficient calculated from [93], where μ is the mobility, D is the diffusion coefficient.

$$D_a(x) = \frac{\mu_e\left(\frac{1}{\sum n_i}\sum n_i\, D_i\right) + \left(\frac{1}{\sum n_i}\sum n_i\, \mu_i\right) D_e}{\mu_e + \left(\frac{1}{\sum n_i}\sum n_i\, \mu_i\right)}$$

The system of equations is discretized based on the finite element method and is solved using a time-dependent solver in COMSOL version 5.3a [94]. A non-uniform mesh is employed with denser grids near the electrodes to resolve the sheaths. The domain is decomposed with 400 non-uniform grids with higher mesh density near the electrode surfaces, for which a grid-independent solution was achieved. The time integration is performed using a fully implicit backward difference formula (BDF) with variable time stepping. The solutions are obtained using the MUMPS (Multifrontal Massively Parallel Sparse) solver.

4.4 GAS PHASE CHEMICAL KINETICS

The chemical kinetic model contains both electron-induced and heavy particle reactions for nitrogen feed gas. A total of 22 species are considered in the simulations, including electrons, ions, vibrational and electronically excited states, and ground-state neutrals (see Table 4.1).

Table 4.1 Different species considered in the dc driven nitrogen plasma model

Category	Species
Electrons	e
Ions	N^+, N_2^+, N_4^+
Vibrationally excited states	$N_{2,v=1}$, $N_{2,v=2}$, $N_{2,v=3}$, $N_{2,v=4}$, $N_{2,v=5}$, $N_{2,v=6}$, $N_{2,v=7}$, $N_{2,v=8}$, $N_{2,v=9}$, $N_{2,v=10}$, $N_{2,v=11}$, $N_{2,v=12}$, $N_{2,v=13}$, $N_{2,v=14}$, $N_{2,v=15}$
Electronically excited states	$N_2\ (A^3\Sigma)$
Neutrals	N, N_2

A total of 73 gas-phase reactions are considered as listed in Table 4.2. They are grouped into two categories – electron-induced and heavy particle reactions. The electron-induced reactions include elastic scattering, vibrational excitation, electronic excitation, ionization, recombination, de-excitation reactions, as well as super elastics collisions. The heavy particle reactions include charge transfer, de-excitation, dissociation, and dissociative de-excitation reactions. The wall reactions involving the deactivation of the excited species at the electrode surfaces are presented in Table 4.3.

Table 4.2 Gas-phase reaction mechanism

#	Reaction	Reaction Rate Coefficient	Ref.
Electron induced reactions			
R1	$e + N_2 \rightarrow e + N_2$	$f(\varepsilon)$	[95]
R2	$e + N_2 \rightarrow e + N$	$f(\varepsilon)$	[96]
R3	$e + N_2 \rightarrow e + N_{2,v=1}$	$f(\varepsilon)$	[95]
R4	$e + N_2 \rightarrow e + N_{2,v=2}$	$f(\varepsilon)$	[95]
R5	$e + N_2 \rightarrow e + N_{2,v=3}$	$f(\varepsilon)$	[95]
R6	$e + N_2 \rightarrow e + N_{2,v=4}$	$f(\varepsilon)$	[95]
R7	$e + N_2 \rightarrow e + N_{2,v=5}$	$f(\varepsilon)$	[95]
R8	$e + N_2 \rightarrow e + N_{2,v=6}$	$f(\varepsilon)$	[95]
R9	$e + N_2 \rightarrow e + N_{2,v=7}$	$f(\varepsilon)$	[95]

R10	$e + N_2 \rightarrow e + N_{2,v=8}$	$f(\varepsilon)$	[95]
R11	$e + N_2 \rightarrow e + N_{2,v=9}$	$f(\varepsilon)$	[95]
R12	$e + N_2 \rightarrow e + N_{2,v=10}$	$f(\varepsilon)$	[95]
R13	$e + N_2 \rightarrow e + N_{2,v=11}$	$f(\varepsilon)$	[95]
R14	$e + N_2 \rightarrow e + N_{2,v=12}$	$f(\varepsilon)$	[95]
R15	$e + N_2 \rightarrow e + N_{2,v=13}$	$f(\varepsilon)$	[95]
R16	$e + N_2 \rightarrow e + N_{2,v=14}$	$f(\varepsilon)$	[95]
R17	$e + N_2 \rightarrow e + N_{2,v=15}$	$f(\varepsilon)$	[95]
R18	$e + N_2 \rightarrow e + N_2(A^3\Sigma)$	$f(\varepsilon)$	[95]
R19	$e + N_{2,v=1} \rightarrow e + N_2(A^3\Sigma)$	$f(\varepsilon)$	[97]
R20	$e + N_{2,v=1} \rightarrow e + N_2$	$f(\varepsilon)$	[97]
R21	$e + N_2(A^3\Sigma) \rightarrow e + N_{2,v=1}$	$f(\varepsilon)$	[97]
R22	$e + N_2(A^3\Sigma) \rightarrow e + N_2$	$f(\varepsilon)$	[97]
R23	$e + N_2 \rightarrow 2e + N_2^+$	$f(\varepsilon)$	[95]
R24	$e + N_{2,v=1} \rightarrow 2e + N_2^+$	$f(\varepsilon)$	[97]
R25	$e + N \rightarrow 2e + N^+$	$f(\varepsilon)$	[96]
R26	$2e + N_2^+ \rightarrow e + N_2$	$1 \times 10^{-31} \left(\frac{T_g}{T_e}\right)^{4.5}$ Ж	[37]
R27	$2e + N^+ \rightarrow e + N$	$1 \times 10^{-31} \left(\frac{T_g}{T_e}\right)^{4.5}$ Ж	[37]
R28	$e + N_4^+ \rightarrow 2N + N_2$	$3.13 \times 10^{-13}(T_e)^{-0.41}$	[98]
R29	$e + N_2^+ \rightarrow 2N$	$2.36 \times 10^{-14}(T_e)^{-0.51}$	[99]

Heavy particle reactions

R30	$N_2^+ + 2N_2 \rightarrow N_2 + N_4^+$	1.90×10^{-41} Ж	[100]
R31	$N_4^+ + N \rightarrow 2N_2 + N^+$	1.00×10^{-17}	[37]
R32	$N_2 + N_2 \rightarrow 2N + N_2$	$6.2 \times 10^{-9} \times (T_g)^{-1.6}$ $\times exp\left(\frac{-113000}{T_g}\right)$	[101]
R33	$N_2 + N_{2,v=1} \rightarrow 2N + N_2$	$6.2 \times 10^{-9} \times (T_g)^{-1.6}$ $\times exp\left(\frac{-113000}{T_g}\right)$	*

R34 $N_2 + N_{2,v=2} \rightarrow 2N + N_2$ $\begin{aligned}6.2 \times 10^{-9} \times (T_g)^{-1.6} \\ \times exp\left(\dfrac{-113000}{T_g}\right)\end{aligned}$ *

R35 $N_2 + N_{2,v=3} \rightarrow 2N + N_2$ $\begin{aligned}6.2 \times 10^{-9} \times (T_g)^{-1.6} \\ \times exp\left(\dfrac{-113000}{T_g}\right)\end{aligned}$ *

R36 $N_2 + N_{2,v=4} \rightarrow 2N + N_2$ $\begin{aligned}6.2 \times 10^{-9} \times (T_g)^{-1.6} \\ \times exp\left(\dfrac{-113000}{T_g}\right)\end{aligned}$ *

R37 $N_2 + N_{2,v=5} \rightarrow 2N + N_2$ $\begin{aligned}6.2 \times 10^{-9} \times (T_g)^{-1.6} \\ \times exp\left(\dfrac{-113000}{T_g}\right)\end{aligned}$ *

R38 $N_2 + N_{2,v=6} \rightarrow 2N + N_2$ $\begin{aligned}6.2 \times 10^{-9} \times (T_g)^{-1.6} \\ \times exp\left(\dfrac{-113000}{T_g}\right)\end{aligned}$ *

R39 $N_2 + N_{2,v=7} \rightarrow 2N + N_2$ $\begin{aligned}6.2 \times 10^{-9} \times (T_g)^{-1.6} \\ \times exp\left(\dfrac{-113000}{T_g}\right)\end{aligned}$ *

R40 $N_2 + N_{2,v=8} \rightarrow 2N + N_2$ $\begin{aligned}6.2 \times 10^{-9} \times (T_g)^{-1.6} \\ \times exp\left(\dfrac{-113000}{T_g}\right)\end{aligned}$ *

R41 $N_2 + N_{2,v=9} \rightarrow 2N + N_2$ $\begin{aligned}6.2 \times 10^{-9} \times (T_g)^{-1.6} \\ \times exp\left(\dfrac{-113000}{T_g}\right)\end{aligned}$ *

R42 $N_2 + N_{2,v=10} \rightarrow 2N + N_2$ $\begin{aligned}6.2 \times 10^{-9} \times (T_g)^{-1.6} \\ \times exp\left(\dfrac{-113000}{T_g}\right)\end{aligned}$ *

R43 $N_2 + N_{2,v=11} \rightarrow 2N + N_2$ $\begin{aligned}6.2 \times 10^{-9} \times (T_g)^{-1.6} \\ \times exp\left(\dfrac{-113000}{T_g}\right)\end{aligned}$ *

R44 $N_2 + N_{2,v=12} \rightarrow 2N + N_2$ $\begin{aligned}6.2 \times 10^{-9} \times (T_g)^{-1.6} \\ \times exp\left(\dfrac{-113000}{T_g}\right)\end{aligned}$ *

R45 $N_2 + N_{2,v=13} \rightarrow 2N + N_2$ $\begin{aligned}6.2 \times 10^{-9} \times (T_g)^{-1.6} \\ \times exp\left(\dfrac{-113000}{T_g}\right)\end{aligned}$ *

R46 $N_2 + N_{2,v=14} \rightarrow 2N + N_2$ $\begin{aligned}6.2 \times 10^{-9} \times (T_g)^{-1.6} \\ \times exp\left(\dfrac{-113000}{T_g}\right)\end{aligned}$ *

R47	$N_2 + N_{2,v=15} \rightarrow 2N + N_2$	$6.2 \times 10^{-9} \times (T_g)^{-1.6}$ $\times exp\left(\dfrac{-113000}{T_g}\right)$	*
R48	$N_2 + N_2(A^3\Sigma) \rightarrow 2N + N_2$	$6.2 \times 10^{-9} \times (T_g)^{-1.6}$ $\times exp\left(\dfrac{-113000}{T_g}\right)$	*
R49	$N_2 + N_{2,v=1} \rightarrow 2N_2$	0.80×10^{-27}	[102]
R50	$N_2 + N_{2,v=2} \rightarrow N_{2,v=1} + N_2$	1.80×10^{-27}	[102]
R51	$N_2 + N_{2,v=3} \rightarrow N_{2,v=2} + N_2$	3.10×10^{-27}	[102]
R52	$N_2 + N_{2,v=4} \rightarrow N_{2,v=3} + N_2$	5.00×10^{-27}	[102]
R53	$N_2 + N_{2,v=5} \rightarrow N_{2,v=4} + N_2$	7.40×10^{-27}	[102]
R54	$N_2 + N_{2,v=6} \rightarrow N_{2,v=5} + N_2$	1.10×10^{-26}	[102]
R55	$N_2 + N_{2,v=7} \rightarrow N_{2,v=6} + N_2$	1.60×10^{-26}	[102]
R56	$N_2 + N_{2,v=8} \rightarrow N_{2,v=7} + N_2$	2.60×10^{-26}	[102]
R57	$N_2 + N_{2,v=9} \rightarrow N_{2,v=8} + N_2$	3.80×10^{-26}	[102]
R58	$N_2 + N_{2,v=10} \rightarrow N_{2,v=9} + N_2$	5.70×10^{-26}	[102]
R59	$N_2 + N_{2,v=11} \rightarrow N_{2,v=10} + N_2$	8.50×10^{-26}	[102]
R60	$N_2 + N_{2,v=12} \rightarrow N_{2,v=11} + N_2$	1.28×10^{-25}	[102]
R61	$N_2 + N_{2,v=13} \rightarrow N_{2,v=12} + N_2$	1.93×10^{-25}	[102]
R62	$N_2 + N_{2,v=14} \rightarrow N_{2,v=13} + N_2$	2.91×10^{-25}	[102]
R63	$N_2 + N_{2,v=15} \rightarrow N_{2,v=14} + N_2$	4.38×10^{-25}	[102]
R64	$N_2 + N_2(A^3\Sigma) \rightarrow 2N_2$	3.50×10^{-27}	**[100]
R65	$N_{2,v=1} + N_2 \rightarrow N_2 + N_{2,v=1}$	1.00×10^{-20}	[103]
R66	$N_{2,v=1} + N_{2,v=1} \rightarrow N_2 + N_{2,v=2}$	2.00×10^{-20}	[103]
R67	$N_{2,v=1} + N_{2,v=2} \rightarrow N_2 + N_{2,v=3}$	3.00×10^{-20}	[103]
R68	$N_{2,v=1} + N_{2,v=3} \rightarrow N_2 + N_{2,v=4}$	3.50×10^{-20}	[103]
R69	$N_{2,v=1} + N_{2,v=4} \rightarrow N_2 + N_{2,v=5}$	3.65×10^{-20}	[103]
R70	$N_{2,v=1} + N_{2,v=5} \rightarrow N_2 + N_{2,v=6}$	3.60×10^{-20}	[103]
R71	$N_{2,v=1} + N_{2,v=6} \rightarrow N_2 + N_{2,v=7}$	3.25×10^{-20}	[103]
R72	$N_{2,v=1} + N_{2,v=7} \rightarrow N_2 + N_{2,v=8}$	3.00×10^{-20}	[103]
R73	$N_{2,v=1} + N_{2,v=8} \rightarrow N_2 + N_{2,v=9}$	2.50×10^{-20}	[103]

$f(\varepsilon)$: reaction rate obtained from EEDF with associated cross-section data. All rate coefficients are in units m^3s^{-1} except for 3-body reactions denoted by 'Ж' in which cases, rate coefficients are in units: m^6s^{-1}

Key: *based on similarity to R32. **: based on similarity to reactions in reference [100].

Table 4.3 Wall reactions

Process	Reaction	Process (contd.)	Reaction (contd.)
W1	$N_2^+ \rightarrow N_2$	W11	$N_{2,v=7} \rightarrow N_2$
W2	$N^+ \rightarrow 0.5N_2$	W12	$N_{2,v=8} \rightarrow N_2$
W3	$N_4^+ \rightarrow 2N_2$	W13	$N_{2,v=9} \rightarrow N_2$
W4	$N \rightarrow 0.5N_2$	W14	$N_{2,v=10} \rightarrow N_2$
W5	$N_{2,v=1} \rightarrow N_2$	W15	$N_{2,v=11} \rightarrow N_2$
W6	$N_{2,v=2} \rightarrow N_2$	W16	$N_{2,v=12} \rightarrow N_2$
W7	$N_{2,v=3} \rightarrow N_2$	W17	$N_{2,v=13} \rightarrow N_2$
W8	$N_{2,v=4} \rightarrow N_2$	W18	$N_{2,v=14} \rightarrow N_2$
W9	$N_{2,v=5} \rightarrow N_2$	W19	$N_{2,v=15} \rightarrow N_2$
W10	$N_{2,v=6} \rightarrow N_2$	W20	$N_2(A^3\Sigma) \rightarrow N_2$

A large number of the reactions listed in Table 4.2. have cross-section data; the majority of these data pertaining to excitation and ionization of the molecular N_2 is obtained from the Biagi database [95, 104, 105] and that of atomic N is obtained from the IST-Lisbon database [96, 106]. However, while solving the Boltzmann equation (BE) for the electron energy distribution function (EEDF), all the electron-induced reactions pertaining to each specific species from the respective databases are considered (see Appendix C). The detailed subset of electron-induced reactions allows accurately resolving of the EEDF with its salient features along with the resulting rate constants and transport

parameters. However, for the one-dimensional simulation, only the reactions listed Table 4.2 and Table 4.3 are considered to reduce the computational overhead – an approach that was adopted in prior works [107, 108]. Electron-electron collisions are ignored since the discharge currents in the model are in the range of milliamperes as coulomb collisions become pertinent only at very high currents.

Most fluid models incorporate the rate and transport coefficients that are calculated from BE models, which utilize input data in the form of electron-neutral cross-sections to produce macroscopic rate and transport coefficients. The cross-sections utilized in the kinetic calculation and the fidelity of the BE model both exhibit a degree of influence over the model predictions. The spherical harmonics expansion in velocity space is usually truncated to only two first terms when solving the BE. Such models are referred to as two-term BE models, while BE models that consider more than two spherical harmonics terms are referred to as multi-term BE models. Qualitatively, the truncation to only two spherical harmonics terms assumes that the velocity distribution of the electrons is close to isotropic. It is widely acknowledged that the two-term approximation is inadequate at high electron energies and for high values of the reduced electric field E/n [109]. Still, it could also occur for low-energy electrons in nitrogen.

Generally, gases with large inelastic cross-sections can induce highly anisotropic velocity distribution functions at low electron energies. Molecular nitrogen is an example of such a gas, with large vibrational excitation cross-sections compared to elastic cross-sections. For this reason, molecular nitrogen was the focus of several early multi-term BE studies [110, 111]. It was revealed that the electron mobility and diffusion coefficients predicted by the two-term BE models could have an error up to tens of percent. Similarly,

the two-term BE models could underpredict the excitation rates of the lower electronic states by tens of percent [111]. The electron-neutral excitation cross-sections for nitrogen compiled from Biagi's Fortran code, MagBoltz, are used in a Monte-Carlo simulation and the multi-term BE code [105]. While the limitations associated with the two-term BE models are well-known, the cascading effects introduced by the two-term approximation on the results of other models are less explored [112, 113].

This study obtains reaction rates and electron transport parameters using "MultiBolt" [114], considering a four-term expansion to represent BE. For comparing model predictions with a truncated BE model, simulations are also performed for the reaction and transport data obtained with the "BOLSIG+" solver [115]. Both the BE models calculate the EEDF for different values of the reduced electric field (E/n) and generate the necessary reaction rate and transport parameters as lookup tables. These lookup tables are generated as a function of the mean electron energy to take into account the effects of non-Maxwellian EDF on the fluid model results.
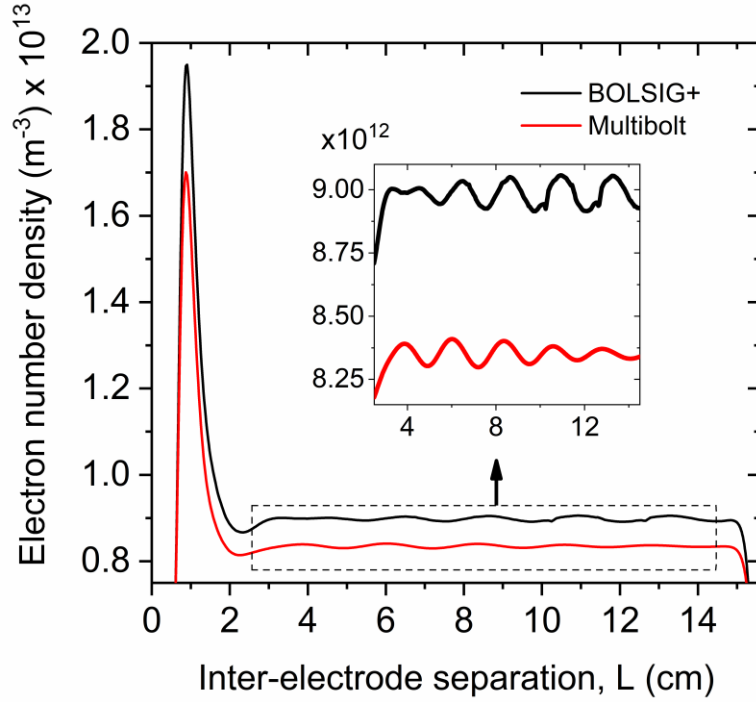
Figure 4.2 Comparison of electron number density predicted from a BOLSIG+ and MultiBolt as inset (P = 0.7 Torr, L = 15.5 cm, $V_d \sim 380$ V, $J_d \sim 0.018$ mA cm^{-2})

Figure 4.2 compares the predicted axial distribution of the electron number density (n_e), between the BOLSIG+ and MultiBolt data. For both the datasets, the simulations are performed as such that almost identical discharge voltage and current are attained. Despite the near-identical discharge voltage and current, it is evident that in the case of the two term-approximation, the higher intensity striations lie closer to the anode and vice versa in the case of the MultiBolt. Distinct differences between the predicted spatial profiles of the striations are present between the two data sets. The differences exist in the striation number and the amplitude of the undulations.
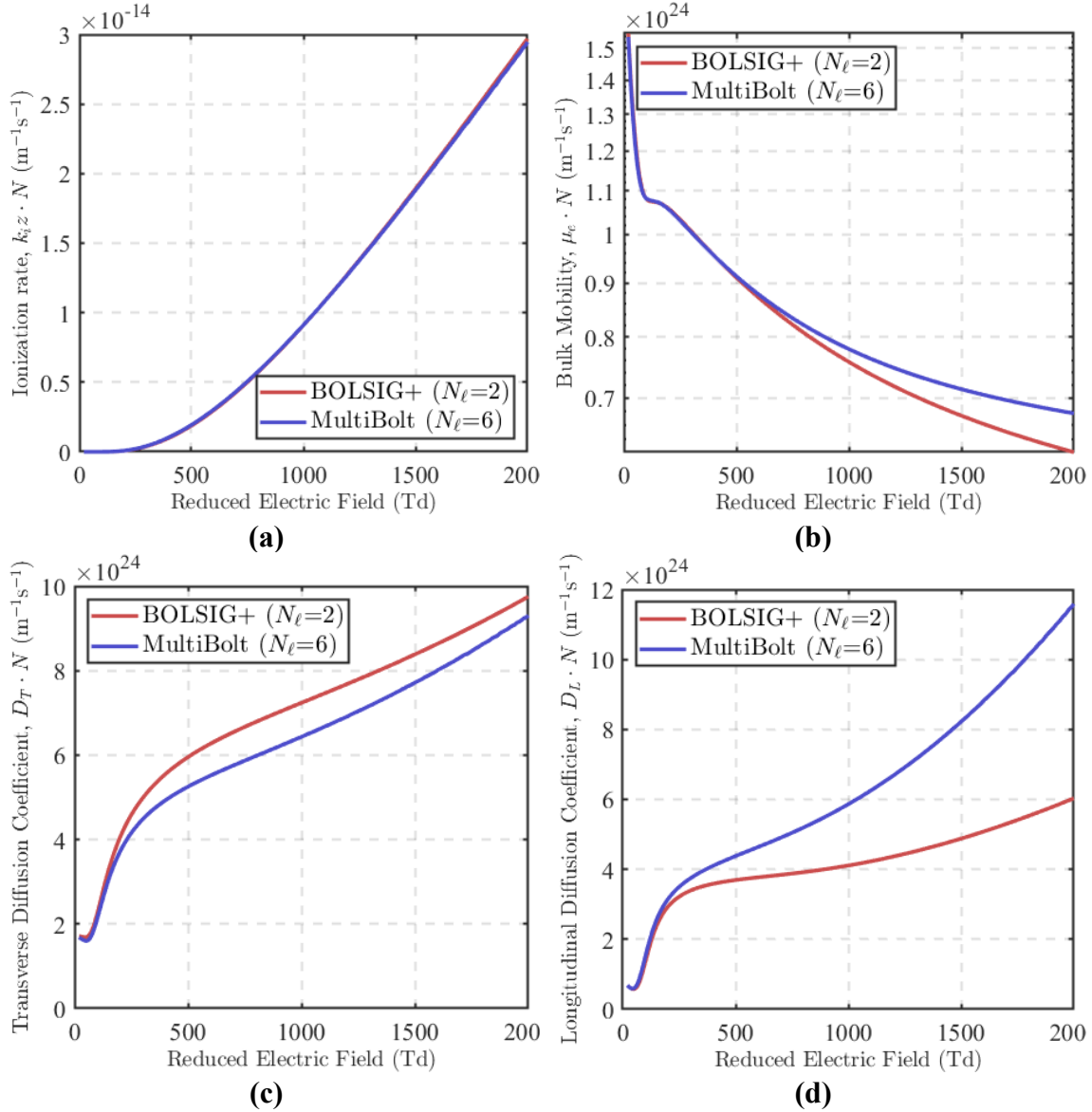
Figure 4.3 (a) Total ionization rate versus reduced electric field calculated from two-term and multi-term solutions to the BE in N_2, **(b)** Bulk electron mobility versus reduced electric field calculated from two-term and multi-term solutions to the BE in N_2, **(c)** Bulk transverse diffusion coefficient versus reduced electric field calculated from two-term and multi-term solutions to the BE in N_2, **(d)** Bulk longitudinal diffusion coefficient versus reduced electric field calculated from two-term and multi-term solutions to the BE in N_2
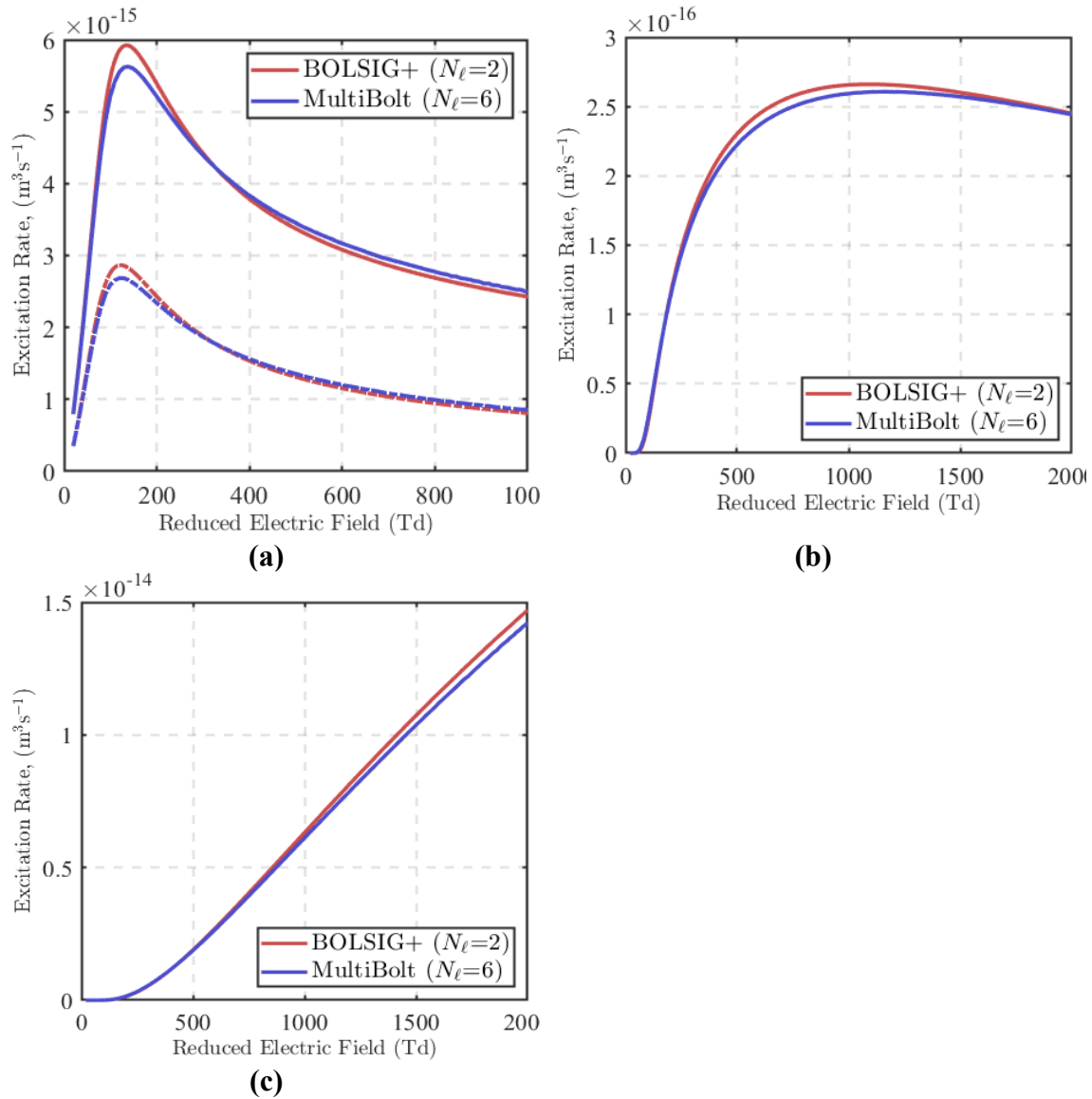
Figure 4.4 (a) Excitation rates of the first two vibrational levels on molecular nitrogen (threshold energies of 0.29 eV and 0.5742 eV, respectively), **(b)** Excitation rate of the first five vibrational levels of the $A^3\Sigma$ excited state (threshold energy of 6.73 eV), **(c)** Summed rate of excitation for all singlet states of N_2 (threshold energy of 14.2 eV)

Ionization rate and transport coefficients calculated from the two-term and multi-term BE equation are presented in Figure 4.3. As shown, the ionization rate as calculated via two-term and multi-term solutions to the BE are nearly identical. A similar agreement is observed for the electron mobility up to ~600 Td, beyond which the two-term and multi-

term results begin to deviate from each other. At 1000 Td, the differences in mobility are ~3% and increase to ~9% at 2000 Td. The diffusion coefficients demonstrate even higher sensitivity with ~ 14% variations in the transverse diffusion coefficient at 500 Td and a similar level at 2000 Td. Even more significant deviation is observed for the longitudinal diffusion coefficient, with ~18 % difference between the two models at 500 Td and up to ~ 90% at 2000 Td.

Figure 4.4 compares the excitation rates calculated from two-term and multi-term solutions. These excitation rates represent the general behavior observed with excitation to low energy (sub-eV), moderate energy (few eV), and high energy (10+ eV) excited states. The comparison of excitations to the lowest vibrational levels demonstrates a 5-10% disparity at ~120 Td. However, the models are in notably better agreement at higher reduced electric fields. Similar observations are made for moderate energy excitations. The models agree well below ~400 Td, deviate by ~2% in the range 500-1500 Td, then again at higher values of Td. Finally, the models agree well for the highest energy excitation, up to 1000 Td, where they begin to deviate from one another. At 2000 Td, the disagreement between the models is ~3.5%. Overall, unlike the transport parameters, the disparity between the calculated excitation rates is relatively small, indicating the EDF's strongest anisotropy for low-energy electrons.

These results re-emphasize the long-known shortcoming of the two-term approximation for molecular nitrogen [111]. Notably, the transport coefficients could be of error of about 5% in the range of 100 Td, which is the most relevant range of reduced electric field for this study. The electron diffusion coefficient strongly influences the structure of stratified plasma. Thus, one would expect that the differences between the two-

74

term and multi-term calculated coefficients would lead to cascading differences in predicted plasma structure when these coefficients are utilized in a fluid model.

Similar observations may be made for the excitation rates. Molecular nitrogen has a large number of vibrational excitations with large cross-sections. These are the dominant process for electron energy dissipation in the low energy range. And consequently, an error in calculating these excitation rates also implies an error in the overall energy balance of electrons in the plasma. The error in the excitation rates of the lowest vibrational levels of N_2 was on the order of 5-10% in the range of reduced electric field of relevance to this study (~100 Td). Thus again, one may expect that accurate excitation rates improve the accuracy of the fluid plasma model.

4.5 EXPERIMENTAL SETUP
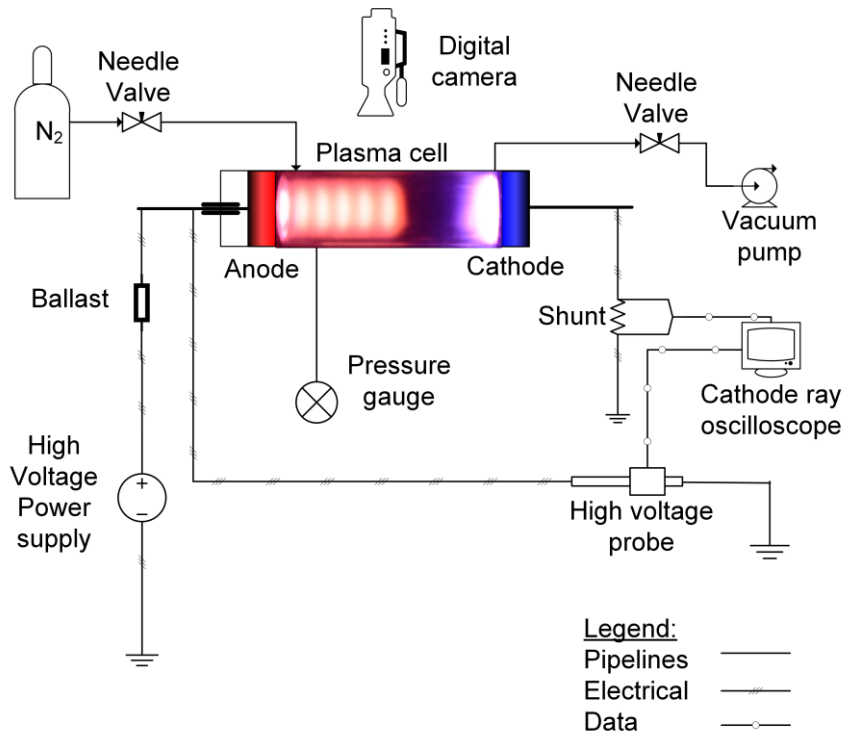
Figure 4.5 Schematic of the experimental setup

Experiments are conducted to determine the voltage-current characteristics and record the visual appearance of the striated structure. The prediction from the model is compared to these measurements. A schematic of the experimental setup is shown in Figure 4.5. A dc power supply (Glassman 0-20kV, 300W) is connected in series to a ballast resistor (100 kΩ), the low-pressure plasma cell, and a shunt resistor (10 kΩ) to measure the discharge current. A high voltage probe (North star PVM-4) and an oscilloscope probe (Tektronix M12) are used to measure the voltage drops across the discharge and the shunt respectively; both the probes are connected to a mixed-signal oscilloscope (Keysight MSO7054B). The discharge is enclosed in a cylindrical plasma cell consisting of a 16.0 cm (maximum operable length of 15.5 cm) long and 3.71 cm outer diameter cylindrical tube of borosilicate glass with two stainless steel disk electrodes on the opposite ends.

The electrodes have a diameter of 3.65 cm. The electrode arrangements are such that before conducting the experiments, the inter-electrode distance can be varied. The discharge cell is connected to the vacuuming system through ultra-torr conflate flanges. Additional fittings include a pressure gauge, a valve connecting the vacuum pump, and an inlet valve for supplying fresh high-purity nitrogen gas. The pressure is measured with a Teledyne Hastings 760s gauge. The vacuum is attained and maintained with an Agilent IDP-15 dry scroll vacuum pump. The outer periphery of each stainless-steel electrode is wrapped with polyamide tape (Kapton) on the sides to prevent the discharge from diffusing in between the glass tube and electrode gap at low pressures. A Nikon D7000 digital camera is used to image the discharge over a range of discharge current conditions. Each image was captured over an exposure time of 3 seconds with a NIKKOR 18-55mm f/3.5-5.6G lens with focal length, aperture, and ISO set to 32mm, f/4.5, and ISO-200 respectively.

4.6 RESULTS AND DISCUSSION

The simulations are conducted for 0.7 Torr operating pressure (P) with an inter-electrode separation distance (L) of 15.5 cm (i.e., $P*L$ = 10.85 Torr-cm) and electrode diameter of 1.1 cm. The discharge current/current density is varied to determine its effect on the striation structure. Figure 4.6 shows the spatial distribution of the electron number density (n_e), (Figure 4.6a), the electric potential, electric field, and the electron temperature (T_e) (Figure 4.6b) for the base case. These spatial distributions represent a quasi-steady-state solution that the system reaches in 0.25 ms.

(a)   **(b)**
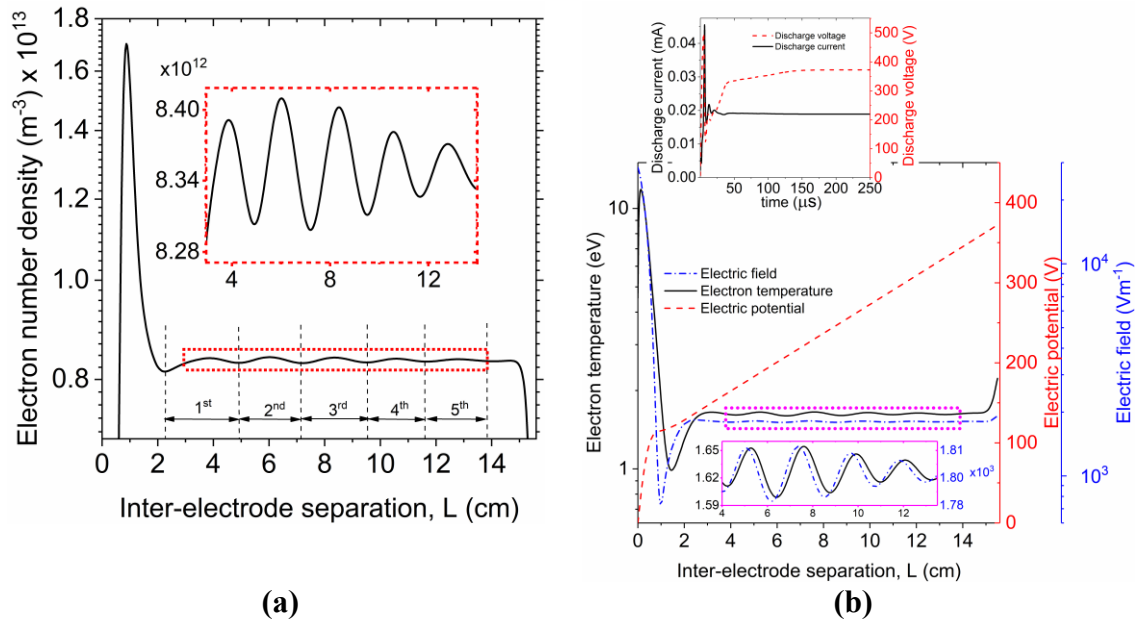
Figure 4.6 Quasi-steady spatial distribution of **(a)** Electron number density, **(b)** Electric potential, electric field and electron temperature along the axial distance (V_d =370 V, J_d = 0.018 mA cm^{-2})

At this stage, no noticeable transient variation in discharge current (I_d) and discharge voltage (V_d) is observed, as seen in Figure 4.6b inset. The n_e distribution shows a steady undulated profile representing a striated structure. The undulations occur outside

the cathode sheath, in the positive column region where the potential increases linearly (see Figure 4.6b). Five strata are formed between ~ 2.2 – 13.8 cm, with the electron density modulations between ~ 8.28 - 8.44 × 10^{12} m^{-3}.

The modulation of the electron number density and striation length decrease towards the anode. The first two striations have maximums n_e of 8.39 ×10^{12} m^{-3} and 8.41 × 10^{12} m^{-3} and a width of ~1.3 cm, based on the full-width half maximum (FWHM). Further, towards the anode, the density modulation decreases to 8.4 × 10^{12} m^{-3}, 8.38 × 10^{12} m^{-3} and 8.37 × 10^{12} m^{-3} and the width decreases to ~1.23 cm, 1.22 cm, and 1.20 cm, respectively. Similar experimental observations have been reported by Lisovskiy et al. [116], in which the width of the striations decreases progressively towards the anode. The n_e peaks coincide with the dip in T_e (Figure 4.6b) – the electron energy generally being depleted due to the ionization processes. Analysis shows that the net source of electrons and the ambipolar diffusion losses balance each other over striation length.

The profile of the electric potential clearly shows the cathode sheath and a positive column plasma with linearly increasing potential (Figure 4.6b). A closer look shows noticeable oscillations of the electric potential in plasma, with four fully developed modulations and one partially developed close to the anode; the amplitude of the modulations for the first two strata is ~ 30 Vm^{-1}. This amplitude subsequently decreases to ~ 18 and ~ 11 Vm^{-1} in the third and the fourth strata. The electron temperature T_e follows the electric field distribution and fluctuates between ~ 1.60 – 1.66 eV in the striated plasma.
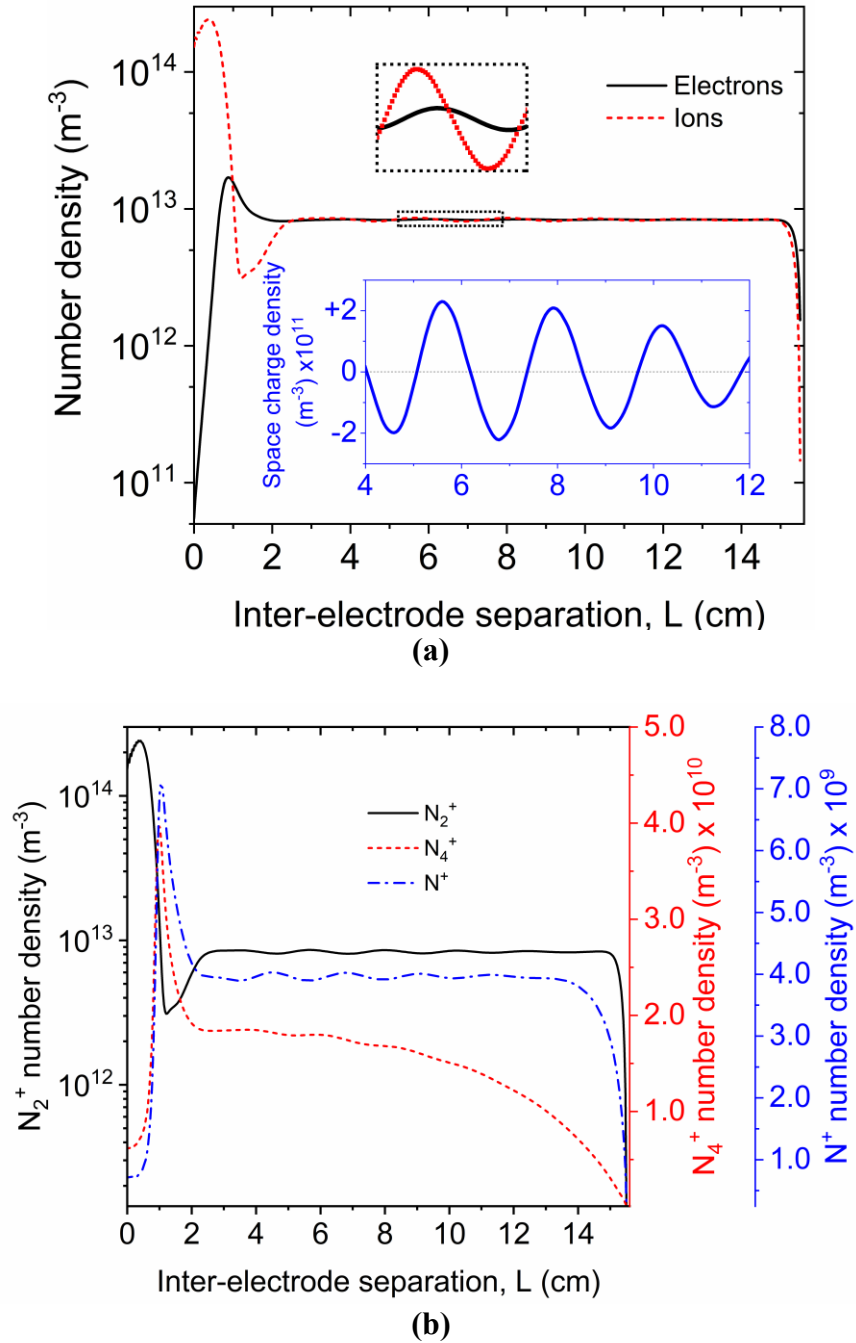
Figure 4.7 Quasi-steady spatial distribution of **(a)** Electron and total ions, **(b)** Three different ions. Zoomed view of the space charge density in the striated positive column region is provided as an inset. (V_d =370 V, J_d = 0.018 mA cm^{-2})

Figure 4.7 illustrates the spatial profiles of charged species. The electrons and total ions densities deviate in the cathode and anode sheaths but are almost the same in the

plasma region (insets Figure 4.7a). The presence of the small space charge in plasma is consistent with the oscillation in the electric field. The simulations identify N_2^+ as the dominant ion in the cathode sheath (Figure 4.7b) and the plasma region.

The spatial distributions of different ions in the striated plasma are distinctively different (Figure 4.7b). The density of the N_2^+ ion is significantly higher, and its oscillations are of higher amplitude compared to those of N^+ and N_4^+. In addition to the main channel of electron impact ionization, the N^+ and N_4^+ ions are formed by the charge exchange processes (R30: $N_2^+ + 2N_2 = N_2 + N_4^+$ and R31: $N_4^+ + N = 2N_2 + N^+$). These processes are not sensitive to the electric field strength. However, since N_2 and N_2^+ are more abundant in the system than N^{4+} and N, the N^{4+} density is higher than N^+.
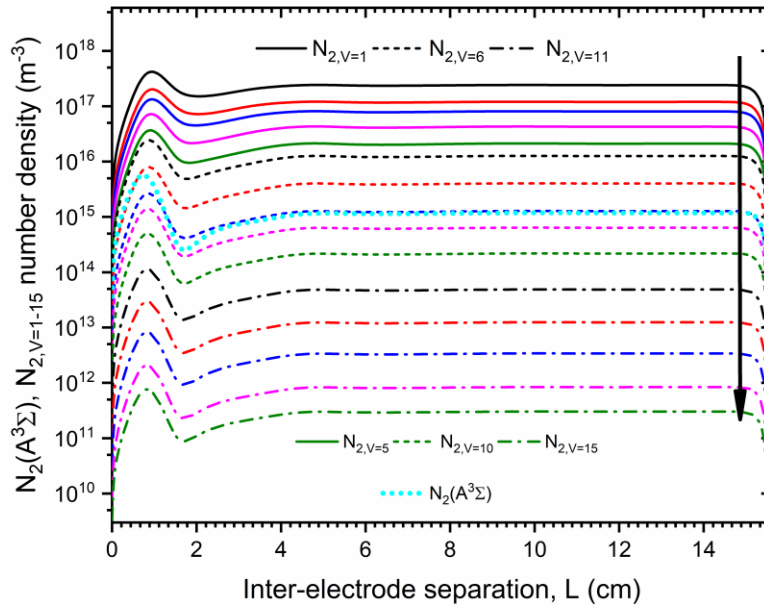
Figure 4.8 Spatial distribution of the different excited species across the axial distance ($V_d = 370$ V, $J_d = 0.018$ mA cm^{-2})

Figure 4.8 depicts the spatial distributions of the vibrationally excited and the electronically excited $N_2(A^3\Sigma)$ species. Even though the spatial profiles of the vibrational

excitation reaction rates (R2-R17) follow the n_e profile in the positive column (not shown here), smaller oscillations are observed for each of the vibrationally excited molecules. The reason is that, in addition to electron impact excitation, the vibrationally excited species are formed from the vibrational-relaxation (R49-R63) and the vibrational-vibrational (R65-R73) interactions, which do not depend on either T_e or n_e. The vibrationally excited species with lower excitation thresholds have the highest density. The $N_2(A^3\Sigma)$ distribution exhibits a similar profile as that of the vibrationally excited states. The predictions further show that despite requiring a higher threshold excitation energy (i.e., ~ 6.73 eV), the $N_2(A^3\Sigma)$ density is higher than the $N_{2,v=8}$ state, which has much lower excitation energy (~ 2.21 eV). The electronically excited $N_2(A^3\Sigma)$ state is not solely formed through direct electron impact, but also through a stepwise process involving $N_{2,v=1}$ (R19: $e + N_{2,v=1} = e + N_2(A^3\Sigma)$), which is present in higher abundance than other vibrational species owing to its lowest excitation potential. Outside of the cathode fall, where the electron kinetic energy is higher, the low-energy chemical processes dominate.

Figure 4.9 - Figure 4.11 illustrate the axial distribution of the reaction rates for N_2^+, N^+, and N_4^+ respectively. In these figures, the electron/ion sources are shown by solid lines, and the sinks are shown by dashed lines. The electron impact ionization reactions of N_2, $N_{2,v=1}$, and N (i.e., R23, R24, and R25), which have the highest ionization potential, are the most effective in the cathode sheath region (Figure 4.9), where the electron kinetic energy is higher. Even outside the cathode fall, N_2^+ is predominately formed by the electron impact, R23: $e + N_2 \rightarrow 2e + N_2^+$ (Figure 4.9b).
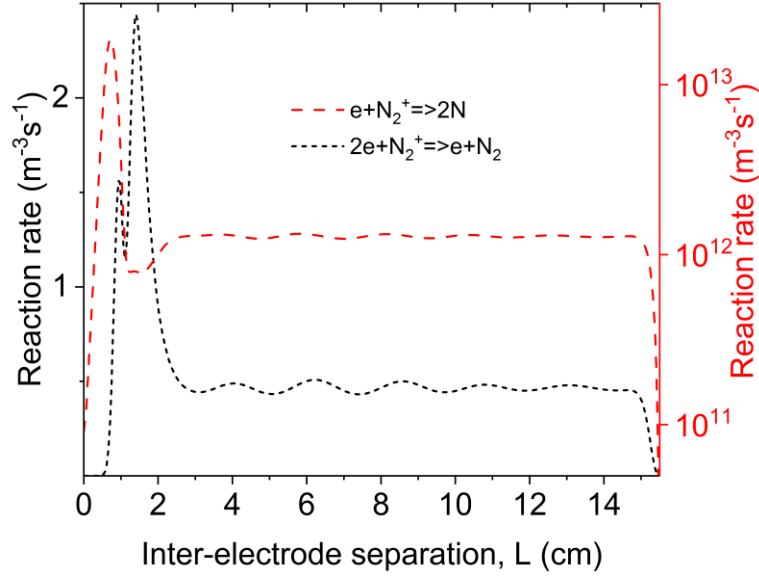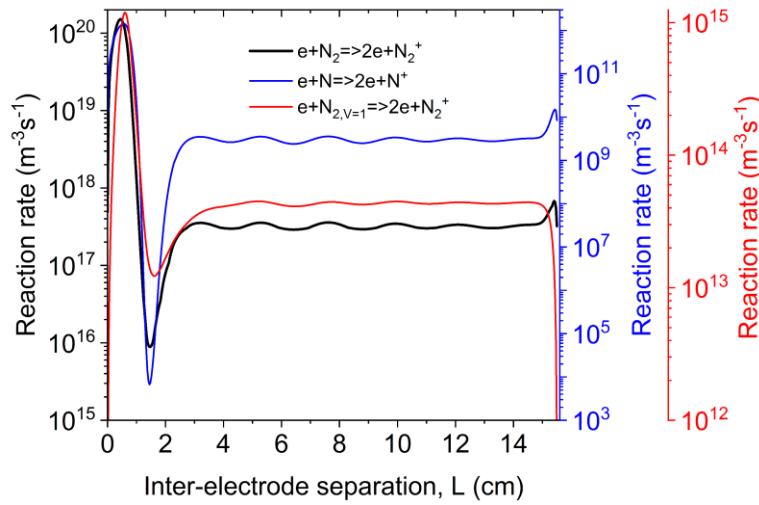
Figure 4.9 Spatial distribution of **(a)** Recombination **(b)** Ionization reaction rates of N_2^+ ions along the axial distance (V_d =370 V, J_d = 0.018 mA cm^{-2})

All three of these reaction rates are modulated in the striated plasma but have much lower rates than in the sheaths. The ionization from $N_{2,v=1}$ (R24) in the striated plasma is three orders of magnitude lower than R23 despite a slightly lower energy threshold. Even though $N_{2,v=1}$ requires lower energy than ground state N_2, the number density of ground state N_2 is significantly higher. Thus, the collision frequency of high-energy electrons with

the ground state N_2 will always be higher than that with $N_{2,v=1}$. For most of the stratified plasma, the dissociative recombination (R29: $e + N_2^+ \rightarrow 2N$) acts as a major consumption path and exceeds both the three-body recombination rates (R26: $2e + N_2^+ \rightarrow e + N_2$ and R27: $2e + N^+ \rightarrow e + N$). The model considered here incorporates the stepwise ionization of only $N_{2,v=1}$, the first vibrationally excited species of N_2. Data on stepwise ionization rate coefficients and/or collision cross-sections are very scarce in the literature. Cacciatore et al. contained the reaction cross-section data for step-ionization of $N_{2,v=5}$, and $N_{2,v=10}$ species but only for a limited electron energy range that could not be reasonably extrapolated for the present study [117]. Due to the limited availability of cross-section and reaction rate coefficients for the required electron energy range and different excited states, stepwise ionizations from all the other vibrational states were not included in the present study.
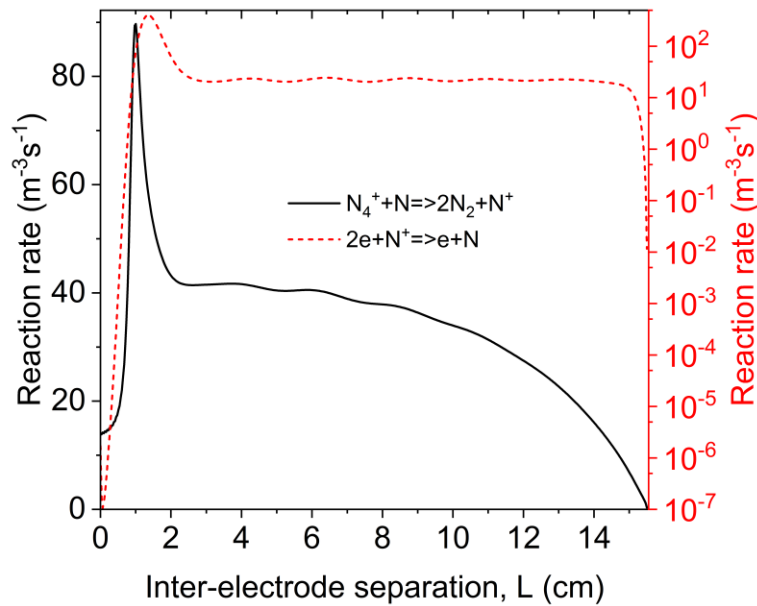
Figure 4.10 Distribution of the ionization and recombination reaction rates of N^+ ions across the axial distance ($V_d = 370$ V, $J_d = 0.018$ mA cm^{-2})

The formation of N^+ from heavy particle interaction is compared with the three-body recombination and presented in Figure 4.10. The N^+ formation in plasma occurs through the charge transfer (R31: $N_4^+ + N \rightarrow 2N_2 + N^+$). The rate of this reaction is larger than that of the three-body recombination rate of N^+ (R27: $2e + N^+ \rightarrow e + N$) for most of the positive column and follows the profile of N_4^+. The N_4^+ ions are formed predominantly by reaction between N_2 and N_2^+ (R30: $N_2^+ + 2N_2 \rightarrow N_2 + N_4^+$, see Figure 4.11); the electron impact dissociative recombination reaction (R28: $e + N_4^+ \rightarrow 2N + N_2$) remains as the most active consumption channel. Further comparison among Figure 4.9 - Figure **4.11** shows that for both N_2^+ and N^+, the recombination rates exceed the formation rates in the plasma, which has been identified by Kawamura et al. [69] as a source of instability and plasma stratification. However, for N_4^+ ions, which are formed through the charge transfer, the formation rate (R30) exceeds the recombination rates (R28 and R31).
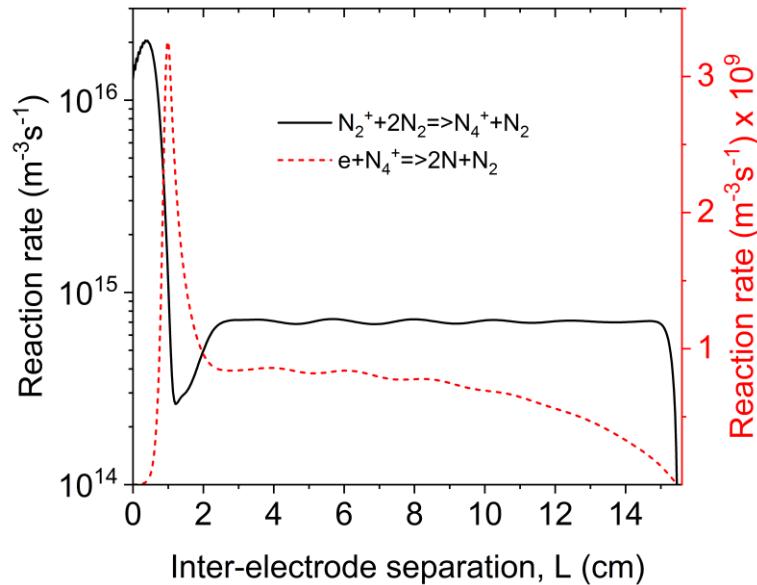
Figure 4.11 Distribution of the ionization and recombination reaction rates of N_4^+ ions across the axial distance ($V_d = 370$ V, $J_d = 0.018$ mA cm^{-2}

Numerical simulations were conducted by eliminating the vibrational excitation reactions ($N_{2,v=1-15}$) and compared with the base case results (Figure 4.12). The same discharge voltage and current were maintained for the two cases. It was observed that without vibrational excitation reactions, the striations did not form. Omitting only the $N_2(A^3\Sigma)$ excitation, N-elastic, and N-ionization reactions from the reaction scheme did not have any noticeable effect on the striations (not shown here). Previous studies [84, 88] have demonstrated that excluding the loss term due to ambipolar diffusion to the wall fails to produce the positive column. In our case, both the ambipolar diffusion to the wall and the vibrational excitation reactions play key roles in forming the standing striation in molecular nitrogen gas. An interesting observation in the profile of T_e (Figure 4.12) is that without the vibrational excitation reactions, T_e remains around 1.63 eV in the positive column. This value of ~ 1.63 eV is also the mean value of the electron temperature T_e in the presence of striations with the vibrational reactions included in the model. One would expect that the value of T_e would increase in the absence of the vibrational excitations channel, however, that is not the case. As always happens in non-equilibrium plasmas, the electron temperature is adjusted to satisfy the balance of the production and losses, which depend on the overall chemistry mechanism.
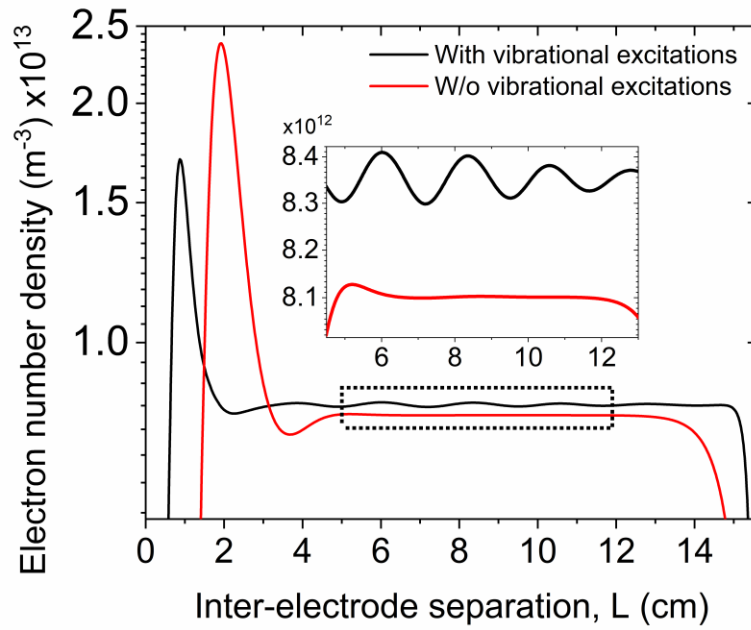
(a)
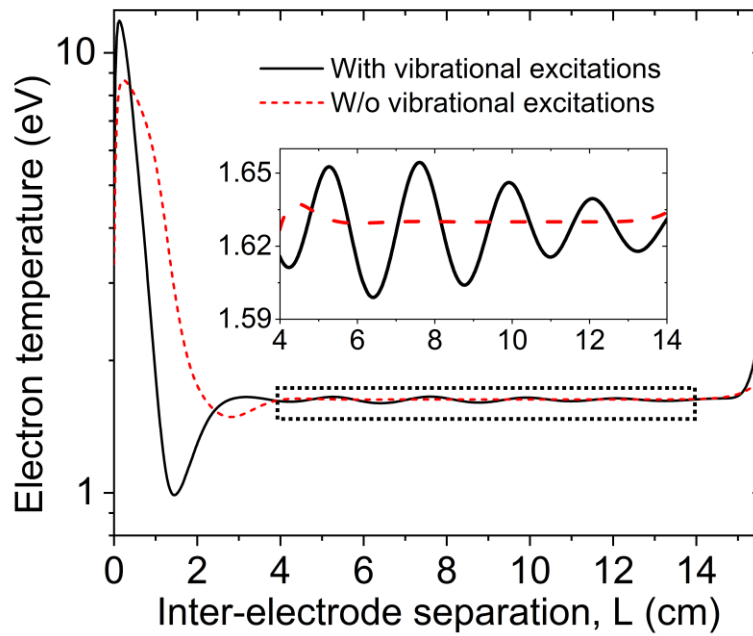
(b)

Figure 4.12 Impact of vibrational excitation reactions ($e + N_2 \rightarrow e + N_{2, v=1\text{-}15}$) on **(a)** Electron number density, **(b)** Electron temperature distribution along the axial distance
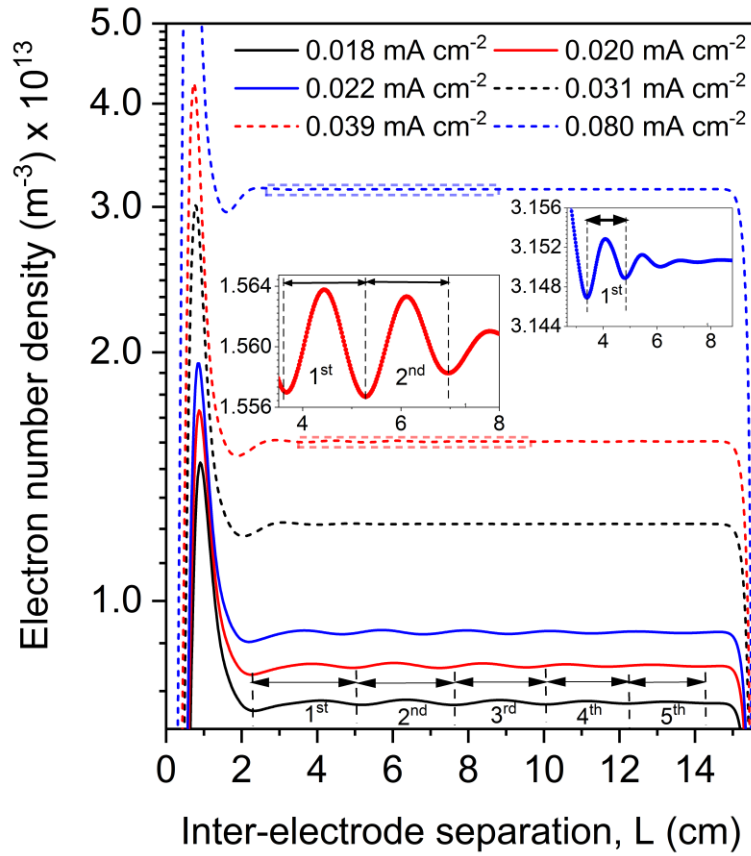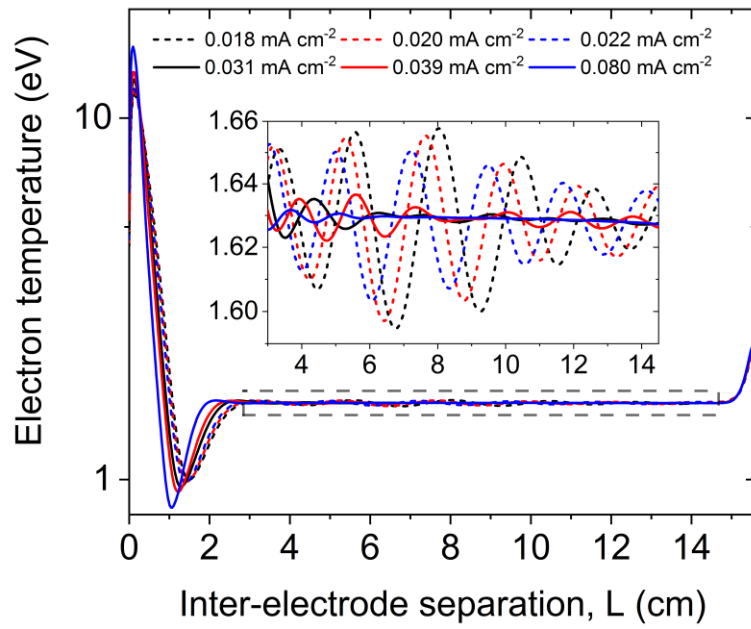
Figure 4.13 Predicted spatial distribution of **(a)** Electron number density, **(b)** Electron temperature distribution for different discharge current densities

The spatial distribution of n_e for a range of discharge current density is presented in Figure 4.13a. The discharge operates in the "*abnormal*" glow mode**.** As a result, the current density increases with the discharge voltage. The predictions clearly show that as the current density increases, the number of striations decreases. The striations tend to get shorter, as observed in the experiments (Fig. 17a). At higher current densities beyond 0.080 mAcm^{-2}, the striations completely phase out and the positive column becomes uniform throughout (not shown here). As the discharge current increases, the amplitude of the T_e modulation decreases, and the T_e value tends to approach ~ 1.63 eV (Figure 4.13b).

Figure 4.14 compares the total formation and consumption rates for the ions and electrons mapped across the entire electron temperature range of discharges at two current densities. These rates were obtained by the summation of all the independent sources and sinks for the respective charged species, including the radial losses from ambipolar diffusion. In both cases, even though some of the ions are formed through heavy particle reactions, the reaction rates of such processes are lower compared to that of electron-induced reactions; thus, the electron and ion formation rates are almost identical to each other, and the respective profiles overlap. In Figure 4.14a, unlike the continuous increasing ion consumption rate, the electron consumption rate increases only up to ~ 3.3 eV and then tends to decrease rapidly. The electron and ions formation and consumption rates start to become comparable to each other between ~ 1.3 - 2 eV, especially at T_e ~ 1.63 eV they become almost equal to each other.
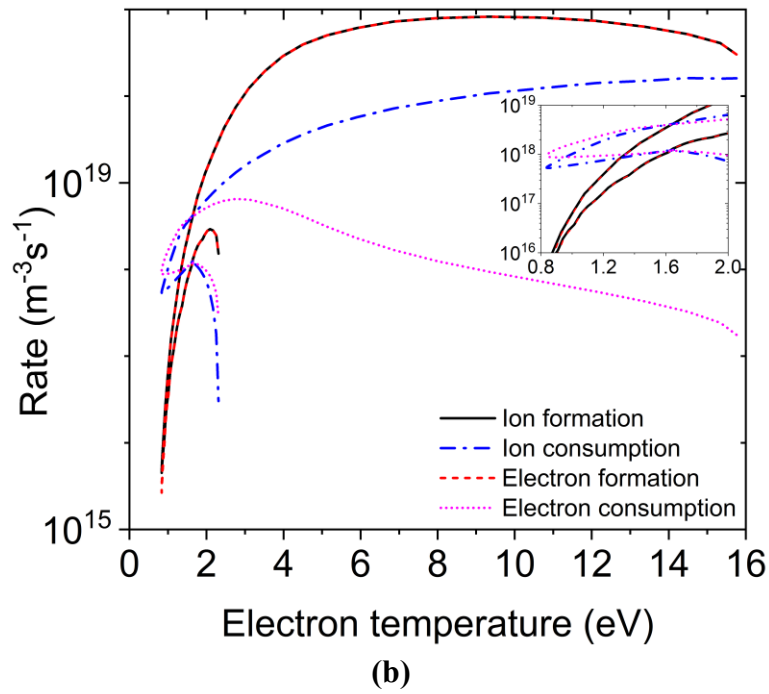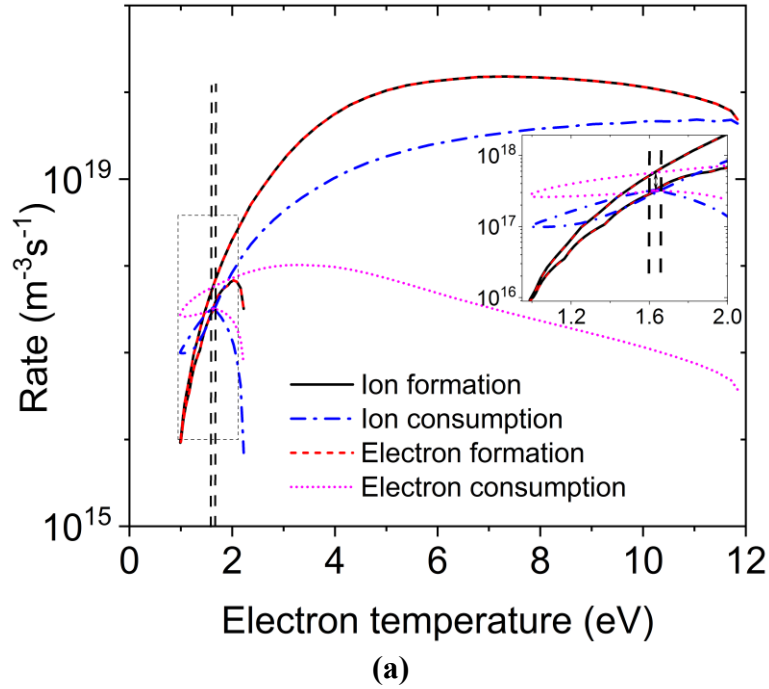
Figure 4.14 Ion and electron formation and consumption rate as a function of electron temperature during standing striations for operating discharge parameters of **(a)** V_d =370 V, J_d = 0.018 mA cm^{-2} , **(b)** V_d =388 V, J_d = 0.081 mA cm^{-2}

A closer look (Figure 4.14a inset) at the rates shows a distinct hysteresis between the ion and electron consumption rates at $T_e \sim 1.60 - 1.66$ eV, which is the T_e modulation amplitude in the striations. Figure 4.14b shows that there is a greater degree of overlap between the ion and electron consumption rates for higher current density, and the hysteresis behavior is nearly absent. A comparison of the consumption rates for ions and electrons suggests that significant differences between the ion and electron consumption rates and possible hysteresis characteristics of the consumption rates at the lower range of electron temperature (1.0 – 2.0 eV) can trigger instability in the system that can result in plasma stratification.

The impact of the vibrational excitation reactions on the electron heating ($\vec{J_e}.\vec{E} - \Delta e_{loss\,from\,vibration\,excitation}$) is shown in Figure 4.15a, where the joule heating and electron number density for two modulations (x = 7.4 – 11.4 cm) for two current densities are presented. It is evident that the joule heating profile is entirely out of phase with n_e. At lower current density, both the n_e and the power source oscillate with higher amplitude. At 0.022 mA cm^{-2}, the power oscillates between ~ 4 – 9 Wm^{-3}, and the reduced electric field oscillates between 78 – 82 Td. Most of the power absorbed by electrons is lost to vibrational and electronic excitation [118]. As the current density increases, the modulation amplitude of the energy source diminishes to 0.2 Wm^{-3}, which is equivalent to a reduction in the oscillating amplitude by ~96%. This implies that the vibrational excitation reactions do not perturb the Joule heating term significantly at higher current and voltage. The distributions of the vibrationally excited species for three current densities are presented in Figure 4.15b. The vibrational species distribution tends to conform towards a Maxwellian-like profile at higher currents.
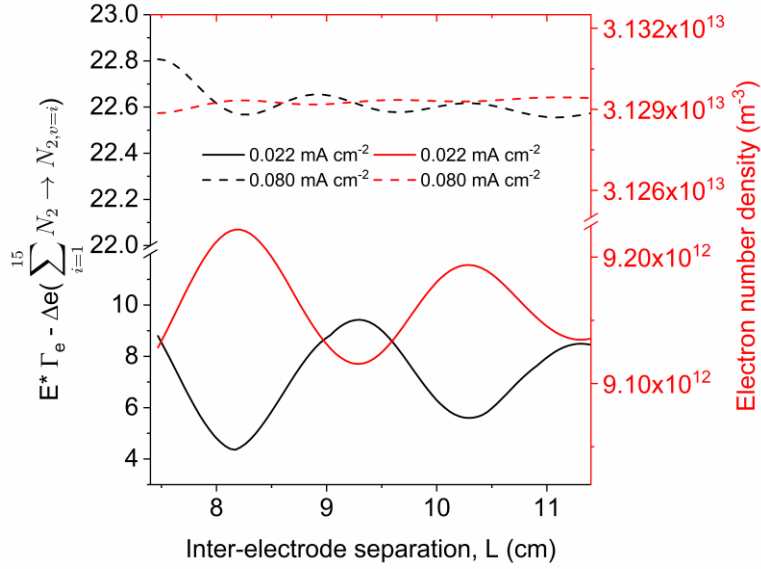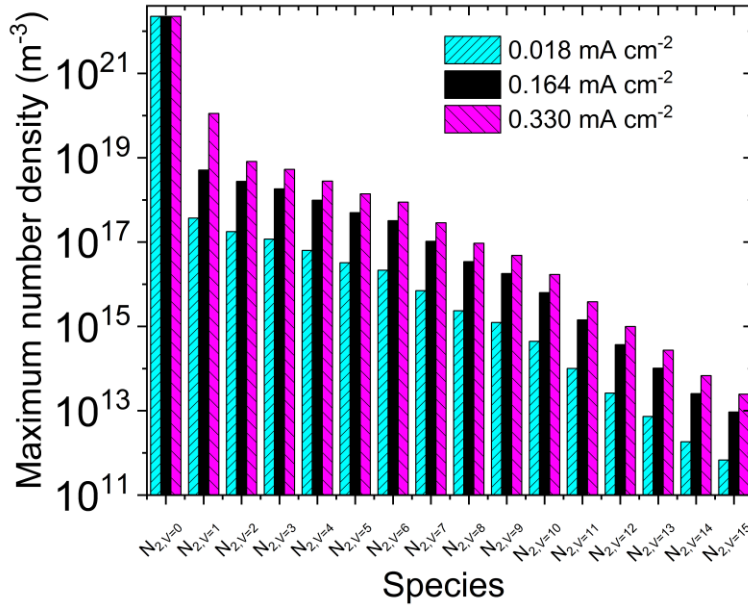
Figure 4.15 (a) Spatial variation of $\vec{j}_e . \vec{E} - \Delta e_{loss\ from\ vibration\ excitation}$ and electron number density in the striated region, **(b)** Distribution of vibrationally excited species for different current densities

Figure 4.16 shows the spatial distributions of the electric field, electron temperature, n_e, n_{ion}, $\frac{dn_e}{dt}$ and $\frac{dn_{ion}}{dt}$, and the phase differences between these in the striated

region. The electric field leads the electron temperature by ~ 0.211π. The phase shift

between T_e and n_{ion} is ~ 0.206π with n_{ion} lagging T_e (Figure 4.16a). However, the electron

temperature lags $\frac{dn_{ion}}{dt}$ by ~ 0.083π. On the other hand, both n_e and $\frac{dn_e}{dt}$ lag T_e by ~ 0.656π

and 0.156π, respectively (Figure 4.16b).

(a)

(b)
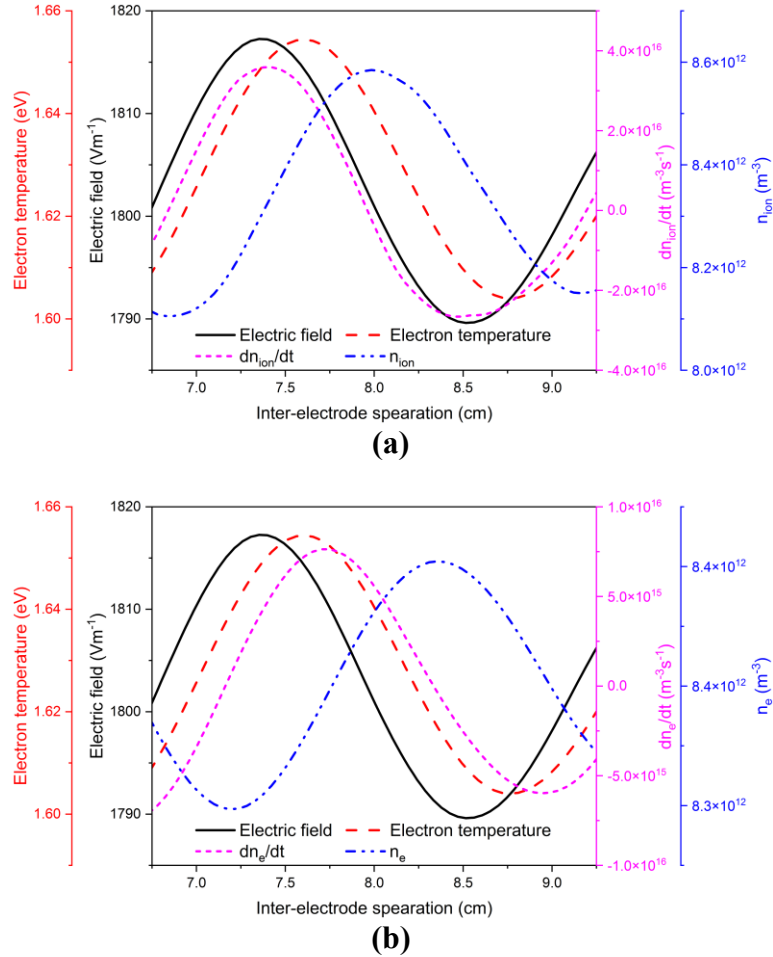
Figure 4.16 Spatial evolution of **(a)** n_{ion}, $\frac{dn_i}{dt}$, electric field, electron temperature and
(b) n_e, $\frac{dn_e}{dt}$, electric field, electron temperature (V_d =370 V, J_d = 0.018 mA cm^{-2})

The maxima of electron energy perturbation is shifted towards the cathode when

compared to both n_e and n_{ion}. The maximum electron energy contributes to the highest

ionization rate, and the newly produced electrons tend to move the maximum electron

number density towards the anode. However, the electron energy transport along the density gradient (i.e., the Dufour effect) tends to shift the peak of the electron energy towards the cathode. Hence, the ionization and the Dufour effect act against each other, and a balance between these two effects results in standing striations.

The variation of the density-gradient-dependent diffusivity, $\chi_\varepsilon = D_\varepsilon - \left(\frac{\mu_\varepsilon}{\mu_e}\right)D_e$ [79] is shown in **Fig. 17** as a function of electron temperature. The distribution indicates that χ_ε is predominantly negative except for a narrow range at low T_e ($\sim 1.5 - 2.25$ eV) and at high T_e (i.e., $T_e > 22.5$ eV). Desangles et al. [79] showed that a sufficiently large negative value of χ_ε can generate instability in the system, which is consistent with our predictions. However, the narrow T_e range of $\sim 1.5 - 2.25$ eV across which χ_ε changes sign, coincides with the T_e modulation range that we have obtained in the striated positive column.
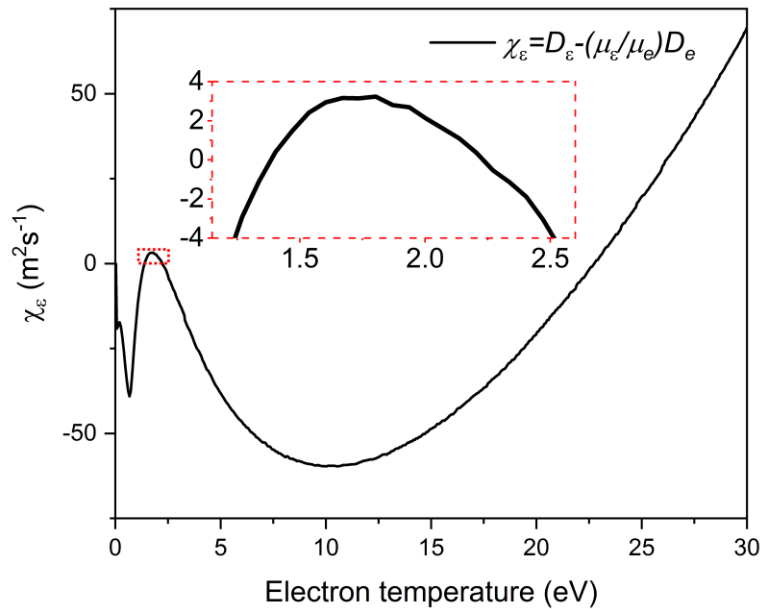
Figure 4.17 Variation of density gradient dependent diffusivity χ_ε (Dufour effect) as a function of electron temperature

The experiments are conducted at $P = 0.7$ Torr and an inter-electrode separation of $L = 15.5$ cm. Voltage-current characteristics were measured together with visual observation of the discharge (Figure 4.18). The discharge visualization shows that as the current increases, the number of striations tends to decrease but the striation thickness increases. Furthermore, the cathode region (Faraday dark space) expands, and the positive column with striations is shifted towards the anode (Figure 4.18a). Figure 4.18b shows the comparison of variation in striation lengths from the cathode to the anode for both the predicted and the experimental case. The condition is chosen such that at least five standing striations are visible in both cases, which corresponded to the lowest current density conditions for each case. It is seen that in both cases, the striation lengths decrease from the cathode to the anode, showing qualitative agreement.

The spatial profiles of n_e from our simulations (Figure 4.13a) qualitatively capture the dependence of the striation number on the discharge current. The peak n_e increases as a function of discharge current and can be related to the observed increase in emission intensity of the cathode glow in the experiments. The full width half maximum (FHWM) of the predicted n_e in the negative glow increases with the discharge current, however, the length of the Faraday dark space is much shorter compared to the visual observations. Even though the model can reproduce qualitative trends of the striation behavior (i.e., number of striations), the most considerable discrepancies with the experimental observations are for the Faraday dark space. The predicted striation width decreases with increasing the current density. Additionally, as the discharge current density increases, the predicted strata tend to constrict axially towards the cathode rather than towards the anode location. In our simulations, the width of the cathode region does not change significantly

with increasing the discharge current. The cathode-directed constriction of the strata could be a result of that. The experimentally observed increase of the Faraday dark space is due to nonlocal ionization by the fast electrons from the cathode sheath [119], which is currently not captured by the model.
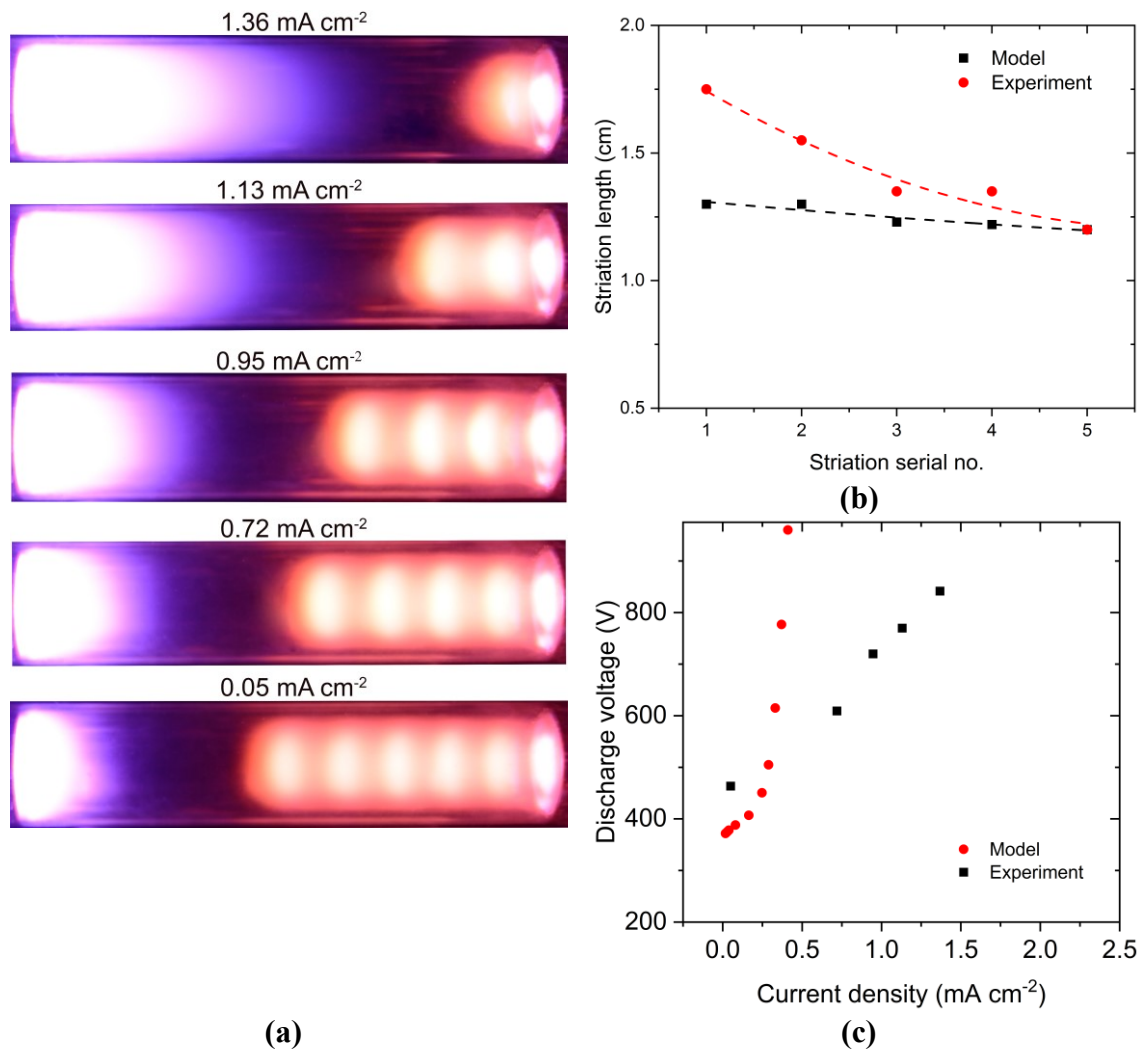
Figure 4.18 (a) Images of the plasma structures for different discharge densities, **(b)** Comparison of measured and predicted striation lengths, **(c)** Comparison of measured and predicted voltage-current characteristics

The measured and predicted voltage-current (Figure 4.18c) characteristics clearly show the discharge operating in the "*abnormal*" glow mode. However, a substantial

discrepancy exists between the absolute values obtained in simulations and the experiments. These discrepancies are attributed to the deficiencies of the fluid model, which cannot capture nonlocal effects in the cathode region. The experimental observations of plasma emission in both the cathode region and striated positive column show radial gradients, which a one-dimensional model cannot accurately capture. A two-dimensional model is currently under development.
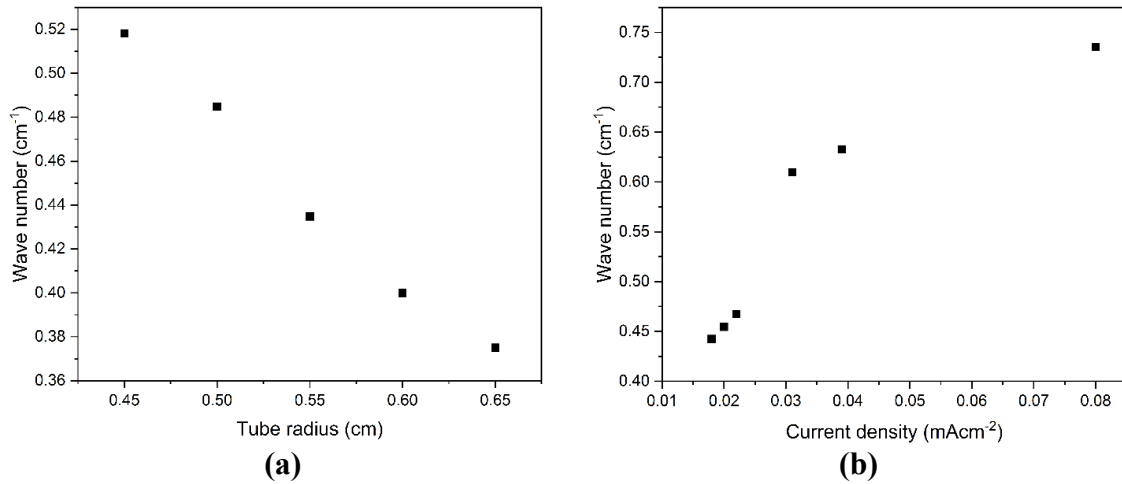
Figure 4.19 Wave number as a function of **(a)** Discharge tube radius, **(b)** Discharge current density

Simulations were conducted to assess the influence of discharge tube diameter and discharge current on the striation characteristics. In these simulations, the tube diameter and discharge current were varied independently. Figure 4.19 summarizes the dependence of the striation wave number on the discharge tube radius and discharge current. Figure 4.19a shows that the wave number decreases almost linearly with increasing the tube radius. As the tube radius decreases, the radial losses of the charged species increase, thereby increasing the region of stratification. A non-linear dependence is observed with respect to the current density (Figure 4.19b). The wave number increases sharply till ~ 0.30

mAcm^{-2} and tends to saturate with further increase of the current density. Notably, even though the wave number increases, the number of striations decreases in the positive column, as has been previously shown in Figure 4.13a.
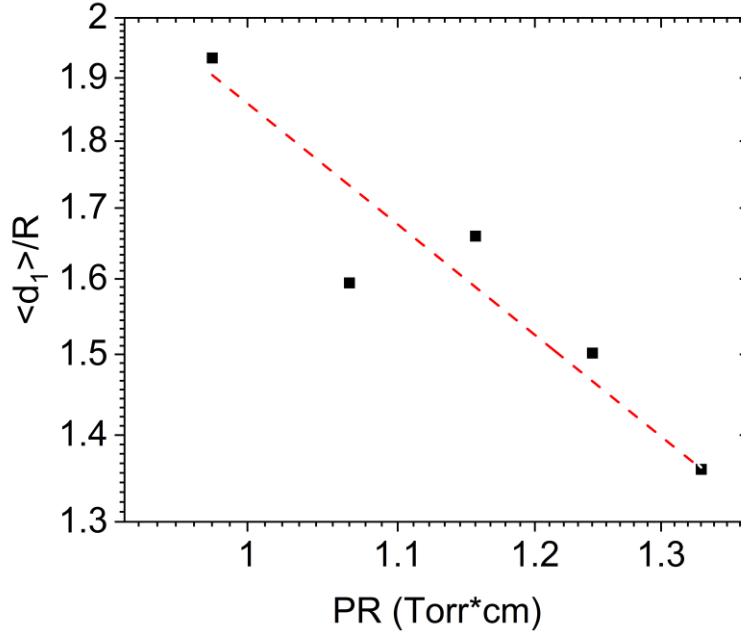
Figure 4.20 The ratio of the thickness of the first striation to tube radius against the product of gas pressure and tube radius

The ratio of the width of the first striation ($\langle d_1 \rangle$) to the discharge tube radius (R) is plotted against the product of the pressure and the tube radius (PR) and presented in Fig. 20. The figure shows ($\langle d_1 \rangle/R$) to have a strong negative correlation to (PR) and thus follows the famous Goldstein-Wehner law, $\frac{\langle d_1 \rangle}{R} = \frac{C}{(PR)^m}$. From a regression fit, the values of C and m are found to be C_{model}=1.86 and m_{model}=1.085 and compare favorably to the ones obtained from experiments, C_{expt}=1.05 and m_{expt}=0.32 as reported in [120].

Following the work of Urbankova and Rohlena [80], we performed a linear stability analysis of the striation behavior in low-pressure dc nitrogen plasmas. From the linear analysis, the dispersion (ω_r) and the application (ω_i) have the following expressions:

$$\frac{\omega_r}{D_a} = \left[\left(\frac{2.4}{R_{tube}}\right)^2 \left(S_{ioniz|\varepsilon}-1\right) - \eta_e k^2\right]\frac{k\varepsilon}{E_x}\frac{\Upsilon_1}{\Upsilon_2} + \frac{\mu_{e|\varepsilon}E_x}{\varepsilon}k\frac{\Upsilon_3}{\Upsilon_2}$$

$$\frac{\omega_i}{D_a} = -k^2\frac{D_e}{\mu_e T_e} + \left[\eta_e k^2 - \left(S_{ioniz|\varepsilon}-1\right)\left(\frac{2.4}{R_{tube}}\right)^2\right]\frac{\Upsilon_3}{\Upsilon_1} + \mu_{e|\varepsilon}k^2\frac{\Upsilon_1}{\Upsilon_2}$$

$$\left.\begin{array}{l}\Upsilon_1 = k^2\frac{\varepsilon^2}{E_x^2}\left[\frac{D_e}{\mu_e T_e}\kappa_e + \chi_\varepsilon\left(\mu_\varepsilon + \mu_\varepsilon\mu_{\varepsilon|\varepsilon}-\eta_e\right)\right] + \frac{D_e}{\mu_e T_e}\left(\varepsilon_{loss|\varepsilon}+\mu_{e|\varepsilon}\right) + 2\left(\mu_\varepsilon+\mu_\varepsilon\mu_{\varepsilon|\varepsilon}-\eta_e\right) \\[12pt] \Upsilon_2 = k^4\frac{\varepsilon^4}{E_x^4}\kappa_e + k^2\frac{\varepsilon^2}{E_x^2}\left[2\kappa_e\left(\varepsilon_{loss|\varepsilon}+\mu_{e|\varepsilon}\right) + \left(\mu_\varepsilon+\mu_\varepsilon\mu_{\varepsilon|\varepsilon}-\eta_e\right)^2\right] + \left(\varepsilon_{loss|\varepsilon}+\mu_{e|\varepsilon}\right)^2 \\[12pt] \Upsilon_3 = k^4\frac{\varepsilon^4}{E_x^4}\kappa_e\chi_\varepsilon + k^2\frac{\varepsilon^2}{E_x^2}\left[\chi_\varepsilon\left(\varepsilon_{loss|\varepsilon}+\mu_{e|\varepsilon}\right) + 2\kappa_e - \frac{D_e}{\mu_e T_e}\left(\mu_\varepsilon+\mu_\varepsilon\mu_{\varepsilon|\varepsilon}-\eta_e\right)\right] + 2\left(\varepsilon_{loss|\varepsilon}+\mu_{e|\varepsilon}\right)\end{array}\right\}$$

(1)

where k is the wave number, E_x is the axial electric field, κ_e is the thermal conductivity of the electrons, η_e electron transport due to temperature gradient – Soret effect, χ_ε energy transport due to density gradient – Dufour effect, S_{ioniz} is the electron ionization source, ε_{loss} is the electron energy loss. $S_{ioniz|\varepsilon}$, $\varepsilon_{loss|\varepsilon}$, $\mu_{e|\varepsilon}$, $\mu_{\varepsilon|\varepsilon}$ are log-log derivatives, e.g. $S_{ioniz|\varepsilon} = \partial\,lnS_{ioniz,o}/\partial ln\varepsilon_o$, where subscripts 'o' denotes unperturbed conditions.
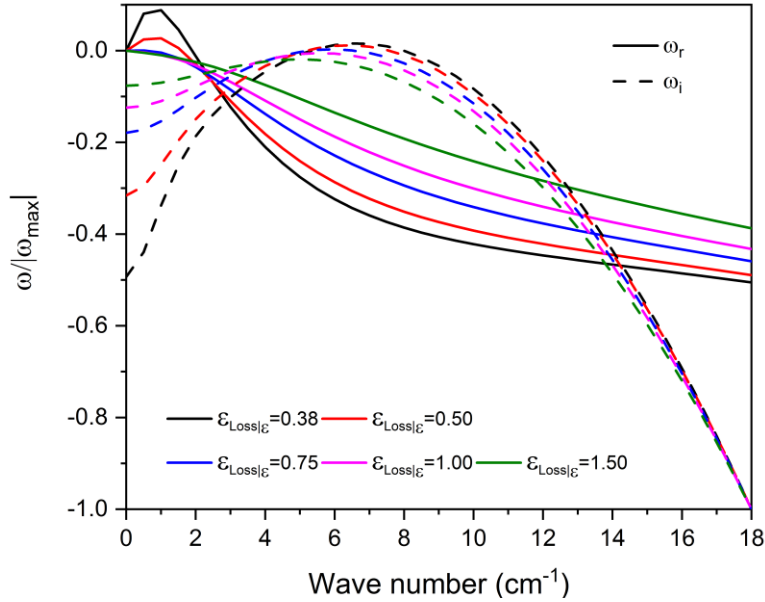
Figure 4.21 Calculated dispersion and amplification curves of wave instability in a low pressure nitrogen dc discharge for different values of $\varepsilon_{loss|\varepsilon}$ values. The positive column of the base case is utilized for the different parameter values in equation (1)

The calculated values of ω_r and ω_i are shown in Figure 4.21 as a function of wave number for different $\varepsilon_{loss|\varepsilon}$ values. It should be noted that $\varepsilon_{loss|\varepsilon}$= 0.38 corresponds to the electron energy loss considering all the reactions in Table 4.1. Both ω_r and ω_i have a strong dependence on $\varepsilon_{loss|\varepsilon}$ and can vary from positive to negative over the wave number range. For $\varepsilon_{loss|\varepsilon}$ = 0.38, the dispersion curve has positive values at small wave numbers and decreases in a nonlinear fashion towards negative values at ~ 3 cm^{-1}. As $\varepsilon_{loss|\varepsilon}$ increases, the dispersion curve remains negative for the rest of the wave numbers. The electron energy loss associated with the vibrational excitation process decreases the $\varepsilon_{loss|\varepsilon}$, the variation of the energy loss as a function of the mean energy. The different vibrational excitation spreads $\varepsilon_{loss|\varepsilon}$ progressively over the mean energy range. The energy loss associated with only dissociation and ionization results in a larger value of $\varepsilon_{loss|\varepsilon}$. The amplification curve

has a weaker dependence on $\varepsilon_{loss|\varepsilon}$ and mostly retains negative for the entire range of wave numbers. However, for $\varepsilon_{loss|\varepsilon} = 0.38$, a slight positivity is evident, indicating the possibility of wave amplification. The presence of vibrationally excited states relaxes the plasma dependency on direct electron impact ionization and allows stepwise ionization to play a role. The stepwise ionization process requires lower threshold energy and is less sensitive to the electron energy making $\varepsilon_{loss|\varepsilon}$ to decrease [80].

4.7 CONCLUSIONS

A one-dimensional fluid model has been developed to simulate striations in nitrogen dc discharges at moderate gas pressures. The plasma model included 22 species and 73 gas-phase reactions with multiple levels of vibrationally excited molecules. Simulations were conducted for a parallel plate geometry with the inter-electrode gap of 15.5 cm, the tube radius 0.55 cm, and pressure of 0.7 Torr, which correspond to $PR = 0.385$ Torr-cm. The simulations predicted standing striations with substantial oscillations of plasma density, electric field, electron temperature, vibrational temperature, and reaction rates. The modulation of the electron temperature occurred in the range of ~ 1.60 − 1.66 eV. We found that the Dufour diffusivity is positive only in the vicinity of this range of T_e, which establishes a stability criterion in this range. Electron and ions' production and consumption rates in the striated plasma varied nonlinearly with the electron temperature: the consumption rate surpassed the formation rate until ~ 1.63 eV. The predictions identify that ionization and Dufour diffusion balance each other resulting in standing waves. Therefore, our model predictions are consistent with the literature identifying Dufour-like diffusion as a critical instability source. Our study indicates that the vibrational excitation of molecules and the ambipolar diffusion processes are essential in predicting the striation

structures. The study showed that the striations cease to exist without the vibrational excitation of molecules in the model. A linear stability analysis further confirmed that the electron energy loss associated with the vibrational excitation process decreases the variation of the energy loss as a function of the mean energy. Both dispersion and amplification of the linear waves depend upon the electron energy loss term, which can trigger instability and plasma stratification for the considered operating conditions.

Parametric studies were conducted to determine the influence of discharge current on striation behavior. Operating in the "*abnormal*" regime, the number of strata decreased with increasing current. No striations formed at a sufficiently high current. Model predictions were compared with experimental measurements. The predicted voltage-current characteristics agreed qualitatively well with the measured data but showed considerable quantitative discrepancies. The model was also able to capture the qualitative trend in the current density dependence of striations. However, the most substantial differences existed with the observed length and location of the Faraday dark space. The calculated size of the Faraday dark space was much shorter compared to experimentally observed. These discrepancies are caused by the well-known deficiencies of the fluid model, which cannot capture well the non-local effects in the cathode region of the abnormal discharges. Including the non-local ionization by the fast electrons from the cathode sheath in future work will improve the agreement with the experiments. Furthermore, the model will be extended to resolve the radial dimension as well to better account for the radial transport of plasma species.

4.8 ACKNOWLEDGEMENT

4.9 REFERENCES

37.   Sakiyama, Y., D.B. Graves, H.-W. Chang, T. Shimizu, and G.E. Morfill, *Plasma chemistry model of surface microdischarge in humid air and dynamics of reactive neutral species.* Journal of Physics D: Applied Physics, 2012. **45**(42): p. 425201.

61.   Oleson, N.L. and A.W. Cooper, *Moving striations.* Advances in Electronics and Electron Physics, 1968. **24**: p. 155 - 278.

62.   Kolobov, V.I., *Striations in rare gas plasmas.* Journal of Physics D: Applied Physics, 2006. **39**(24): p. R487-R506.

63.   Golubovskii, Y.B., V. Nekuchaev, and A.Y. Skoblo, *Advances in the study of striations in inert gases.* Technical Physics, 2014. **59**(12): p. 1787-1800.

64.   Kolobov, V., *Glow Discharges: Stratification*, in *Encyclopedia of Plasma Technology*. 2016. p. 529-539.

65.   Liu, Y.X., E. Schungel, I. Korolov, Z. Donko, Y.N. Wang, and J. Schulze, *Experimental observation and computational analysis of striations in electrocnegative capacitively coupled radio-frequency plasmas.* Physical Review Letters, 2016. **116**: p. 255002.

66.   Gudmundsson, J.T. and A. Hecimovic, *Foundations of DC plasma sources.* Plasma Sources Science and Technology, 2017. **26**(12): p. 123001-1-20.

67.   Lisovskiy, V.A., V.A. Koval, E.P. Artushenko, and V.D. Yegorenkov, *Validating the Goldstein–Wehner law for the stratified positive column of dc discharge in an undergraduate laboratory.* European Journal of Physics, 2012. **33**(6): p. 1537-1545.

68.   Pollard, W., P. Suzuki, and D. Staack, *Striations in high-pressure hydrogen microplasma.* IEEE Transactions on Plasma Science, 2014. **42**(10): p. 2650-2651.

69.   Kawamura, E., M.A. Lieberman, and A.J. Lichtenberg, *Ionization instability induced striations in atmospheric pressure He/H2O RF and DC discharges.* Journal of Physics D: Applied Physics, 2017. **50**(14).

70.   Goldstein, R.A., M.A. Huerta, and J.C. Nearing, *Stationary striations in an argon plasma as a bifurcation phenomenon.* Physics of Fluids, 1979. **22**(2).

71.   Pekarek, L., *Ionization waves (striations) in a discharge plasma* Soviet Physics Uspekhi, 1968. **11**(2): p. 188.

72.   Allis, W.P., *Review of glow discharge instabilities.* Physica B+C, 1976. **82**(1): p. 43- 51.

73.   Nighan, W.L. and W.J. Wiegand, *Influence of negative-ion processes on steady-state properties and striations in molecular gas discharges.* Phyical Review A, 1974. **10**: p. 922-945.

74.   Haas, R.A., *Plasma Stability of Electric Discharges in Molecular Gases.* Physical Review A, 1973. **8**(2): p. 1017-1043.

75.   Arslanbekov, R.R. and V.I. Kolobov, *2-D Simulations of striations in direct current glow discharges in argon.* IEEE Transactions on Plasma Science 2005. **33**(2): p. 354-355.

76.   Golubovskii, Y.B., A.Y. Skoblo, C. Wilke, R.V. Kozakov, J. Behnke, and V.O. Nekutchaev, *Kinetic resonances and stratification of the positive column of a discharge.* Phys Rev E Stat Nonlin Soft Matter Phys, 2005. **72**(2 Pt 2): p. 026414.

77.   Golubovskii, Y.B., V.I. Kolobov, and V.O. Nekutchaev, *On electron bunching and stratification of glow discharges.* Physics of Plasmas, 2013. **20**: p. 101602.

78.   Arslanbekov, R.R. and V.I. Kolobov, *Advances in simulations of moving striations in DC discharges of noble gases.* Physics of Plasmas, 2019. **26**(10).

79.   Désangles, V., J.-L. Raimbault, A. Poyé, P. Chabert, and N. Plihon, *Pattern formation in low-pressure radio-frequency plasmas due to a transport instability.* Physical review letters, 2019. **123**(26): p. 265001.

80.   Urbankova, H. and K. Rohlena, *Electron thermal diffusion instability and standing striations in the plasma of a dc discharge in molecular gases.* Czechoslovak Journal of Physics B, 1980. **30**: p. 1227 - 1235.

81.   Mulders, H.C., W.J. Brok, and W.W. Stoffels, *Striations in a low-pressure RF-driven argon plasma.* IEEE transactions on plasma science, 2008. **36**(4): p. 1380-1381.

82.   Liu, Y.-X., E. Schüngel, I. Korolov, Z. Donkó, Y.-N. Wang, and J. Schulze, *Experimental observation and computational analysis of striations in electronegative capacitively coupled radio-frequency plasmas.* Physical review letters, 2016. **116**(25): p. 255002.

83.   Iza, F., S. Yang, H. Kim, and J.K. Lee, *The mechanism of striation formation in plasma display panels.* Journal of applied physics, 2005. **98**(4): p. 043302.

84.   Levko, D. and L.L. Raja, *Magnetized direct current microdischarge I. Effect of the gas pressure.* Journal of Applied Physics, 2017. **121**(9): p. 093302.

85.   Golubovskii, Y.B., V. Maiorov, I. Porokhova, and J. Behnke, *On the non-local electron kinetics in spatially periodic striation-like fields.* Journal of Physics D: Applied Physics, 1999. **32**(12): p. 1391.

86.   Tsendin, L., *Electron kinetics in non-uniform glow discharge plasmas.* Plasma Sources Science and Technology, 1995. **4**(2): p. 200.

87.   Golubovskii, Y., S. Valin, E. Pelyukhova, V. Nekuchaev, and F. Sigeneger, *Discharge stratification in noble gases as convergence of electron phase trajectories to attractors.* Physics of Plasmas, 2016. **23**(12): p. 123518.

88.   Levko, D., *Electron kinetics in standing and moving striations in argon gas.* Physics of Plasmas, 2021. **28**(1): p. 013506.

89.   Sigeneger, F., G. Sukhinin, and R. Winkler, *Kinetics of the electrons in striations of spherical glow discharges.* Plasma Chemistry and Plasma Processing, 2000. **20**(1): p. 87-110.

90.   Mahamud, R. and T.I. Farouk, *Ion kinetics and self pulsing in DC microplasma discharges at atmospheric and higher pressure.* Journal of Physics D: Applied Physics, 2016. **49**(14): p. 145202.

91.   Farouk, T., B. Farouk, D. Staack, A. Gutsol, and A. Fridman, *Simulation of dc atmospheric pressure argon micro glow-discharge.* Plasma Sources Science and Technology, 2006. **15**(2006): p. 676-688.

92.   Kolobov, V.I., R.R. Arslanbekov, D. Levko, and V.A. Godyak, *Plasma stratification in radio-frequency discharges in argon gas.* Journal of Physics D: Applied Physics, 2020. **53**(25): p. 25LT01.

93.   Raizer, Y.P. and J.E. Allen, *Gas discharge physics*. Vol. 2. 1997: Springer Berlin.

94.	*COMSOL Multiphysics*, in *Multiphysics Reference Guide for COMSOL 5.5*. 2019: Burlington, MA, USA.

95.	Biagi, S.F., FORTRAN Program, MAGBOLTZ v8.97. Oct 2012.

96.	Alves, L. *The IST-LISBON database on LXCat*. in *Journal of Physics: Conference Series*. 2014. IOP Publishing.

97.	Kushner, M., *Electron Impact Processes Hybrid Plasma Equipment Model*. Personal Communication.

98.	Van Gaens, W. and A. Bogaerts, *Kinetic modelling for an atmospheric pressure argon plasma jet in humid air*. Journal of Physics D: Applied Physics, 2013. **46**(27): p. 275201.

99.	Peterson, J., A. Le Padellec, H. Danared, G. Dunn, M. Larsson, A. Larson, R. Peverall, C. Strömholm, S. Rosén, and M. Af Ugglas, *Dissociative recombination and excitation of N 2+: Cross sections and product branching ratios*. The Journal of chemical physics, 1998. **108**(5): p. 1978-1988.

100.	Sommerer, T.J. and M.J. Kushner, *Numerical investigation of the kinetics and chemistry of rf glow discharge plasmas sustained in He, N2, O2, He/N2/O2, He/CF4/O2, and SiH4/NH3 using a Monte Carlo-fluid hybrid model*. Journal of applied physics, 1992. **71**(4): p. 1654-1673.

101.	Appleton, J., M. Steinberg, and D. Liquornik, *Shock-Tube Study of Nitrogen Dissociation using Vacuum-Ultraviolet Light Absorption*. The Journal of Chemical Physics, 1968. **48**(2): p. 599-608.

102.	Billing, G.D. and E. Fisher, *VV and VT rate coefficients in N2 by a quantum-classical model*. Chemical Physics, 1979. **43**(3): p. 395-401.

103. Ahn, T., I.V. Adamovich, and W.R. Lempert, *Determination of nitrogen V–V transfer rates by stimulated Raman pumping.* Chemical Physics, 2004. **298**(1-3): p. 233-240.

104. Biagi, S.F., *Monte carlo simulation of electron drift and diffusion in counting gases under the influence of electic and magnetic field.* Nuclear Instruments and Methods in Physical Research Section A, 1999. **421**: p. 234 - 240.

105. Biagi, *www.LxCat.net.* retrieved on June 11, 2018.

106. IST-Lisbon, *www.LxCat.net.* retrieved on June 11, 2018.

107. Farouk, T., B. Farouk, A. Gutsol, and A. Fridman, *Atmospheric pressure methane–hydrogen dc micro-glow discharge for thin film deposition.* Journal of Physics D: Applied Physics, 2008. **41**(17): p. 175202.

108. Farouk, T., B. Farouk, and A. Fridman, *Computational studies of atmospheric pressure methane-hydrogen DC micro glow discharges.* IEEE Transactions on Plasma Science, 2010. **38**(2): p. 73 - 85.

109. White, R.D., R.E. Robson, B. Schmidt, and M.A. Morrison, *Is the classical two-term approximation of electron kinetic theory satisfactory for swarms and plasmas?* Journal of Physics D: applied physics, 2003. **36**(24): p. 3125.

110. Pitchford, L., S. ONeil, and J. Rumble Jr, *Extended Boltzmann analysis of electron swarm experiments.* Physical Review A, 1981. **23**(1): p. 294.

111. Pitchford, L. and A. Phelps, *Comparative calculations of electron-swarm properties in N 2 at moderate E N values.* Physical Review A, 1982. **25**(1): p. 540.

112.   Dujko, S., A. Markosyan, R. White, and U. Ebert, *High-order fluid model for streamer discharges: I. Derivation of model and transport data.* Journal of Physics D: applied physics, 2013. **46**(47): p. 475202.

113.   Markosyan, A., S. Dujko, and U. Ebert, *High-order fluid model for streamer discharges: II. Numerical solution and investigation of planar fronts.* Journal of Physics D: Applied Physics, 2013. **46**(47): p. 475203.

114.   Stephens, J., *A multi-term Boltzmann equation benchmark of electron-argon cross-sections for use in low temperature plasma models.* Journal of Physics D: Applied Physics, 2018. **51**(12): p. 125203.

115.   Hagelaar, G. and L. Pitchford, *Solving the Boltzmann equation to obtain electron transport coefficients and rate coefficients for fluid models.* Plasma Sources Science and Technology, 2005. **14**(4): p. 722.

116.   Lisovskiy, V., V. Koval, E. Artushenko, and V. Yegorenkov, *Validating the Goldstein–Wehner law for the stratified positive column of dc discharge in an undergraduate laboratory.* European Journal of Physics, 2012. **33**(6): p. 1537.

117.   Cacciatore, M., M. Capitelli, and C. Gorse, *Non-equilibrium dissociation and ionization of nitrogen in electrical discharges: the role of electronic collisions from vibrationally excited molecules.* Chemical Physics, 1982. **66**(1-2): p. 141-151.

118.   Boeuf, J. and E. Kunhardt, *Energy balance in a nonequilibrium weakly ionized nitrogen discharge.* Journal of applied physics, 1986. **60**(3): p. 915-923.

119.   Yao, J., C. Yuan, S. Eliseev, A. Kudryavtsev, and Z. Zhou, *Longitudinal structure and plasma parameters of an entire DC glow discharge as obtained using a 1D*

fluid-based model with non-local ionization. Plasma Sources Science and Technology, 2020. **29**(7).

120. Lisovskiy, V., V. Derevyanko, E. Artushenko, and V. Yegorenkov, *Stratification of the Positive Column of a DC Discharge in Nitrogen.* East European Journal of Physics, 2012(1017 (3)): p. 95-101.

CHAPTER 5 :

APPLICATION OF DIELECTRIC BARRIER DISCHARGE IN MISTY

PLASMA SYSTEMS FOR DISINFECTION[3]

5.1 INTRODUCTION

Recently, the application of cold atmospheric pressure plasmas, namely, dielectric barrier discharge (DBD) has been a topic of intense research in biological, medical, and environmental fields [121-133]. These kinds of plasmas are mostly nonequilibrium or nonthermal, produce negligible heat, have selective effects, and are environmentally friendly [121, 133-135]. Through the production of reactive oxygen and nitrogen species (RONS), which possess antimicrobial properties, nonthermal gaseous plasmas (NTGP) are found to stimulate cell growth, while also causing both bacterial and viral kills as well as biofilm inactivation. NTGP has the ability to disinfect high density of harmful microorganisms, heal and decontaminate wounds in a relatively short time depending on the type of microorganism treated, the type of discharge medium, and the plasma power density without affecting mammalian cells or creating any pollutant as a byproduct [136, 137].

The existing areas of application of gaseous plasmas in medicine can be broadly categorized into 4 segments: blood coagulation, ablation, incision, and cosmetic applications [137]. However, due to already stretched healthcare systems worldwide, there is a significant unmet global need for wound management with market size of approximately $13 billion and growing. Additionally, approximately 1.7 million healthcare-associated infections occur each year in the U.S., killing 98,000 patients [138] and COVID-19 has revealed further weaknesses in the preparedness of healthcare facilities, which lacked the ability to adequately disinfect existing personal protective equipment (PPE), exacerbating an already precarious situation. Thus, nonthermal based plasma technologies have the potential for sufficient market penetration.

Plasma treatment of biological samples can be categorized into two major methods: direct and indirect/remote [139]. In the direct method, the substrate to be treated is in direct contact with the discharge medium. Typically, the substrate is placed either on the grounded electrode or a dielectric connected to a powered electrode. In indirect or remote treatment, the DBD is ignited in an inert medium (e.g. a noble or inert gas) and the radicals and ionized species produced are transported to the target medium by gas flow [139, 140]. Hong et al. studied the inactivation efficiency of low-temperature plasmas (LTP) created by RF discharge on *E. coli* and *B. subtilis*, placed between a powered dielectric and a grounded electrode [141]. The discharge medium primarily consisted of helium with variable admixtures of oxygen. Oxygen radicals, generated in the discharge played the primary role in causing cytoplasmic damage and chromosome leakage to the bacterial samples [141]. Similar results have been presented by Laroussi et al., in which it was shown that without any admixture of oxygen in helium as the primary discharge medium, there was no bacterial disinfection of *E. coli* for the given conditions [142].

Min Shi et al. studied the deactivation efficiency of atmospheric pressure DBD on Hepatitis B virus (HBV) [143]. The HBV serum was coated on one of the dielectric surfaces and it was observed that HBV DNA count exponentially decreased with increasing exposure time of DBD. The interaction of RONS produced in the DBD with the lipids and proteins in the outer capsid of HBV is proposed as a probable deactivation mechanism [143]. Alekseev et al. studied the antiviral effect of nanosecond pulsed DBD on human corneal cells infected with herpes simplex virus type 1 (HSV-1) [133]. Exposure of 35-40 s resulted in deactivation of the HSV-1 virus, while also imparting no detectable toxicity or detrimental effects to human corneas [133]. Similar selectivity results have been found

by Fridman et al., in which, a floating electrode DBD (FE-DBD) was used to sterilize human tissue without incurring any detectable physical damage [133, 139]. It was also proved that the maximum non-toxic dose for tissue sterilization and blood coagulation by DBD is much stronger than that used in sterilization and blood coagulation. Joshi et al. showed that the same FE-DBD plasma was able to deactivate *E. coli, S. aureus,* and multidrug-resistant *S. aureus* in respective biofilm and planktonic forms [144]. Kalghatgi et al. showed that reactive species: both charged and neutrals produced by DBD plasmas can be 'tuned' by varying the discharge parameters to stimulate cell proliferation or even apoptosis [134]. Filipić et al. reported that, in general, 'cold plasmas' have demonstrated the capability to inactivate several types of viruses, namely, bacteriophages, FCV, Adenovirus, Influenza A & B, respiratory syncytial virus (RSV), HIV, avian influenza virus (AIV), Newcastle disease virus (NDV) and porcine reproductive and respiratory syndrome virus [135]. Capsid protein damage, nucleic acid disintegration, and changes in lipid components were reported as primary disinfection mechanisms. The different RONS that were responsible for such disintegration were O, O_3, H_2O_2, $ONOOH$, $ONOO^-$ and NO_x. However, it was to be noted that neither all degradation mechanisms not every RONS were applicable for each strain of virus.

Several studies have been conducted to investigate bacterial deactivation efficiency in the presence of water in a plasma discharge. NTPG in the presence of moisture is known to produce several RONS that include N, O, OH, NO, NO_2, and possibly more [38]. Purevdorj et al. studied that mortality of *B. pumilus* spores greatly improved when water is introduced with air in a low pressure microwave plasma discharge [145]. The increase in mortality is attributed to the increased production of OH, H, and O radicals and their

114

respective reaction pathways. Hanbal et al. studied the influence of DBD jet with air containing admixtures of water on Tobacco Mosaic viruses (TMV), which are resistant to physical and chemical agents [146]. It was observed that the RONS, namely HNO_2, NO_2^- and H_2O_2 produced in the plasma irradiation can degrade nucleic acids in TMV resulting in viral collapse to subunits. Muranyi et al. studied the effect of synthetic air with 0-80% relative humidity (RH) as a discharge medium in a cascaded dielectric barrier discharge (CDBD) on two strains of bacteria; they found that for *A. niger*, the bacterial mortality was the highest at 70% RH, whereas in case of *B. subtilis*, addition of any degree of RH deteriorated the mortality rate. The increased mortality of *A. niger* was attributed to the increased production of OH, which oxidizes the unsaturated fatty acids and proteins in the bacterial spores. The reduction in *B. subtilis* deactivation is attributed to the loss in discharge homogeneity of CDBD with increasing RH. Similar results have been portrayed by Falkenstein et al., which stated that despite the presence of water in DBD producing OH that increases oxidation, it also reduces micro discharges, thus reducing overall reactive species in the system. The latter effect is more pronounced when the reaction kinetics of OH with the target microorganism is relatively slow [147]. Maeda et al. applied RF discharge in air with variable 0-70% humidity on *E. coli* and found that the optimum deactivation is obtained at 43% RH, whereas no deactivation was observed at 0 and 70% RH [148]; no clear reason was given but the interaction between an increased number of water molecules and the powered electrode surfaces are stated to be a probable cause. Venzia et al. showed that moistened *G. stearothermophilus* spores showed no growth after indirect exposure to NTPG, which is contrary to dry conditions [149]. Moldgy et al. studied the decontamination efficiency of four different plasma sources on feline calicivirus and *S.*

Heidelberg and found that decontamination efficiency was increased with the presence of moisture [150]. The reactions of N_2O_5 with H_2O and H_2O_2, forming HOONO and $HOONO_2$, both of which have virucidal properties are stated to be responsible for the enhanced deactivation.

Despite such favorable outcomes in both bacterial and viral deactivation, nonthermal plasmas still face an uphill challenge to being established as a general medical practice due to interdisciplinary complexities and a lack of knowledge of the physicochemical processes that involve a multitude of charged species and excited neutrals [139]. Moreover, most DBD apparatus presented in the literature lacks the portability as well as the requirement of introducing a specified amount of water vapor to incorporate the optimum RH, which also introduces logistic complexities. Hence, the primary goal of this paper is to introduce an LTP technology that can be used to disinfect personal protective equipment (PPE), which does not bear a direct relationship to plasma medicine, yet. In this paper, we present a novel, relatively simple, portable, planar DBD device with an electrically insulated annular flow channel built through the planar powered electrode. The discharge medium is air saturated with water vapor that flows through the annulus and forms a stagnation discharge plane between the powered dielectric and the substrate. Application on *Escherichia (E.) coli.* and *Bacillus (B.) atrophaeus* on agar showed that usage of a flowing humid discharge medium has a ~40% higher efficacy than either a static or a dry flowing medium in culling bacterial colony forming units (cfu). *E. coli* is treated in its 'live' form whereas *B. atrophaeus* is treated in its 'sporulated' form, in which, these have thick spore coats protecting the bacterium until conditions become favorable for germination. This makes these bacilli highly resistant to conventional sterilization

procedures [149, 151-153]. Preliminary analyses indicated that the treated substrate turned acidic; in the presence of water vapor, pH can be decreased due to the formation and subsequent dissociation of hydrogen peroxide to H^+ and H_2O. Thus, the approach of dielectric barrier discharge in water vapor promises to be efficient at disinfecting PPEs, which include soft surfaces, against SARS-CoV-2 or other coronaviruses which are not as resilient as the spores against which current tests have proved successful.

5.2 EXPERIMENTAL METHOD AND DIAGNOSTIC SETUP

The experimental setup consists of compressed air passing through a bubble column, containing filtered water, at a flow rate of 10 slpm, Figure 5.1a. The resulting humid air, saturated with water vapor, at 298 K, 1 atm is passed concentrically through an in-house designed electrode assembly. When static conditions are tested, the airflow is turned off. In the case of studying airflow without adding water, an empty bubble column is used. The electrode assembly is positioned at 2 mm from the substrate, which, in turn, is placed on a ground plate. The substrate in the present experimental setup consists of agar media containing either *E. coli* or *B. atrophaeus*. The dielectric barrier discharge is initiated in the stagnation plane formed by the saturated air between the lower surface of the electrode (the dielectric itself) and the grounded substrate.

The construction of the electrode is detailed in Figure 5.1b. It consists of a circular sandblasted copper ring (OD 1.75", ID 0.39", thickness: 0.06"), which acts as the powered electrode, fused to the top surface of a circular quartz ring (OD 2", ID 0.25", thickness: 0.125"), which serves as the dielectric. The copper electrode is welded to a corona-resistant wire that is drilled into the Delrin housing from the top and connects the electrode to the power supply (not shown). The entire setup is housed in a Delrin block (OD 2", thickness:

2"). The inner diameter of the Delrin cylindrical block is drilled to Ø 0.25" from the bottom to a height of 0.25" and to a Ø 0.5" at the top to a depth of 1". A 0.25" compression fitting to 0.5" NPT" is fitted on the top of the housing to connect an inlet PFA tube carrying the water vapor saturated air. At the bottom of the housing, a quartz tube (OD 0.25", ID 0.16") is fitted and its walls are fused with adhesive to the inner walls of the dielectric. This tube serves as the passage for the saturated air to the ground to form the discharge stagnation plane.

A regulated 15-25 kV, 50-4000 Hz, 300W pulsed DBD power supply (Advanced Plasma Solutions) was used to initiate the DBD discharge in a stagnation plane of moisture saturated air. The DBD HV pulser is operated at 20kV, 1670 Hz with a pulse width of 0.3 ms. An Agilent mixed-signal oscilloscope MSO7054B (500 MHz, 4GS/s) was used to measure the discharge voltage and discharge current, Figure 5.1c. The voltage at the copper electrode was measured via a North Star PVM-4 1000:1 HV probe and the discharge current was measured at the ground with a Pearson 6515 current monitor. The power density was maintained at 0.87 W/cm^2. The optical emissions spectrometer of the discharge is captured with an integration time of 10 s by Ocean Optics HR4000 CG-UV-NIR with an optical fiber directed towards the center of the discharge plane.

5.3 STERILIZATION EFFICACY PROCEDURE

A suspension of 10^5 colony forming units (CFUs) per ml of *E. coli* (K-12 strain, ATCC 10798) and *B. atrophaeus* spores (BG-105, Crosstex Medical Company) were made separately in Luria-Bertani (LB, Fisher Scientific) and 1X phosphate-buffered saline (1XPBS), respectively, before the DBD treatment. Enumeration of both *E. coli* and *B. atrophaeus* spores were done through optical density measurement at 600 nm (OD600)

with a Biotek Synergy 2 microplate reader; quantification was done using 2 X 10^9 CFUs/OD600. 100 µl of the respective suspension containing 1 X 10^4 CFUs was spread solidified LB agar in 100x15mm petri dishes to a height of 0.5 cm.

(a)

(b)

(c)
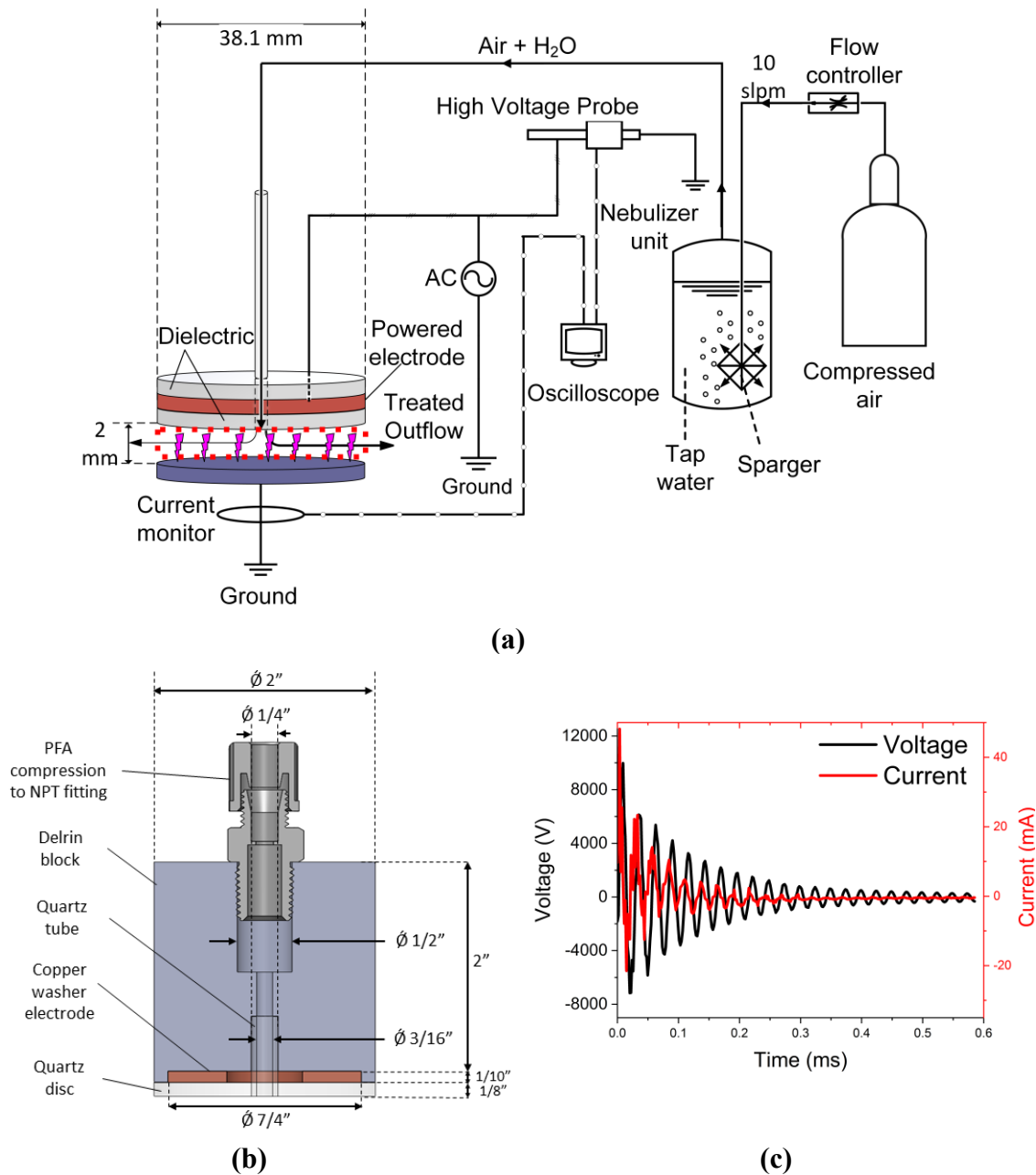
Figure 5.1 (a) Schematic of the experimental setup, **(b)** Detailed electrode configuration, **(c)** Single characteristic voltage and current pulse in the discharge

Each dish with either *E. coli* or *B. atrophaeus* is placed below the electrode such that the surface of the agar is 2 mm from the bottom plane of the dielectric. After the experiments, the petri dishes were incubated at 37°C for 24 hours to facilitate the growth of colonies. The colonies were later counted with Image J software.

5.4 RESULTS AND DISCUSSION

The dielectric barrier discharge is initiated in the stagnation plane formed by the saturated air between the lower surface of the electrode (the dielectric itself) and the grounded substrate. Figure 5.2 shows the visualization of the discharge without and with the influx of water vapor. Figure 5.2a shows that without the influx of air or water vapor, the DBD discharge is mostly non-uniform and filamentary. The discharge mostly emits the characteristic bluish color of nitrogen emissions. With the influx of moisture saturated air from the center of the top plane, the discharge becomes more uniform, and the filamentary nature is reduced, Figure 5.2b.

(a)

(b)
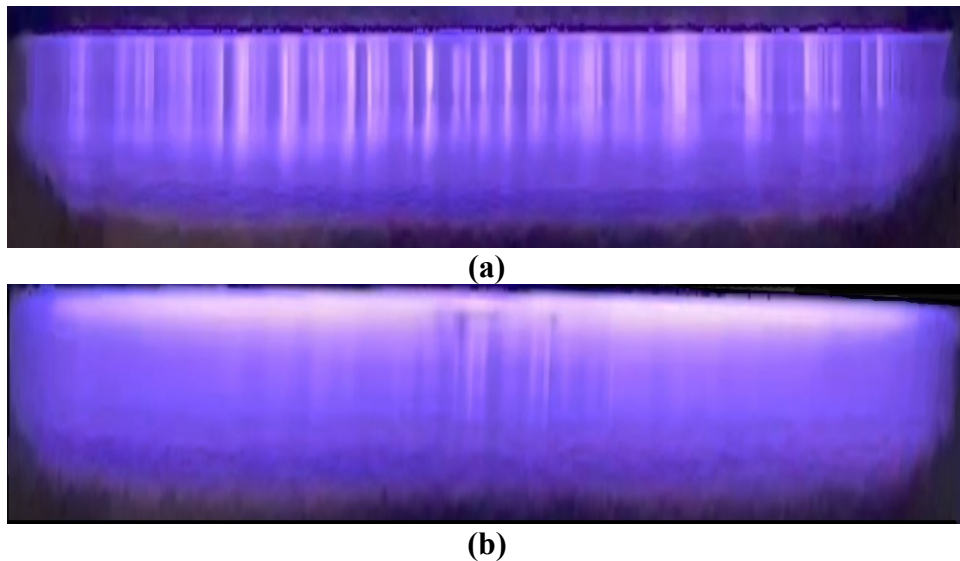
Figure 5.2 Visualization of the discharge structure **(a)** Without added humidity, **(b)** With added humidity

The experiments were conducted for three different discharge media: i) static ambient, ii) airflow with no water added at room temperature (298 K) and 1 atm, and iii) airflow saturated with water vapor at the same conditions. Multiple samples were treated at each condition to reduce statistical variance. Visual observation showed that after the same treatment duration, the petri dishes that were treated with moisture-saturated air shows the least number of colonies, Figure 5.3(a-d). Thus, DBD discharge in a humid airflow medium has the highest efficacy in disinfection compared to using static and flowing air as discharge media.

	Control	Static	Air	Air + H_2O
E. coli treated for 2 mins	(a)	(b)	(c)	(d)
B. Atrophaeus treated for 20 mins	(e)	(f)	(g)	(h)
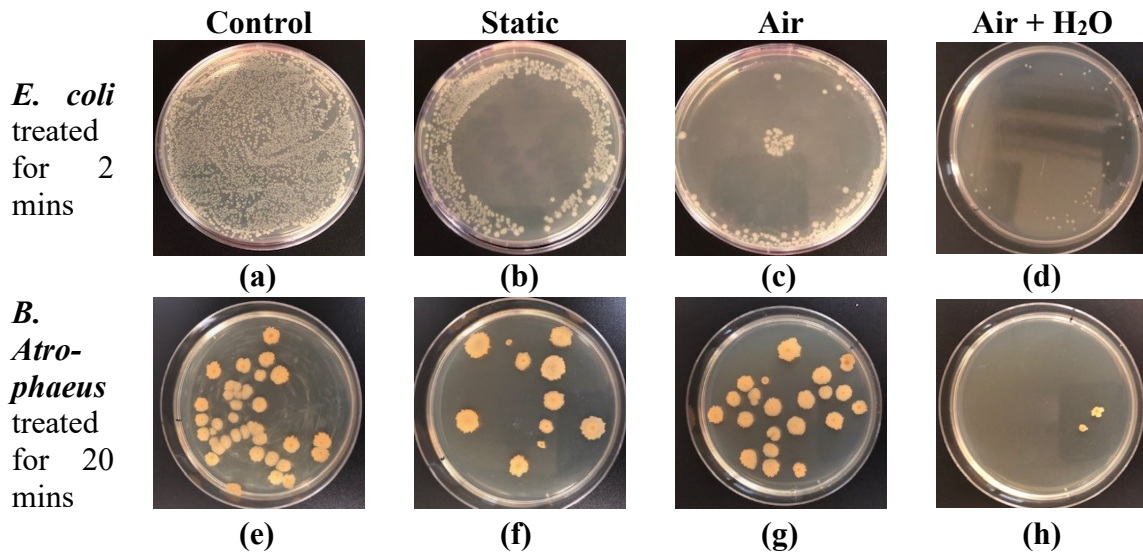
Figure 5.3 Comparison of the visual representation of the DBD treatment of **(a-d)** *E. coli,* **(e-h)** *B. atrophaeus*, for different discharge media and control

Since *B. atrophaeus* was treated in its sporulated form, it offered greater resistance to RONS from the plasma generation and thus, needed to be treated for a longer duration. It is observed that while, for *E. coli*, it was sufficient to treat for 2 mins to obtain maximum disinfection, *B. atrophaeus* did not show any noticeable effect of disinfection until the treatment time is longer than 10 mins. Similar to the case of *E. coli*, it is observed from

visual representation that petri dishes, which were treated with moisture saturated air as the discharge medium shows the least amount of bacillus, Figure 5.3(e-h). Thus, in the case of bacillus spores, the effectiveness of DBD with humid plasma is also superior to either of the other two discharge media.
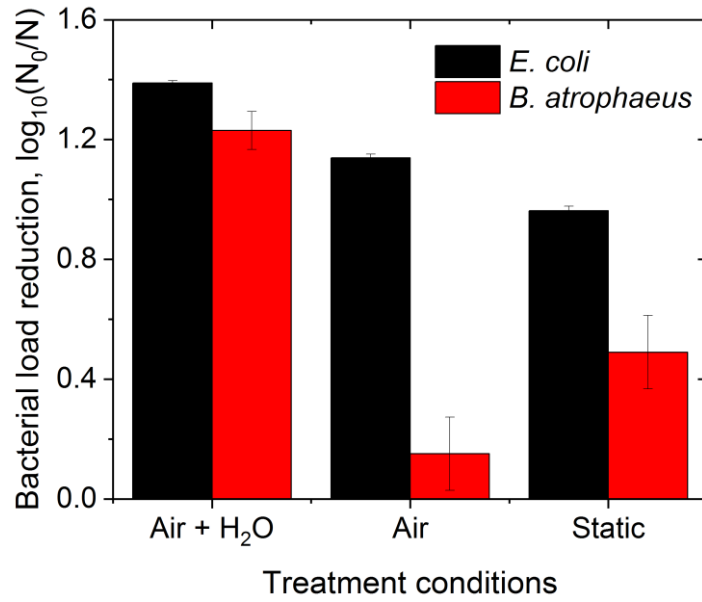
(a)
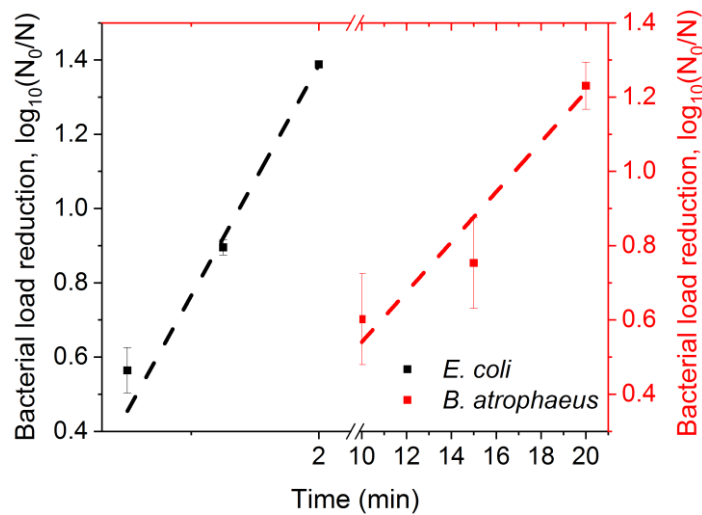
(b)

Figure 5.4 (a) Comparison of bacterial load reduction for different discharge media for *E. coli* and *B. Atropaheus*, **(b)** Temporal evolution of bacterial load reduction for DBD in Air + H_2O medium

As described in the previous sections, the bacterial colonies were counted after 24 hours of incubated growth with ImageJ software. The deactivation efficiency is calculated by a logarithmic reduction method described in [154] as $\log_{10}(N_0/N)$, where N_0 is the bacterial count in the control samples that did not undergo any sort of treatment and N is the bacterial count after undergoing DBD treatment. The visual representations of treatment effects of different discharge media are graphically portrayed in Figure 5.4a. This is in agreement with the visual observations showing the superiority of the moisture-laden airflow as the discharge medium. It can also be noted from Figure 5.4 (a) that compared to treatment under static conditions, adding humid airflow to the discharge medium increases the deactivation efficacy by ~1.5 and ~2.5 times for *E. coli* and *B. atrophaeus* respectively.

Experiments were conducted for different treatment durations. The *E. coli* were treated for treatment times of 0.5, 1.25, and 2 min; the *B. atrophaeus* petri dishes were treated for durations of 10, 15, and 20 minutes. Figure 5.4 (b) shows the dependence of bacterial load reduction on treatment times for only the moisture-saturated air as the discharge medium. It is observed that for both the bacterial strains, the bacterial load reduction increases in a linear correlation with treatment time. Figure 5.4 (b) also confirms that for *B. atrophaeus*, the minimum treatment time for noticeable bacterial load reduction is 5 times that is required for *E. coli* due to its spore-protection form. For both *B. atrophaeus* spores and *E. coli* colonies, the DBD in the humid medium proved to be of the highest effectiveness. The effectiveness could be due to OH radicals, since they are strong oxidizing agents that react with cell membranes, denature the nucleic lipids and proteins in the bacterial cells, and thus deactivate the bacteria. This may be attributed to the higher concentration of OH, H, O, and H_2O_2 being generated from DBD discharge in the presence

of a greater degree of water. Optical emission spectra of the discharge show the presence

of OH(A-X) band at 306-312 nm [155] and reactive nitrogen species (N_2 2nd +ve, 337-410

nm [156]) in the discharge, Figure 5.5a. Direct reliable, accurate quantification of OH and

other reactive species is beyond the scope of the present work.
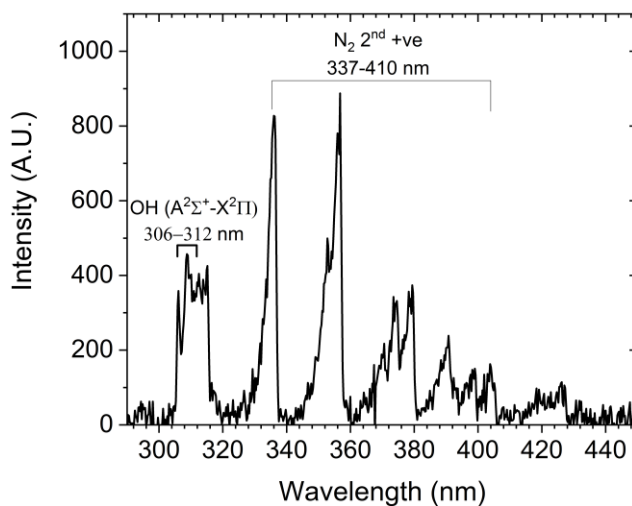
(a)
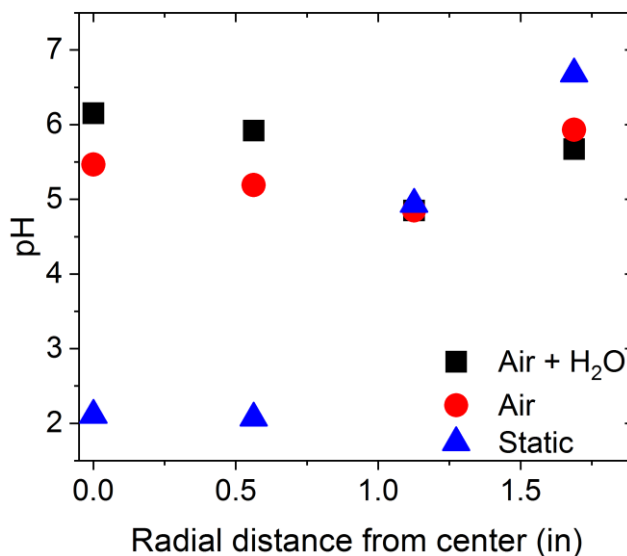
(b)

Figure 5.5 (a) Optical emission spectra of the discharge plane showing the OH and N_2
2nd positive emission bands, **(b)** Radial variation of pH from the agar center, post
treatment

OH, radicals are highly reactive and the combination of two OH radicals produced in plasma discharge to form one molecule of H_2O_2 in the afterglow can be regarded as a possible decay mechanism of OH. Since H_2O_2 is acidic, its formation is supposed to lower the pH. Thus, pH measurement of the treated medium is adopted as an indirect method to assess treatment effectiveness. The agar medium is treated for 25 mins with all of the three discharge mediums and the radial variation of pH from the center of influx is measured using Horiba LAQUAtwin pH-22 Compact Meter. Figure 5.5b shows that the static conditions induce the largest pH drop but with the smallest treatment range i.e., localized since it had no induced flow and thus no convective species transport. Despite DBD in both 'air' and 'air + H_2O' having comparable treatment ranges, air + H_2O, induces a slightly larger pH drop farthest away from the center. The drop in pH of the medium in static and dry airflow conditions may be attributed to low-oxidizing radicals and neutrals that do not primarily originate from the presence of water. Furthermore, in further experiments (not shown here), it is seen that the presence of O_2 enhances the production of H_2O_2 in plasma NTP discharge in presence of H_2O. This may explain why DBD in static conditions was not able to considerably deactivate *B. atrophaeus* spores despite lowering the pH by the greatest degree. The increase in acidity of the medium in presence of water vapor can be potentially due to the formation and subsequent dissociation of H_2O_2, formation of peroxynitric acid ($HOONO_2$) and peroxynitrous acid ($HOONO$), all of which have bactericidal properties [150] but may not drastically decrease pH since these are not direct deposited on the substrate due to being associated with a radial convective flow. A sharp drop in pH might also be undesirable for medical applications.
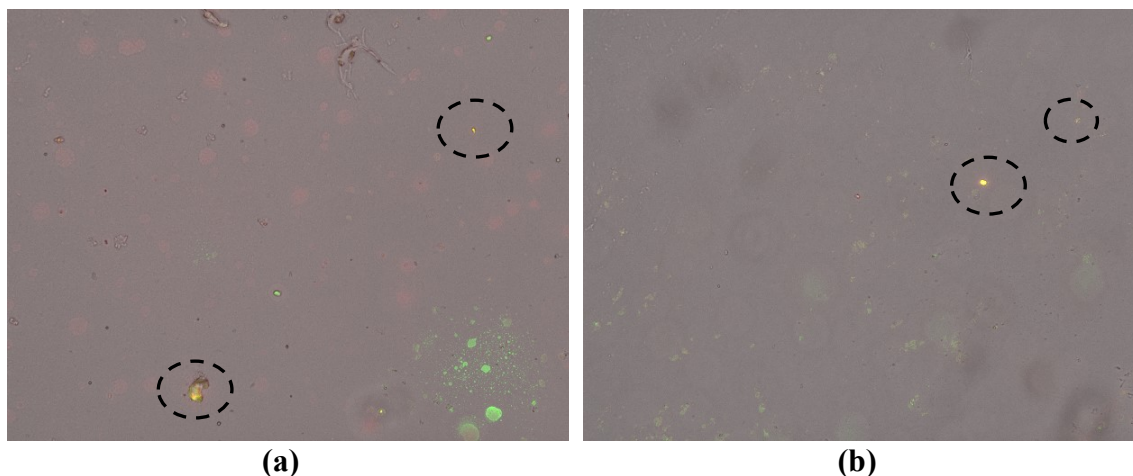
Figure 5.6 DBD-treated strains of **(a)** *E. coli* and **(b)** *B. atrophaeus*, stained with Sybr green and PPI to reveal dead DNA

To analyze the cause of the deactivation of the treated stains, live/dead experiments were conducted on the treated samples. Both the treated strains of bacteria are treated with Sybr green and subsequently with propidium iodide (PI). Sybr green can penetrate both live and dead cells whereas PI can penetrate only dead cells. Both Figure 5.6a and Figure 5.6b show that *E. coli* and *B. atrophaeus* exhibit yellow stains which indicate the presence of both Sybr green and PI. This confirms that the bacterial cells have indeed been 'killed' by the DBD plasma.

5.5 CONCLUSIONS

In this work, we have compared bacterial load reduction of two different strains: *E. coli* and *B. atrophaeus* via nonthermal dielectric barrier discharge plasma operating at atmospheric pressure with three different discharge media. It was demonstrated that using air saturated with water vapor at 298 K and 1 atm as a plasma medium increases the disinfection effectiveness for both strains. A treatment time of 20 mins with humid plasma was necessary to achieve maximum disinfection with *B. atrophaeus* spores, whereas an

exposure time of 2 mins was deemed sufficient to disinfect *E. coli*. Optical emission spectroscopy and pH measurement show the presence of OH(A-X) bands, N_2 2nd positive systems, and possibly H_2O_2, generated in the discharge. It was also noted that in the case of humid air, the pH change was prevalent over the longest distance from the influx point, signifying the largest treatment range. It was also able to impart maximum deactivation efficacy with the least change in pH of the overall culture medium. Based on the efficacy, it could be said with reasonable confidence that it will be a successful tool against viruses as well.

Furthermore, an agar surface was treated which can be classified as soft and has ramifications for disinfecting surfaces of PPEs, mask airways, tubing, often touched locations such as arms of sofas/chairs, patient stirrups, straps if present, and the mist can penetrate hard to reach areas such as in-between computer keyboards or behind monitors. The approach of DBD in water vapor promises to be efficient at disinfecting items such as PPEs enabling quick, safe, and efficient re-use. Furthermore, the fact that DBD discharge in presence of water vapor promotes maximum deactivation efficacy without incurring any significant change in the pH of the medium is promising and the involved processes need further investigation.

5.6 ACKNOWLEDGEMENT

5.7 REFERENCES

38.   Wilson, A., D. Staack, T. Farouk, A. Gutsol, A. Fridman, and B. Farouk, *Self-rotating dc atmospheric-pressure discharge over a water-surface electrode: regimes of operation.* Plasma Sources Science and Technology, 2008. **17**(4): p. 045001.

121.   Li, Y., R. Atif, K. Chen, J. Cheng, Q. Chen, Z. Qiao, G. Fridman, A. Fridman, and H.-F. Ji, *Polymerization of d-ribose in dielectric barrier discharge plasma.* Plasma, 2018. **1**(1): p. 144-149.

122.   Na, Y.H., G. Park, E.H. Choi, and H.S. Uhm, *Effects of the physical parameters of a microwave plasma jet on the inactivation of fungal spores.* Thin solid films, 2013. **547**: p. 125-131.

123.   Laurita, R., A. Miserocchi, M. Ghetti, M. Gherardi, A. Stancampiano, V. Purpura, D. Melandri, P. Minghetti, E. Bondioli, and V. Colombo, *Cold atmospheric plasma treatment of infected skin tissue: evaluation of sterility, viability, and integrity.* IEEE Transactions on Radiation and Plasma Medical Sciences, 2017. **1**(3): p. 275-279.

124.   Yan, D., J.H. Sherman, and M. Keidar, *Cold atmospheric plasma, a novel promising anti-cancer treatment modality.* Oncotarget, 2017. **8**(9): p. 15977.

125.   Laroussi, M., M. Kong, G. Morfill, and W. Stolz, *Plasma medicine: applications of low-temperature gas plasmas in medicine and biology.* 2012: Cambridge University Press.

126.   Ercan, U.K., S.S. Joshi, A. Yost, S. O'Toole, M. Paff, E. Melchior, S.G. Joshi, and N. Gogotsi, *Inhibition of biofilms by non-thermal plasma treated novel solutions.* Advances in Microbiology, 2014. **4**(16): p. 1188.

127.   Fridman, G., M. Peddinghaus, M. Balasubramanian, H. Ayan, A. Fridman, A. Gutsol, and A. Brooks, *Blood coagulation and living tissue sterilization by floating-electrode dielectric barrier discharge in air.* Plasma Chemistry and plasma processing, 2006. **26**(4): p. 425-442.

128.   Kalghatgi, S.U., G. Fridman, M. Cooper, G. Nagaraj, M. Peddinghaus, M. Balasubramanian, V.N. Vasilets, A.F. Gutsol, A. Fridman, and G. Friedman, *Mechanism of blood coagulation by nonthermal atmospheric pressure dielectric barrier discharge plasma.* IEEE Transactions on plasma science, 2007. **35**(5): p. 1559-1566.

129.   Kalghatgi, S., G. Friedman, A. Fridman, and A.M. Clyne, *Endothelial cell proliferation is enhanced by low dose non-thermal plasma through fibroblast growth factor-2 release.* Annals of biomedical engineering, 2010. **38**(3): p. 748-757.

130.   Coulombe, S., V. Léveillé, S. Yonson, and R. Leask, *Miniature atmospheric pressure glow discharge torch (APGD-t) for local biomedical applications.* Pure and Applied Chemistry, 2006. **78**(6): p. 1147-1156.

131.   Shekhter, A.B., V.A. Serezhenkov, T.G. Rudenko, A.V. Pekshev, and A.F. Vanin, *Beneficial effect of gaseous nitric oxide on the healing of skin wounds.* Nitric oxide, 2005. **12**(4): p. 210-219.

132. Smith, J.B., I. Adams, and H.-F. Ji, *Biomolecule response to nonthermal plasma.* Plasma Medicine, 2017. **7**(4).

133. Alekseev, O., K. Donovan, V. Limonnik, and J. Azizkhan-Clifford, *Nonthermal dielectric barrier discharge (DBD) plasma suppresses herpes simplex virus type 1 (HSV-1) replication in corneal epithelium.* Translational vision science & technology, 2014. **3**(2): p. 2-2.

134. Kalghatgi, S., C.M. Kelly, E. Cerchar, B. Torabi, O. Alekseev, A. Fridman, G. Friedman, and J. Azizkhan-Clifford, *Effects of non-thermal plasma on mammalian cells.* PloS one, 2011. **6**(1): p. e16270.

135. Filipić, A., I. Gutierrez-Aguirre, G. Primc, M. Mozetič, and D. Dobnik, *Cold plasma, a new hope in the field of virus inactivation.* Trends in Biotechnology, 2020. **38**(11): p. 1278-1291.

136. Laroussi, M., I. Alexeff, and W.L. Kang, *Biological decontamination by nonthermal plasmas.* IEEE Transactions on Plasma Science, 2000. **28**(1): p. 184-188.

137. Lloyd, G., G. Friedman, S. Jafri, G. Schultz, A. Fridman, and K. Harding, *Gas plasma: medical uses and developments in wound care.* Plasma Processes and Polymers, 2010. **7**(3-4): p. 194-211.

138. Haque, M., M. Sartelli, J. McKimm, and M.A. Bakar, *Health care-associated infections–an overview.* Infection and drug resistance, 2018. **11**: p. 2321.

139. Fridman, G., G. Friedman, A. Gutsol, A.B. Shekhter, V.N. Vasilets, and A. Fridman, *Applied plasma medicine.* Plasma processes and polymers, 2008. **5**(6): p. 503-533.

140. Malyavko, A., D. Yan, Q. Wang, A.L. Klein, K.C. Patel, J.H. Sherman, and M. Keidar, *Cold atmospheric plasma cancer treatment, direct versus indirect approaches.* Materials Advances, 2020. **1**(6): p. 1494-1505.

141. Hong, Y., J. Kang, H. Lee, H. Uhm, E. Moon, and Y. Park, *Sterilization effect of atmospheric plasma on Escherichia coli and Bacillus subtilis endospores.* Letters in applied microbiology, 2009. **48**(1): p. 33-37.

142. Laroussi, M., C. Tendero, X. Lu, S. Alla, W.L.J.P.P. Hynes, and Polymers, *Inactivation of bacteria by the plasma pencil.* 2006. **3**(6-7): p. 470-473.

143. Shi, X.-M., G.-J. Zhang, X.-L. Wu, Z.-Y. Peng, Z.-H. Zhang, X.-J. Shao, and Z.-S. Chang, *Effect of low-temperature plasma on deactivation of hepatitis B virus.* IEEE Transactions on Plasma Science, 2012. **40**(10): p. 2711-2716.

144. Joshi, S.G., M. Paff, G. Friedman, G. Fridman, A. Fridman, and A.D. Brooks, *Control of methicillin-resistant Staphylococcus aureus in planktonic form and biofilms: a biocidal efficacy study of nonthermal dielectric-barrier discharge plasma.* American journal of infection control, 2010. **38**(4): p. 293-301.

145. Purevdorj, D., N. Igura, O. Ariyada, and I.J.L.i.a.m. Hayakawa, *Effect of feed gas composition of gas discharge plasmas on Bacillus pumilus spore mortality.* 2003. **37**(1): p. 31-34.

146. Hanbal, S.E., K. Takashima, S. Miyashita, S. Ando, K. Ito, M.M. Elsharkawy, T. Kaneko, and H. Takahashi, *Atmospheric-pressure plasma irradiation can disrupt tobacco mosaic virus particles and RNAs to inactivate their infectivity.* Archives of virology, 2018. **163**(10): p. 2835-2840.

147. Falkenstein, Z. and J.J.J.J.o.P.D.A.P. Coogan, *Microdischarge behaviour in the silent discharge of nitrogen-oxygen and water-air mixtures.* 1997. **30**(5): p. 817.

148. Maeda, Y., N. Igura, M. Shimoda, and I.J.A.b. Hayakawa, *Inactivation of Escherichia coli K12 using atmospheric gas plasma produced from humidified working gas.* 2003. **23**(4): p. 389-395.

149. Venezia, R.A., M. Orrico, E. Houston, S.-M. Yin, and Y.Y. Naumova, *Lethal activity of nonthermal plasma sterilization against microorganisms.* Infection Control & Hospital Epidemiology, 2008. **29**(5): p. 430-436.

150. Moldgy, A., G. Nayak, H.A. Aboubakr, S.M. Goyal, and P.J. Bruggeman, *Inactivation of virus and bacteria using cold atmospheric pressure air plasmas and the role of reactive nitrogen species.* Journal of Physics D: Applied Physics, 2020. **53**(43): p. 434004.

151. Schinköthe, J., H.A. Scheinemann, S. Diederich, H. Freese, M. Eschbaumer, J.P. Teifke, and S. Reiche, *Airborne Disinfection by Dry Fogging Efficiently Inactivates Severe Acute Respiratory Syndrome Coronavirus 2 (SARS-CoV-2), Mycobacteria, and Bacterial Spores and Shows Limitations of Commercial Spore Carriers.* Applied and Environmental Microbiology, 2021. **87**(3): p. e02019-20.

152. Rattanakul, S. and K. Oguma, *Inactivation kinetics and efficiencies of UV-LEDs against Pseudomonas aeruginosa, Legionella pneumophila, and surrogate microorganisms.* Water research, 2018. **130**: p. 31-37.

153. Zhang, C., Y. Li, C. Wang, and X. Zheng, *Different inactivation behaviors and mechanisms of representative pathogens (Escherichia coli bacteria, human adenoviruses and Bacillus subtilis spores) in g-C3N4-based metal-free visible-*

light-enabled photocatalytic disinfection. Science of The Total Environment, 2021. **755**: p. 142588.

154. Gershman, S., M.B. Harreguy, S. Yatom, Y. Raitses, P. Efthimion, and G. Haspel, *A low power flexible dielectric barrier discharge disinfects surfaces and improves the action of hydrogen peroxide.* Scientific reports, 2021. **11**(1): p. 1-12.

155. Qazi, H., Q.-Y. Nie, H.-P. Li, X.-F. Zhang, and C.-Y. Bao, *Comparison of electrical and optical characteristics in gas-phase and gas-liquid phase discharges.* Physics of Plasmas, 2015. **22**(12): p. 123512.

156. Georgescu, N., C.P. Lungu, A.R. Lupu, and M. Osiac, *Atomic oxygen maximization in high-voltage pulsed cold atmospheric plasma jets.* IEEE transactions on plasma science, 2010. **38**(11): p. 3156-3162.

CHAPTER 6 :

IMAGING MEASUREMENTS OF ABSOLUTE OH AND H_2O_2

CONCENTRATIONS IN A HE-H_2O NANOSECOND PULSED

ATMOSPHERIC PRESSURE DIELECTRIC BARRIER DISCHARGE JET

BY PHOTO-FRAGMENTATION LASER-INDUCED FLUORESCENCE[4]

---

[4] Tahiyat, M. M., D. V. D. Bekerom, E. Huang, , J. H. Frank and T. I. Farouk, *Absolute OH and H_2O_2 density measurements in nanosecond pulsed He-H_2O and He-H_2O-O_2 in near atmospheric pressure dielectric barrier discharge afterglow by photo-fragmentation laser-induced fluorescence.* To be submitted to Plasma Sources Science & Technology.

6.1 INTRODUCTION

In recent times, nonthermal plasma (NTP) discharges in presence of water have found a widespread scope of research in environmental [157-159], biomedical [134, 160, 161], and catalysis [162-164] applications. The primary reason for this immense interest is the production of reactive oxidizing species from NTP discharge in humid medium, namely OH and H_2O_2, which take active roles in the aforementioned physicochemical processes. In wastewater treatment, ozone and OH are the primary species responsible for the oxidation of organic contaminants in liquid [157] and gaseous states [159]. Both OH and H_2O_2 are prominent oxidizers in plasma-activated water that has shown to possess antibacterial effects [158, 160]. OH, H_2O_2 and O_3 generated from NTP via dielectric barrier discharge (DBD) was also found to promote proliferation when NTP is applied to mammalian cells [134]. The OH radicals generated from NTP also showed promise in the treatment of cancer cells [161]. It was observed that plasma-catalytic destruction of volatile organic compounds (VOCs) increased in efficiency due to the formation of OH in the presence of humid air [162, 164]. Hydroxylation reactions were also found to be one of the primary pathways for the catalytic breakdown of pharmaceutical wastes [163]. Thus, to understand discharge chemistry and conditions responsible for the generation of these oxidizing species, it is imperative to know their respective discharge distribution for different operating parameters.

Most experimental efforts in the literature have attempted to use laser-induced fluorescence (LIF) to quantify OH distribution in nano-second pulsed (NSP) discharges. However, these attempts have usually involved trace water vapor in carrier gases: nitrogen [165], helium [29-31], argon [29], and synthetic air [24, 25]. In most cases, a frequency-

doubled dye laser- synchronized with a high voltage pulsar- is used to generate 282 nm photons, which excite OH in a timed discharge; the resultant fluorescence is captured with an ICCD camera with a 313 nm optical filter coupled with a spectrometer [31]. The OH concentration is usually found via a chemical model or UV absorption spectroscopy.

Optical emission spectroscopy (OES) of pulsed corona discharge in water has been studied previously for both liquid and bubble modes [166]. Stark broadening of the H_β line was used to measure electron number density (n_e) and the gas temperature (T_g) was measured from the rotational temperature of N_2(C-B) lines. Both n_e, emission intensities of OH, H, and O as well as chemical reactivity -deduced by measuring the production rate of H_2O_2- were found to be significantly larger in the liquid state than in the bubble state whereas T_g was ~ 300 K higher in the liquid mode [166].

The OH number density measurements in the afterglow of an NSP discharge in He + trace H_2O were compared from three different techniques: UV absorption, LIF calibrated with Rayleigh scattering, and chemical modeling were all found to correspond within experimental uncertainty [33]. The spatial density distribution of OH in an NSP discharge in a He-H_2O mixture was studied with LIF for two different discharge power densities [31]. It was observed that for low power, OH is mostly concentrated in the middle of the discharge whereas for the higher power, OH was mostly present at the periphery and the discharge core appeared dissociated. It was deduced from a chemical model that in the latter case, the dissociated core resulted from charge exchange and dissociative recombination of atomic ions and OH^+. The OH density in NSP discharge of an N_2-H_2O mixture also showed a drop in OH at the core, which was expected to be due to a higher OH decay rate due to core kinetics involving larger local densities of N and N^+ [165]. For

a similar discharge geometry and gas mixture, it was observed that the maximum OH density was found in the afterglow at 1-2 μs after the discharge current pulse [30]. This OH spike in the afterglow was attributed to the charge transfer reactions from atomic ions to H_2O and electron-water ion recombination reactions. The absolute number density of OH had also been measured by broadband UV absorption spectroscopy for He-H_2O mixture in RF glow discharge, using 310 nm UV LED [27]. For different humidity and power densities, the OH number densities were found to be in the range of 10^{19} -10^{20} m^{-3} for temperatures between 345-410 K. Discharge morphology of DBD with H_2O in presence of He and Ar was studied with ICCD imaging and broadband absorption [29]. The difference in OH density wrt H_2O concentration for the two gases was attributed to the change in the number of micro discharge filaments, surface charge intensity, and kinetic losses. LIF measurements in a pulsed arc discharge in $H_2O/O_2/N_2$ mixture, showed that OH increased with both humidity and oxygen content due to the formation of additional reaction pathways [25]. Spatial and temporal temperature measurements for a pulsed positive corona discharge for a similar gas mixture showed that, in the afterglow, the temperature at the anode is higher than in the rest of the discharge volume [24]. This was attributed to the lower OH decay rate at the anode owing to the comparative lack of OH forming reaction pathways in the rest of the discharge volume. In a nozzle-to-plane dc streamer corona discharge, 2-D LIF showed that OH radicals were produced mostly within the streamers and the shape of these streamers was affected by the presence of metastables from associated carrier gases [23]. LIF measurements in atmospheric pressure DBD in He-H_2O mixture had shown that comparative dependence of OH density was greater on the water vapor content than on discharge current; the maximum value at saturated vapor pressure

was found to be 10^{13} cm^{-3} [167]. Even though LIF measurements of OH and T_g in trace water in presence of He, N_2 and O_2 had been well researched in pulsed dc systems, similar measurements of OH and H_2O_2 in high water content in a DBD system had been scarce. Moreover, most chemical models used to calculate OH density did not include the OH decay recombination reactions to form H_2O_2.

Since H_2O_2 was not known to fluoresce in any known wavelength, photofragmentation LIF (PF-LIF) was adopted to detect and quantify H_2O_2. In the PFLIF technique, a pump photon (213 nm or 266 nm) photo dissociates a parent molecule (in this case, H_2O_2) into fragments (i.e. OH) that are detected by a probe photon (282 nm) using LIF [168, 169]. The 213 nm is generated from the fifth harmonic of an Nd: Yag laser, whereas 266 nm is generated from a frequency quadrupled Nd:Yag laser. Previous studies in combustion physics measured H_2O_2 by using a 266 nm laser to photo-dissociate each H_2O_2 molecule into two OH radicals which were, in turn, excited by LIF, and the resulting signals were detected [170, 171]. A technique for measuring both H_2O and H_2O_2 had been studied by combining PF-LIF and Two-Photon LIF (2P-LIF): KrF excimer laser at 248.28 nm is used to induce broadband fluorescence (400-500 nm) from H_2O molecules via 2P-LIF and simultaneously photo dissociate H_2O_2; 281.9 nm from a frequency-doubled dye laser was used to fluoresce resulting OH after 50 ns [169]. PF-LIF signal yield from H_2O at room temperatures was also deemed negligible compared to that from H_2O_2. Despite multiple applications in combustion physics, PF-LIF to detect H_2O_2 in non-thermal plasma is virtually nonexistent in literature and thus, will contribute to a new development in this area.

In this research, we studied the time-evolved generation of OH and H_2O_2 from a near-atmospheric pressure (600 Torr) dielectric barrier discharge in two different carrier gas mixtures: He-H_2O mixture at the highest attainable water vapor concentration at 283K with and without 5% O_2 admixture. The planar distribution of H_2O_2 and OH were measured using PF-LIF and LIF respectively. He is used as the carrier gas since it has lesser reaction pathways that involve OH kinetics that is expected to facilitate modeling the discharge [30] and being the only monatomic inert gas, possesses lower quenching ability than other polyatomic inert gases. The H_2O_2 concentration was calibrated by flowing a He-H_2O_2 mixture through the six-way cross reactor and the concentration of H_2O_2 was measured using absorption spectroscopy during calibration. The OH concentration was calibrated from a chemical model. The results from these experiments will serve as a kinetic model validation target since such data for high water vapor concentration is not readily available in the literature. The data will also provide important insights into the kinetics and disinfection mechanism of He-H_2O NTP discharge.

6.2 EXPERIMENTAL SETUP

The schematic of the experimental setup is shown in Figure 6.1a. He gas is continuously passed through an MKS mass flow controller at 500 sccm following a bubbler containing deionized water in a water bath (not shown here) at 283 K. The temperature of the water bath was kept 10 K below room temperature to prevent unwanted condensation in the exit lines. The resultant He-H_2O mixture flows from the top of the electrode through the center and forms a stagnation plane in the 4 mm interelectrode spacing between the quartz dielectric and a grounded SS plate (not shown here). The entire electrode assembly is placed in a 6 -way cross cell (not shown here), which is pressurized with He at 600 Torr.

The water vapor concentration is calculated by the assumption that the He-H$_2$O mixture flowing out of the electrode nozzle in the bottom is saturated with water vapor at 278 K. TPS DVX –(10 kV, 15 mA), operating on burst mode, is used to provide high voltage pulses to the powered electrode. The frequency of the burst mode is controlled by a function generator synchronized with a delay generator. The delay generator is also used to time the lasers and the ICCD cameras in accordance with the voltage pulse. The jitter in the signals, recorded from the oscilloscope is ~2 ns. The voltage and current profiles were recorded with a North Star PVM-4 high voltage probe and Pearson 6015 current monitor.
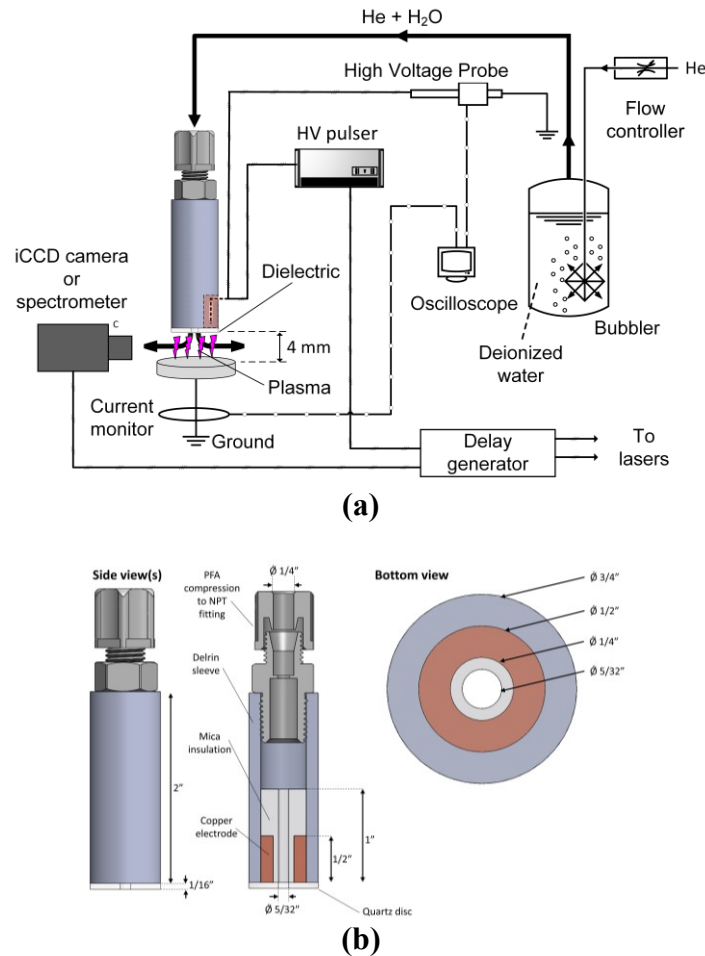
Figure 6.1 (a) Schematic of the experimental setup, **(b)** Detailed configuration of the electrode

6.3 ELECTRODE CONFIGURATION

The detailed configuration of the powered electrode is shown in Figure 6.1b. It consists of a powered copper cylinder housed concentrically in a Delrin cylindrical block. A tapered mica cylinder is drilled into the copper to induce structural rigidity as well as discharge leaking from the sides of the copper. A concentric channel is drilled into the mica as well to flow the He-H_2O mixture. Finally, a quartz dielectric with a center hole is fused to the copper and Delrin using an adhesive with high dielectric strength.

The schematic of the laser generation system for LIF and PFLIF diagnostics is shown in Figure 6.2a. The 5th harmonic from Nd:Yag laser (Continuum Surelite) was used to generate the photodissociation beam (213 nm) to fragment H_2O_2 to OH radicals. A tuned frequency-doubled dye laser (Lambda-Physik), with Rhodamine 6 G dye, pumped by an Nd:Yag laser (Quanta-Ray) was used to generate an excitation beam (282.594 nm), which, induced fluorescence from OH at 315 nm. The benefits of using this transition are mentioned in [31]. To measure OH generated solely from the DBD, the 213 nm beam was blocked with a beam dump. The laser pulses were produced at a frequency of 10 Hz. The intensity of the laser pulses was measured with a photodiode ('name') connected to an oscilloscope ('Tektronix'). The laser energy per pulse for 213 nm and 282.594 nm beams were 0.3 μJ and 0.1 mJ respectively with a variation of ± 4%.

6.4 LASER DIAGNOSTICS SETUP

(a)

(b)

Figure 6.2 (a) Schematic of laser generation, **(b)** Schematic of LIF detection

Figure 6.2b shows the LIF detections setup in more detail. The two beams were aligned bypassing those through two apertures placed as shown by adjusting the reflector for each beam. A cylindrical quartz lens of a focal length of 500 mm is used to create a laser plane of a thickness of 10 nm and a knife-edge is used to cut the laser plane to a height of 4 mm so that there is insignificant fluorescence from the sides of the electrode. A UVFS sampler is used to transmit 10% of the incident laser radiation to a separate camera for measuring beam profiles. The six-way cross housing the electrode is connected to a Brewster window to allow beam exit. The fluorescence signal from the DBD discharge is collected through an ICCD camera (Andor) with a Nikkor 105 mm f/2.5 UV lens through one of the quartz windows, perpendicularly to the beam path. A bandpass filter with a central wavelength of 315 nm with an FWHM of 10 nm is connected to the ICCD camera to filter out unwanted signals.

6.5 GAS TEMPERATURE MEASUREMENT

The gas temperature was measured from the rotational temperature of the OH (A, v'=1) state. This is measured by spectrally resolving the fluorescence signal of the OH (A, v'=1) state when the ground state is excited using the $P_1(2)$ transition. Assuming the time scale for the rotational energy transfer is much less than the lifetime of the excited state, the gas temperature can be said to be equal to the rotational temperature of the excited state. A spectrally resolved fluorescence signal is compared to that generated from LIFBASE [172] and the rotational temperature is calculated from the fit.

6.6 ABSOLUTE CALIBRATION FOR H_2O_2

Absolute calibration of H_2O_2 PF-LIF signals is performed using a He-H_2O-H_2O_2 reference mixture, which consists of a 2 slm flow of He bubbling throw a 50%(wt.) hydrogen peroxide solution, maintained at 283 K by a temperature-controlled water bath. As discussed below, the mole fraction of hydrogen peroxide vapor in the mixture is much smaller than that of water, and so it may be assumed that quenching is dominated by water. Collisional quenching rates of OH(A) in the reference mixture are the same as in the experiment, eliminating the need for fluorescence yield correction. The absolute hydrogen peroxide profile $\boldsymbol{x}_{HP}$ is then directly obtained by the ratio of PF-LIF signals in the experiment and reference mixture: $\boldsymbol{x}_{HP} = \frac{I_{PFLIF} - I_{LIF}}{I_{PFLIF}^{ref} - I_{LIF}^{ref}} x_{HP}^{ref}$, where $\boldsymbol{I}_{PF-LIF}$ is the PF-LIF image in the experiment, $\boldsymbol{I}_{PF-LIF}^{ref}$ the PF-LIF image in the reference mixture, x_{HP}^{ref} is the H_2O_2 mole fraction in the reference mixture, and boldface symbols signify 2D images.

Mole fractions of water and H_2O_2 could in principle be estimated by their vapor pressures. To calculate the vapor pressures for the hydrogen peroxide solution, we used Raoult's modified law following [173]. The expected vapor pressures and mole fractions are shown in Table 6.1 below:

Table 6.1 Expected water vapor and mole fractions of H_2O and H_2O_2 for different temperatures

	T = 283.14 K	T = 293.14 K:
p_{H2O}	5.7 torr	11.0 torr
p_{H2O2}	0.21 torr	0.45 torr
x_{H2O}	0.76 %	1.44 %
x_{H2O2}	273 ppm	592 ppm

As can be seen, the vapor pressures are highly sensitive to temperature, with the mole fractions of both water and hydrogen peroxide roughly doubling at a temperature increase from 10°C to 20°C. This is an important detail because we only measure the bath temperature. We assume that the liquid-vapor boundary is at this same temperature, but this is not guaranteed since the top half of the bubbler is not completely submerged, potentially allowing the vapor to heat up significantly above the bath temperature of 10°C. Moreover, for the higher flow rates (up to 5 slm), the residence time in the bubbler may be too small for the gas to equilibrate with the temperature of the hydrogen peroxide solution.

To improve the accuracy of the concentration estimates, FTIR-absorption spectroscopy was employed to directly measure the H_2O and H_2O_2 concentrations. The gas mixture was sampled by flowing the gas through a 12 cm cell with KBr windows, placed in the N_2 purged sample compartment of an FTIR spectrometer. The gas was sampled in two positions; In one of the positions, the exit of the jet was immediately let into the FTIR absorption cell (off-line). In the other position, the absorption cell was placed in line with the exhaust line of the cell (between the pump and experimental cell). The measured absorption spectra at both positions are shown in Figure 6.3.

Concentrations were obtained by fitting the absorption spectra with a synthetic spectrum based on the HITRAN line database for H_2O and H_2O_2. The fitted H_2O_2 mole fractions are as follows: $x_{cell\ exhaust}^{H2O2} = 0.045\%$ and $x_{jet\ exit}^{H2O2} = 0.050\%$. The mole fraction of water does not differ between the two positions and is determined to be: $x_{cell\ exhaust}^{H2O} = x_{jet\ exit}^{H2O} = 0.43\%$.
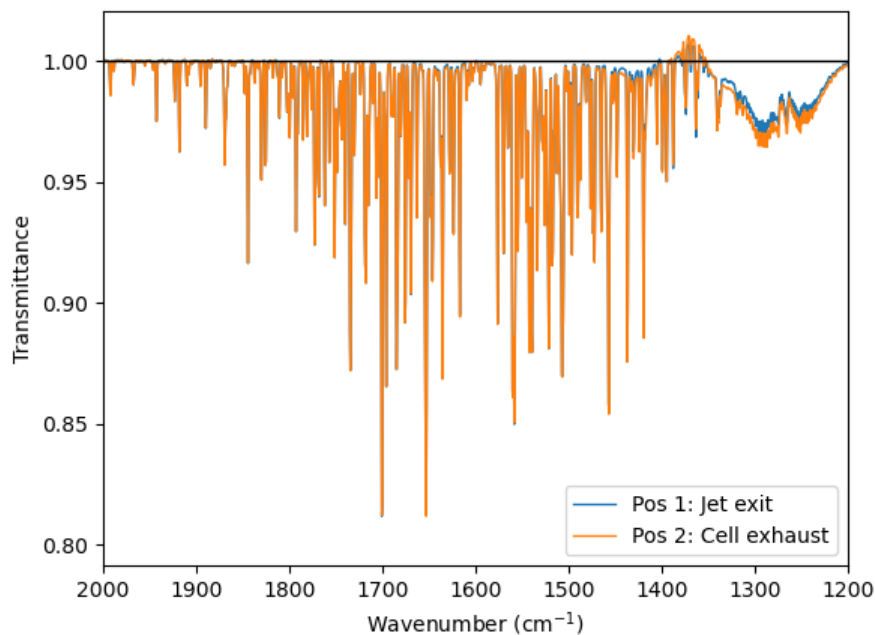
Figure 6.3 Absorption spectra at the two different locations

The measured H_2O_2 fractions are consistent with predictions at 293K (20°C), but measured water fractions are significantly lower than predicted values at 283K (10°C), the controlled bath temperature.

The difference in measured H_2O_2 concentration between positions 1 and 2 suggests that H_2O_2 reacts away somewhere in the system. Because it is hard to say where this happens exactly, it would be more robust to measure the density in-situ. To this extent, the H_2O_2 density is also measured by UV-absorption of the 213nm laser. After the 213nm beam passes the experimentation cell once, it is reflected to double the absorption path length. The laser intensity is monitored before entering the cell and after passing the cell twice by photo-diodes that are verified to operate in a linear regime. Diffusers in front of the PDs mitigate the effect of spatial fluctuations. The ratio of the intensities between the

146

two beams is used to calculate the transmission, which is then used to calculate hydrogen peroxide concentration via Beer's Law.

The obtained mole fractions were 550, 561, and 566 ppm H_2O_2, which is reasonably close to the values obtained by FTIR absorption. Both the values obtained by IR- and UV absorption are close to the estimated values for 293.14 K but much higher than those estimated for 283.14 K, the bath temperature of the bubblers. This could indicate that the H_2O_2 vapor present in the cell originates from H_2O_2 condensed in the lines, where the temperature is closer to 293K.

6.7 ABSOLUTE CALIBRATION FOR OH

Absolute calibration of the OH-LIF images is done in two steps. At first, the LIF signal is normalized by fluorescence from acetone to correct for the distribution in the laser intensity (flat-field correction). The normalized LIF-signal is multiplied by a scalar calibration constant C_{cal} to reflect absolute OH densities: $x_{OH} = \frac{I_{LIF}}{I_{LIF}^{ace}} C_{cal}$. The second step of the absolute calibration procedure is to determine the value of C_{cal}, which can be found by measuring the LIF signal of a known quantity of OH.

Absolute OH-densities are inferred from the decay time constants of ground-state OH, similar to [167]. Instead of measuring OH-decay traces in the plasma, however, we used photo-fragmentation of H_2O_2, which provides a relatively clean system where the majority reactive species, H_2O and H_2O_2, can be quantified through IR- and UV absorption spectroscopy respectively. This leaves only one unknown impacting the OH-decay rate, namely the OH-concentration, which can be solved for.
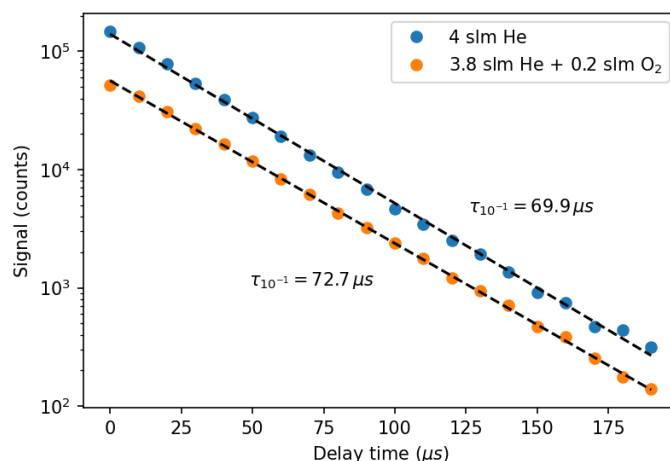
Figure 6.4 Temporal LIF signal decay for the two flow mixtures

The OH-decay trace (or decay time constant) is measured by recording LIF-images while stepwise increasing the delay time between the 213nm and 282nm laser, starting at a delay of 50ns and increasing in steps of 10us. Each of the LIF-images is first normalized by the laser profile and consequently averaged over a uniform region. This averaged LIF signal is plotted for varying delay times in Figure 6.4 with a logarithmic vertical scale. The straight line in Figure 4 suggests that the decay is close to singly exponential decay, which contrasts the observed quadratic behavior (in semilog-y) observed by [167]. The reason for this discrepancy is that in our case the H_2O_2 concentration is significantly higher, which promotes the $H_2O_2 + OH \rightarrow H_2O + HO_2$ relative to the $OH + OH \rightarrow H_2O + O$ reaction that causes the quadratic dependency. The vertical offset between the pure He and O_2 admixed traces is due to the difference in fluorescence yield.

The decay traces are fitted with a singly exponential function: $y = y_0 10^{-t/\tau}$, which yields the averaged LIF-signal y_0 at $t = 0$ and the (decadal) decay time constant τ of the decay trace.

The mole fraction of water and hydrogen peroxide were used as inputs in a Chemkin calculation to simulate the OH decay. The OH concentration was a free parameter that was varied to match the experimentally observed decay.
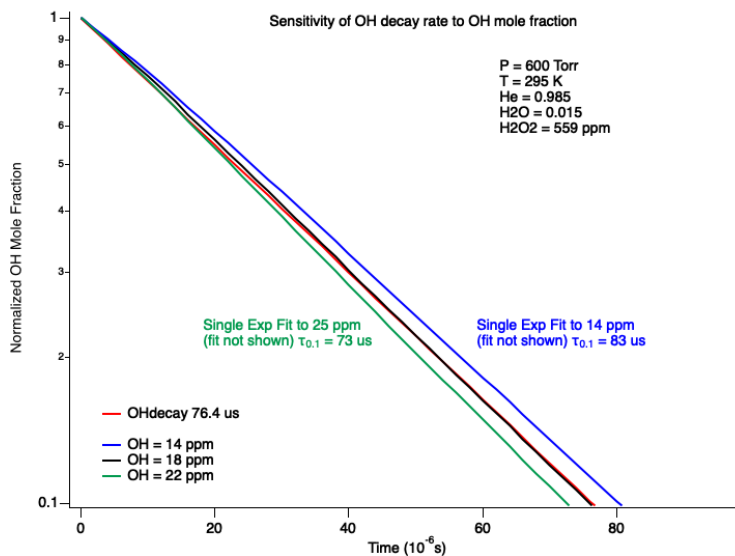
Figure 6.5 Sensitivity of OH decay rate to OH mole fraction

Figure 6.5 shows OH decay simulated in ChemKin, based on the measured 559 ppm H_2O_2 as an input value. The OH-decay is insensitive to the water concentration. The OH number density was varied until the initial slope of the simulated OH decay approximately matched the slope of the measured decay for a single exponential with $\tau = 76.4$ us, which came out $x_{OH}^{cal} = 14$ ppm.

When the H_2O_2 is decreased to 300ppm, the OH needs to be increased to 50 ppm to match the initial OH decay rate. However, at 50 ppm the decay is no longer single exponential because now OH + OH reactions dominate. This lends additional credence to the measured H_2O_2 values of ~600 ppm.

Now, the calibration constant can be calculated as follows: $C_{cal} = x_{OH}^{cal}/y_0$, where x_{OH}^{cal} is the OH mole fraction obtained from the Chemkin simulations, and y_0 is the averaged LIF signal obtained from fitting the experimental decay curve.

6.8 LINEARITY VERIFICATION

If the excitation laser energy is too high, partial or even complete saturation of the LIF transition could occur, at which point the LIF signal intensity doesn't scale linearly with the laser energy anymore. The calibration procedure of the H_2O_2 is insensitive to (partial) saturation because the LIF signals of the experiment $\boldsymbol{I}_{LIF}$ and reference $\boldsymbol{I}_{LIF}^{ace}$ have the same degree of saturation which divides out when taking the ratio. In the OH calibration, the OH-LIF signal is divided by the LIF signal from acetone, which likely has different degrees of saturation while operating outside of the linear regime.

The linearity of the OH-LIF was investigated by measuring the LIF intensity as a function of excitation laser energy, Figure 6.6. The energy was scanned by rotating a half-lambda waveplate, which in conjunction with a polarizing beamsplitter cube comprises a variable attenuator. The laser energy was measured by a photodiode which was confirmed to have a linear response to the beam energy and was calibrated by comparing the diode signal to a laser power meter.
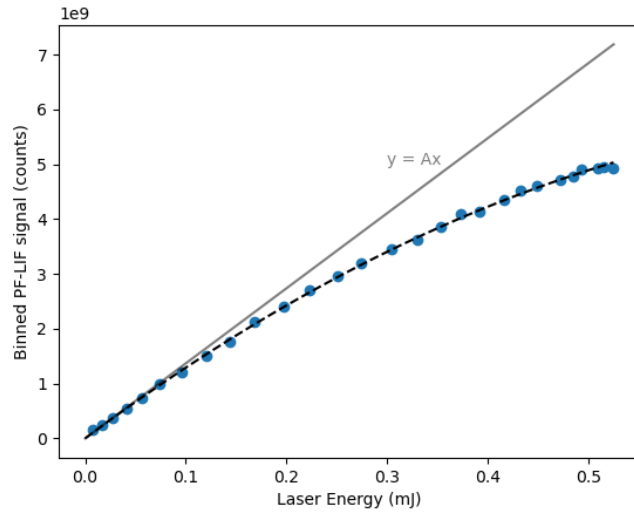
Figure 6.6 PF-LIF signal dependence on laser energy

A partially saturated LIF transition can cause artifacts at the edges, where laser energy is lower, and the transition is less saturated. Because the acetone-LIF used to image the laser intensity distribution is in the linear regime, this may cause the normalized signal in the edges to appear higher than it is. To test how strong this effect is, LIF images were taken at 100%, 50%, and 25% of the laser energy. Ratios of 50/100 and 25/100 are shown in Figure 6.7.
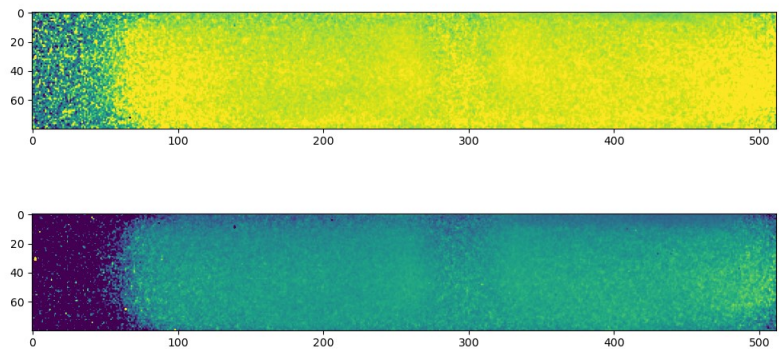
Figure 6.7 LIF signals at 50% and 25% ratio

By binning over the horizontal axis, the profiles can be compared directly:

(a)   **(b)**
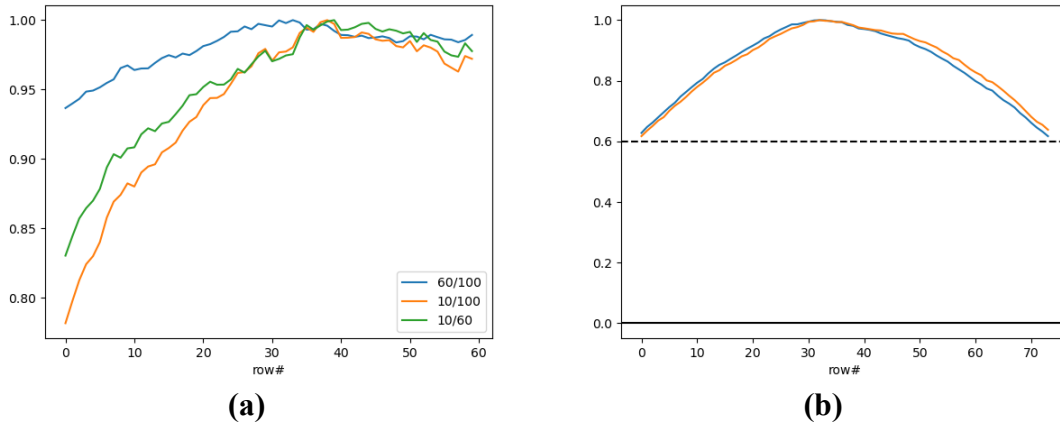
Figure 6.8 Different LIF ratios binned horizontally

It is seen that as long as the intensity doesn't drop below 60% of the maximum energy, the worst overestimation of the OH concentration as a result of saturation is 5%, Figure 6.8a. This rule was used to determine the valid window of our data; this window is defined by those rows where the laser intensity drops to no lower than 60%, Figure 6.8b. Note that the plots we use for this determination drop in signal near the edges due to the laser profile, but also due to vignetting; The rule just described is therefore conservative since a measured drop of 60%, in reality, means a drop of *at most* 60%.

We find that the yield ratio between the pure He and He + 5% O_2 admixture is $Y\_O_2/Y\_He = 58.3\%$. This number is used to apply the calibration measured in pure He to experiments recorded in the admixed O_2 case.

6.9 RESULTS

6.9.1 GAS TEMPERATURE

Fluorescence spectra were recorded of OH-LIF in the plasma for a series of time delays. The spectra were fit with a routine based on interpolating LIFBASE spectra in a range of preset temperatures ($\Delta T=50K$). All fitted temperatures fell in the range of 275 K-300 K. Figure 6.9 shows the measured fluorescence spectra and a synthetic spectrum at T=300 K. We used an A-X(1,0) excitation scheme, so most observed emissions, 94.5%, originated from the (1,1) transition, with the remainder coming from the (0,0) transition (not shown in the figure). Fluorescence from the PF-LIF from seeded H_2O_2 yielded very similar rotational temperatures and vibrational fractions, with no indication of higher vibrational levels being populated. This suggests that the OH produced by the photo-fragmentation process is in not in some hot nascent distribution but is instead fully equilibrated with the surroundings. From the fluorescence spectroscopy, we resolve that the temperature of the gas in the afterglow is ~300 K.
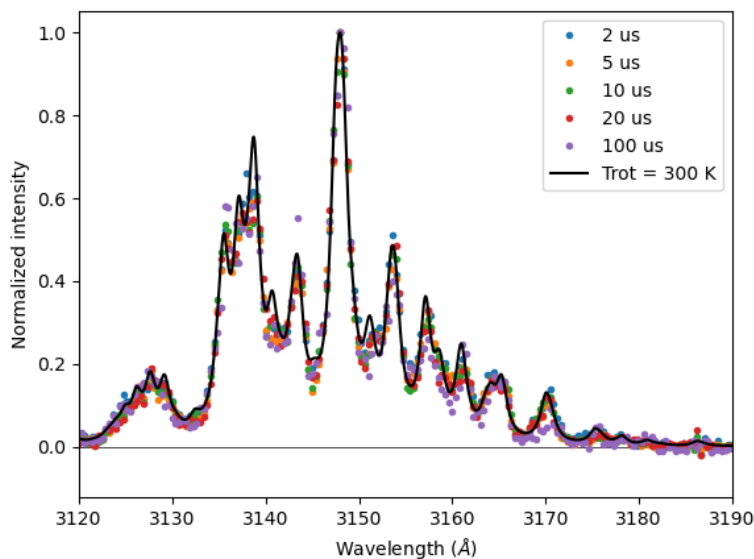
Figure 6.9 Fluorescence spectrum

6.9.2 PLASMA EMISSION

As mentioned previously, the HV pulsar was operated in burst mode of 5 and 10 pulses per burst. The bursts are delivered in the first 0.1 ms (burst duration) of a 20 ms pulse duration. For the 5 burst/pulses mode, the optical emission for each of the successive pulse is shown sequentially in Figure 6.10. The emission is shown for a gate width of 50 ns capturing each burst.

Burst#	He-H$_2$O	He-O$_2$-H$_2$O
1		
2		
3		
4		
5		
	(a)	(b)
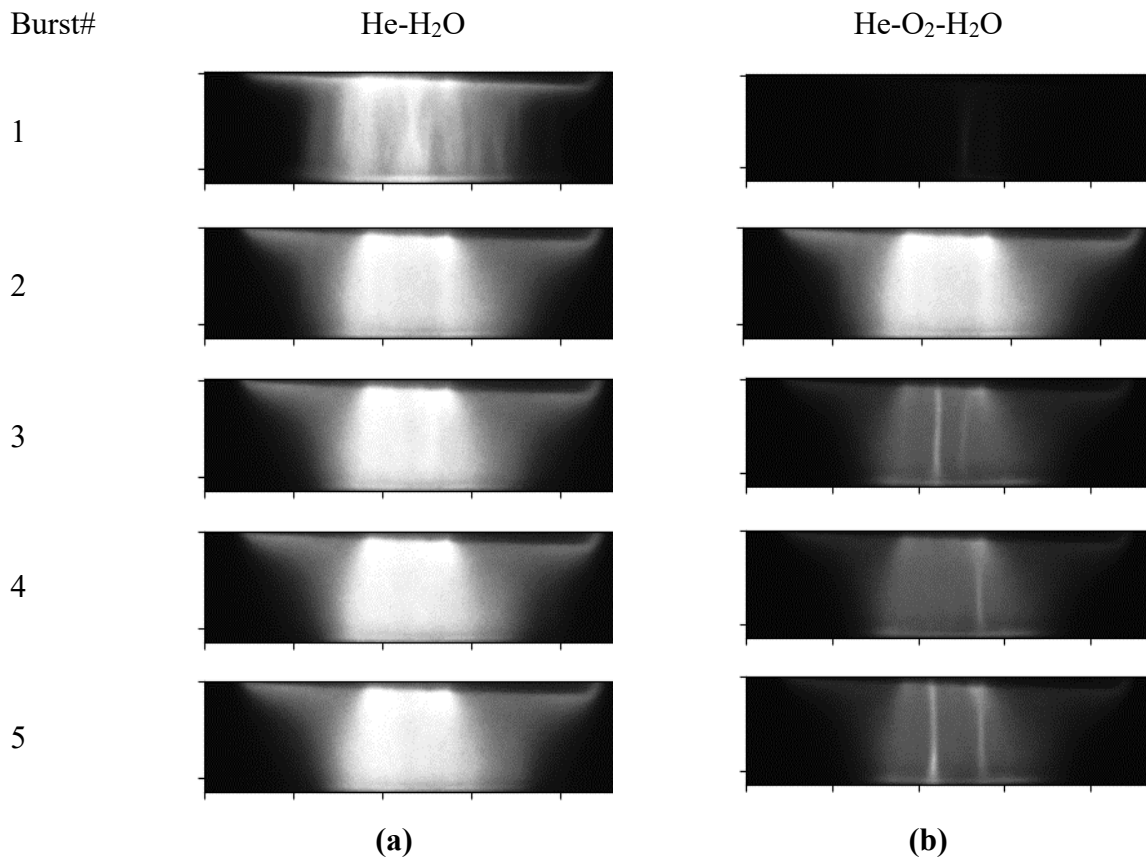
Figure 6.10 DBD emission in pure He-H$_2$O mixture and (He+5%O$_2$)-H$_2$O

Figure 6.10a shows the emission of H$_2$O in He only. For DBD discharge in both gas mixtures, it is observed that the first pulse is greatly filamentary. For DBD in He-H$_2$O, multiple filaments were present on the first burst but in the successive bursts, the discharge acquired the appearance of a uniform glow mode, and the filaments were no longer

154

perceptible. Figure 6.10b shows the emission of H_2O in He, containing a 5% admixture of O_2. A single filament is slightly visible on the first pulse. For successive bursts, a more glow-like appearance is observed with 1 or 2 filaments.

The changes in plasma morphology can be explained by charge deposition on the dielectric. After the first burst, there could still be residual charges on the dielectric before the next pulse is initiated, hence facilitating the discharge in the next burst. The more filamentary nature of He-O_2-H_2O discharge could be energy losses from additional reaction pathways, due to the quenching kinetics of the added O_2.

6.9.3 STUDY OF PFLIF AND LIF

A simple qualitative simulation of the stagnation flow field for a similar geometry and flow configuration is done in COMSOL Multiphysics version 5.3a [94] and shown in **Figure 6.11**. The LIF and PFLIF images showing absolute densities of OH and H_2O_2 are shown in Figure 6.12 for 10 bursts/pulse mode. Both active species: OH, and H_2O_2 adopts the flow-field of the stagnation plane as shown in the simulated slow-field, **Figure 6.11**. The discharge region can be subdivided into three major sections based on the density of the active species. The first section is the central core, in which, negligible discharge species are produced and are dominated by gas flow; this is denoted by the blue central core in almost every image in Figure 6.12. The second section is the periphery around the central core in which, the production of the largest amount of both the discharge species occurs; this is denoted by the reddish/whitish section in the top right image in Figure 6.12. The rest of the discharge volume outside these zones seems to be mostly dominated by convection and diffusion; this is denoted by the greenish/bluish regions in the top right image in Figure 6.12.

The discharge morphology can be explained by the qualitative flow-field distribution, **Figure 6.11**. In the central channel and close to the ground plate, the velocity vectors are of the highest magnitude. In the initial times, both OH and H_2O_2 are highly concentrated in these regions as well, Figure 6.12. As time progresses, it is seen that the concentration of the discharge species tends to decrease close to the ground electrode and tends to increase more towards the upper surface of the discharge volume. This may be explained by the diffusion and recirculation velocity vectors as in **Figure 6.11**. With greater time delays, the active species are lost due to convection and reaction losses as well. The temporally resolved images from 1 to 10 ms show that with time, the central core widens i.e., the discharge species are conveyed more and more out from the central zones to the periphery.
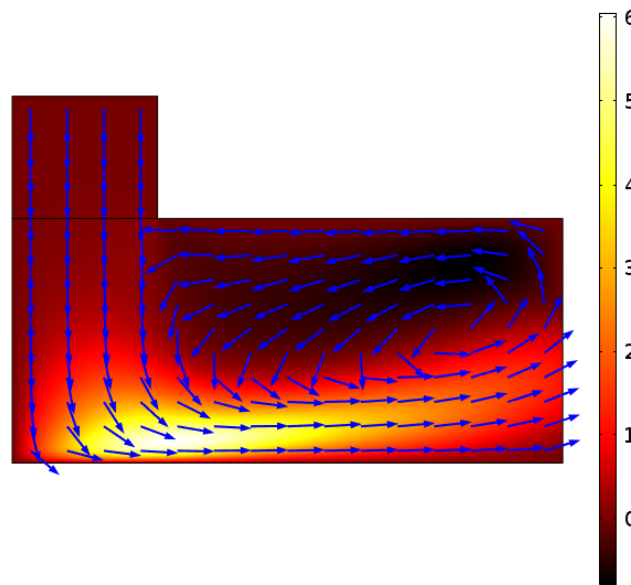
Figure 6.11 Qualitative flow field of He in a stagnation plane of similar configuration (colormap in m/s)

Time (ms)	Number density of OH (ppm)	Number density of H₂O₂ (ppm)
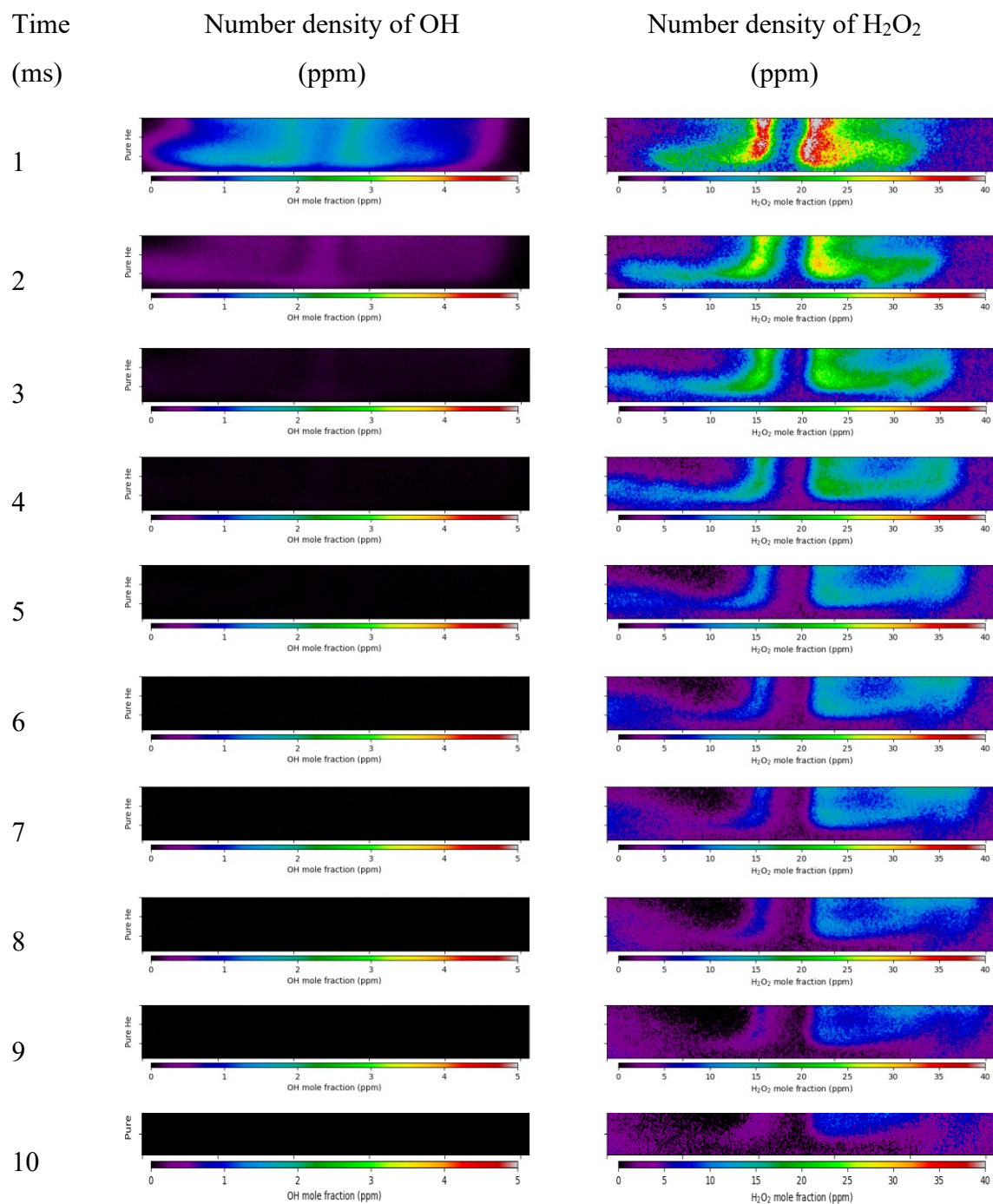
Figure 6.12 PLIF images of H₂O and H₂O₂ in the afterglow of DBD for water vapor in helium with no admixture as discharge medium

It is further observed from Figure 6.12 that the OH density almost becomes undetectable after 2.5 ms, whereas ~ 7-10 ppm of H_2O_2 was still present after 10 ms. Thus, it is observed that the H_2O_2 residence time is longer than that of OH. For the mode with 5 bursts/pulse, the OH density attains the same degree of non-detection at 0.5 ms earlier (not shown here), thus, doubling the burst rate increases the OH residence time. However, in the case of H_2O_2, the effect of doubling the burst rate did not noticeably affect its final concentration at the end of the pulse. The faster decay time of OH radicals can be attributed to the OH being an active radical whereas H_2O_2 is a relatively stable molecule. Furthermore, one of the formation routes of H_2O_2 is the recombination of OH radicals, which also explains why H_2O_2 possesses a longer residence time while OH decays faster.

LIF and PLIF images showing the absolute density of OH and H_2O_2 for an admixture of 5% O_2 to He-H_2O mixture are shown in Figure 6.13. The plasma morphology is almost the same as shown in Figure 6.12. The temporally resolved images still show the widening of the central core and the decrease in the greenish hue in the right images in Figure 6.13 mean that convection and diffusion losses are also dominant along with kinetic loss mechanisms.

The most noticeable change is seen in the case of H_2O_2 density. For the case with 5% O_2 admixture, the $n(H_2O_2)$ is almost twice of that the case without O_2 admixture. In the case of $n(OH)$, the observations are not as straightforward. Until 2.5 ms, the $n(OH)$ is lesser in the case with O_2 admixture than without. However, after 2.5 ms, $n(OH)$ in the case with O_2 admixture steadies at ~ 0.5 ppm, whereas, in the case without admixture, $n(OH)$ almost decays completely.

Time (ms)	Number density of OH (ppm)	Number density of H₂O₂ (ppm)
1 ms		
2 ms		
3 ms		
4 ms		
5 ms		
6 ms		
7 ms		
8 ms		
9 ms		
10 ms		
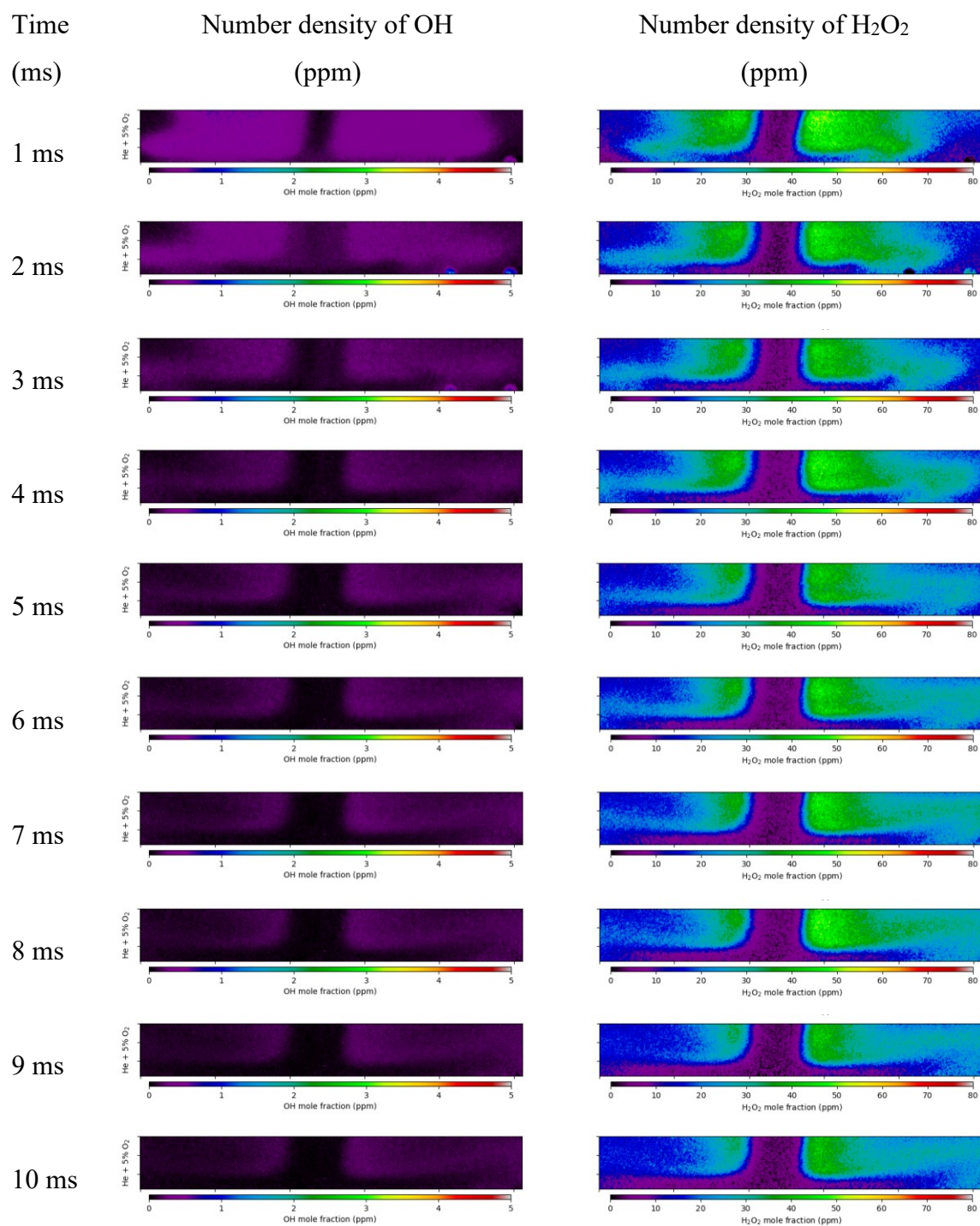
Figure 6.13 PLIF images of H₂O and H₂O₂ in the afterglow of DBD for water vapor in helium with 5% O₂ as admixture as discharge medium

Deducing the kinetics behind these observations is beyond the scope of this dissertation. However, it could be said that the decrease in n(OH) for the first 2.5 ms for the case with 5% O_2 admixture is due to the quenching effect of the added O_2 molecules. The subsequent increase in n(OH) and n(H_2O_2) with admixture is due to the presence of ●O radicals from discharge in O_2. The heavy particle reactions between ●O and H_2O molecules provide additional reaction channels for the formation of OH and H_2O_2.

6.10 CONCLUSION

Planar laser-induced fluorescence (PLIF) of OH and photofragmentation planar laser-induced fluorescence (PF-PLIF) of H_2O_2 were resolved both spatially and temporally in a dielectric barrier discharge (DBD) of highly concentrated He-H_2O mixture. Spectrally resolved fluorescence spectrum of OH(A-X)(1,0) excitation scheme showed that the discharge temperature was ~300 K. Two modes of power were investigated. It was observed that for the lower voltage bursts, OH had a residence time of 2 ms, whereas H_2O_2 had a prolonged existence well over 10 ms. With doubling pulse voltage burst rate, OH residence time increased by ~ 0.5 ms, whereas the residence time or final number density of H_2O_2 was mostly unchanged. The prolonged residence time of H_2O_2 was attributed to the OH recombination reaction and higher relative stability of H_2O_2 molecules compared to OH radicals. Experiments were also repeated with 5% O_2 as admixture. The results showed that until 2.5 ms, the OH density was lesser in the case with O_2 admixture, which might be due to the quenching effect of O_2. In the latter case (with O_2 admixture), the presence of OH persisted well beyond 10 ms and for the same time delays, the H_2O_2 density was almost doubled. Since this phenomenon is observed in the afterglow it might be reasonable to suppose that such kinetics involves heavy particle reactions including charge

transfer, recombination, and dissociative recombination reactions involving •O radicals, H_2O, H_2O^+ and •OH. This lends credence to the fact that in DBD plasma, the density of the active species: OH, and H_2O_2 in the afterglow is highly dependent on heavy particle interactions in the afterglow, which can have an as significant impact as electron-impact reactions during breakdown initiation.

In the future, the experiments could be repeated for varying water concentrations using another He has inlet stream to mix with the humid He to form mixtures with varying humidity. This could lend further insight if the OH and H_2O_2 production depend more on the water vapor concentration or the discharge power. A 248 nm laser could also be used instead of 213 nm. A 248 nm laser induces fluorescence in H_2O vapor as well as photofragments H_2O_2. Thus, the concertation of H_2O_2 vapor could be measured in situ.

6.11 REFERENCES

23.   Kanazawa, S., H. Tanaka, A. Kajiwara, T. Ohkubo, Y. Nomoto, M. Kocik, J. Mizeraczyk, and J.-S. Chang, *LIF imaging of OH radicals in DC positive streamer coronas.* Thin Solid Films, 2007. **515**(9): p. 4266-4271.

24.   Ono, R. and T. Oda, *Measurement of gas temperature and OH density in the afterglow of pulsed positive corona discharge.* Journal of Physics D: Applied Physics, 2008. **41**(3): p. 035204.

25.   Ono, R. and T. Oda, *OH radical measurement in a pulsed arc discharge plasma observed by a LIF method.* IEEE Transactions on Industry applications, 2001. **37**(3): p. 709-714.

27.   Bruggeman, P., G. Cunge, N.J.P.S.S. Sadeghi, and Technology, *Absolute OH density measurements by broadband UV absorption in diffuse atmospheric-pressure He–H2O RF glow discharges.* 2012. **21**(3): p. 035019.

29.   Du, Y., G. Nayak, G. Oinuma, Z. Peng, and P.J. Bruggeman, *Effect of water vapor on plasma morphology, OH and H2O2 production in He and Ar atmospheric pressure dielectric barrier discharges.* Journal of Physics D: Applied Physics, 2017. **50**(14): p. 145201.

30.   Verreycken, T., N. Sadeghi, and P.J. Bruggeman, *Time-resolved absolute OH density of a nanosecond pulsed discharge in atmospheric pressure He–H2O: absolute calibration, collisional quenching and the importance of charged species in OH production.* Plasma Sources Science and Technology, 2014. **23**(4): p. 045005.

31.   Verreycken, T., R. Van der Horst, A. Baede, E. Van Veldhuizen, and P. Bruggeman, *Time and spatially resolved LIF of OH in a plasma filament in atmospheric pressure He–H2O.* Journal of Physics D: Applied Physics, 2012. **45**(4): p. 045205.

33.   Verreycken, T., R. Van Der Horst, N. Sadeghi, and P. Bruggeman, *Absolute calibration of OH density in a nanosecond pulsed plasma filament in atmospheric pressure He–H2O: comparison of independent calibration methods.* Journal of Physics D: Applied Physics, 2013. **46**(46): p. 464004.

94.   *COMSOL Multiphysics*, in *Multiphysics Reference Guide for COMSOL 5.5*. 2019: Burlington, MA, USA.

134.   Kalghatgi, S., C.M. Kelly, E. Cerchar, B. Torabi, O. Alekseev, A. Fridman, G. Friedman, and J. Azizkhan-Clifford, *Effects of non-thermal plasma on mammalian cells.* PloS one, 2011. **6**(1): p. e16270.

157.   Ceriani, E., E. Marotta, V. Shapoval, G. Favaro, and C. Paradisi, *Complete mineralization of organic pollutants in water by treatment with air non-thermal plasma.* Chemical Engineering Journal, 2018. **337**: p. 567-575.

158.   Ma, R., G. Wang, Y. Tian, K. Wang, J. Zhang, and J. Fang, *Non-thermal plasma-activated water inactivation of food-borne pathogen on fresh produce.* Journal of hazardous materials, 2015. **300**: p. 643-651.

159.   Penetrante, B., M. Hsiao, J. Bardsley, B. Merritt, G. Vogtlin, A. Kuthi, C. Burkhart, and J. Bayless, *Identification of mechanisms for decomposition of air pollutants by non-thermal plasma processing.* Plasma sources science and technology, 1997. **6**(3): p. 251.

160.	Baik, K.Y., H.L. Kang, J. Kim, S.Y. Park, J.Y. Bang, H.S. Uhm, E.H. Choi, and G. Cho, *Non-thermal plasma jet without electrical shock for biomedical applications.* Applied Physics Letters, 2013. **103**(16): p. 164101.

161.	Kim, Y.H., Y.J. Hong, K.Y. Baik, G.C. Kwon, J.J. Choi, G.S. Cho, H.S. Uhm, D.Y. Kim, and E.H. Choi, *Measurement of reactive hydroxyl radical species inside the biosolutions during non-thermal atmospheric pressure plasma jet bombardment onto the solution.* Plasma Chemistry and Plasma Processing, 2014. **34**(3): p. 457-472.

162.	Karuppiah, J., E.L. Reddy, P.M.K. Reddy, B. Ramaraju, R. Karvembu, and C. Subrahmanyam, *Abatement of mixture of volatile organic compounds (VOCs) in a catalytic non-thermal plasma reactor.* Journal of hazardous materials, 2012. **237**: p. 283-289.

163.	Magureanu, M., N.B. Mandache, and V.I. Parvulescu, *Degradation of pharmaceutical compounds in water by non-thermal plasma treatment.* Water research, 2015. **81**: p. 124-136.

164.	Vandenbroucke, A.M., R. Morent, N. De Geyter, and C. Leys, *Non-thermal plasmas for non-catalytic and catalytic VOC abatement.* Journal of hazardous materials, 2011. **195**: p. 30-54.

165.	Verreycken, T. and P.J. Bruggeman, *OH density measurements in nanosecond pulsed discharges in atmospheric pressure N2–H2O mixtures.* Plasma Sources Science and Technology, 2014. **23**(1): p. 015009.

166.   Bruggeman, P., D. Schram, M.Á. González, R. Rego, M.G. Kong, C.J.P.S.S. Leys, and Technology, *Characterization of a direct dc-excited discharge in water by optical emission spectroscopy.* 2009. **18**(2): p. 025017.

167.   Dilecce, G., P. Ambrico, M. Simek, and S. De Benedictis, *LIF diagnostics of hydroxyl radical in atmospheric pressure He-H2O dielectric barrier discharges.* Chemical physics, 2012. **398**: p. 142-147.

168.   Larsson, K., *Development of photofragmentation-based diagnostics.* 2018: Division of Combustion Physics, Department of Physics, Lund University.

169.   Larsson, K., O. Johansson, M. Aldén, and J. Bood, *Simultaneous visualization of water and hydrogen peroxide vapor using two-photon laser-induced fluorescence and photofragmentation laser-induced fluorescence.* Applied Spectroscopy, 2014. **68**(12): p. 1333-1341.

170.   Johansson, O., J. Bood, M. Aldén, and U. Lindblad, *Detection of hydrogen peroxide using photofragmentation laser-induced fluorescence.* Applied spectroscopy, 2008. **62**(1): p. 66-72.

171.   Li, B., M. Jonsson, M. Algotsson, J. Bood, Z. Li, O. Johansson, M. Aldén, M. Tunér, and B. Johansson, *Quantitative detection of hydrogen peroxide in an HCCI engine using photofragmentation laser-induced fluorescence.* Proceedings of the Combustion Institute, 2013. **34**(2): p. 3573-3581.

172.   Luque, J. and D.R. Crosley, *LIFBASE: Database and spectral simulation program (version 1.5).* SRI international report MP, 1999. **99**(009).

173.	Aul, C.J., M.W. Crofton, J.D. Mertens, and E.L. Petersen, *A diagnostic for measuring H2O2 concentration in a shock tube using tunable laser absorption near 7.8 μm.* Proceedings of the Combustion Institute, 2011. **33**(1): p. 709-716.

CHAPTER 7 :

CONCLUDING REMARKS AND FUTURE RESEARCH DIRECTION

7.1 PREFACE TO CONCLUSION

The primary goal of this dissertation was to fundamentally characterize plasma discharge in pure water vapor. To that extent, low pressure dc glow discharge in water vapor was characterized using multiple operating parameters: length of discharge path, pressure and discharge current. A dielectric barrier discharge system employing He-H_2O discharge medium at high H_2O concentration was studied at different power densities to characterize active species produced in the discharge, namely, OH and H_2O_2. According to the basis of known literature, using photofragmentation laser-induced fluorescence to measure in situ direct production of H_2O_2 in a plasma that has been presented in this dissertation is a pioneering attempt. Using the findings from the characterization, two applications were developed. The first application can evaluate dryness using the emissions from plasma dissociation of water vapor. The second application uses the principle of DBD in the air-H_2O discharge medium to create active species that can help in the disinfection mechanism. Concurrently, the 1-d dc discharge model of N_2 is developed with the goal to discern water vapor kinetics in dc discharge that can affect the stratification of the positive column.

7.2 MAJOR FINDINGS

An extensive understanding of the plasma characterization including species density and discharge characteristics is necessary for high fidelity modeling of the discharge. In this dissertation, two different active species were spatially resolved, namely OH(A-X) and H_α with the most dominant emission signals originating from plasma dissociation of H_2O. It was also observed that OH(A-X) emission was the most intense at the anode and have some presence in the positive column, whereas H_α transition is the most

intense at the cathode and had an almost undetectable presence in the positive column. This is potentially due to lower electron temperature (T_e) at the positive column that can only sustain OH(A-X) of the two transitions that were studied. Since the anode sheath possesses lower T_e than the cathode sheath, the higher intensity of OH(A-X) at the cathode sheath can also be termed due to larger cross-sections of OH(A-X) transitions at lower T_e and vice versa. Two fundamental properties, namely normal current density (j_n) and normal cathode potential (V_n) are deduced for the water vapor plasma for stainless steel electrodes. Both j_n and V_n dictate conditions for maintaining stable normal glow discharge as well as discerning the size of the cathode spot.

Dielectric barrier discharge plasma in water vapor in pseudo atmospheric helium produced both OH and H_2O_2, both of which were detected with laser-induced fluorescence and photofragmentation laser-induced fluorescence, respectively. H_2O_2 was measured with direct calibration with an H_2O_2-He mixture of known concentration, whereas OH was measured using a chemical model to fit the OH decay trace in the afterglow. It was also shown that the addition of O_2 increased the concentration of both OH and H_2O_2, however, in the case of OH, there is time-varying kinetics introduced in the afterglow that requires careful deduction.

Even though evaluating the quenching effect of H_2O kinetics on dc discharge in air at moderately low pressures remained outside the bounds of this dissertation, a fluid model with detailed electronic, vibrational, and heavy particle interactions are created to model striations in a dc glow discharge in N_2 gas. There has been no known literature in which, striations have been modeled for a purely diatomic gas. The role of the vibrational excitation kinetics in the forming of these striations is found to be very crucial both in terms

169

of vibrational energy as well as in terms of wave-perturbation analysis. It is also noticed that electron energy transfer due to mass density gradient also satisfies the instability criterion in the discharge regime studied.

7.3 FUTURE DIRECTIONS FOR PROGRESS

Even though this dissertation attempted to answer most of the challenges that it addressed, there are significant data validation and reasoning that could be further explored as independent research topics.

The dc characterization of plasma in pure H_2O could be further extended to incorporate electron number density measurement from the profile of H_α. Even though the profile of H_β is commonly used by researchers since it does not require corrections due to molecular interactions, the $H\alpha$ profile is also used in cases when the emission intensity of H_β is very low.

For DBD discharge in the He-H_2O mixture, the characterization of the active species was accomplished for the maximum attainable humidity in He at operating temperature. Several research attempts in the past had performed parametric studies for varying concentrations of humidity in noble gas mixtures and in some cases, it was reported that OH production was more affected by the humidity content than by power density. But such cases for H_2O_2 parametric evaluation are very scarce in the case of nonthermal plasma discharge. With the PFLIF technique that has been developed for measurements in plasma in this dissertation, these parametric studies can be accomplished. The photofragmentation laser used in the experiment is 213 nm. It had been reported in the literature that a 248 nm laser can accomplish the same photofragmentation as well as induce a broadband

fluorescence from H_2O, which can be calibrated to attain a concentration of H_2O in the discharge after plasma dissociation.

The OES device for evaluating dryness can be recalibrated to measure dryness in air-H_2O mixtures as well. Its potential to be used as a flowmeter for H_2O is an exciting topic to be addressed. For the DBD application that used air-H_2O as a discharge medium, the areas of application could be extended to evaluate treatment effectiveness on bio-organisms on different surfaces. For the current application, only two strains of bacteria were studied. The study could be further extended to treat more resilient bacterial and viral strains, notably, the strains of coronavirus that could extend the application of this instrument to medical facilities.

BIBLIOGRAPHY

1. Fridman, A. and L.A. Kennedy, *Plasma physics and engineering*. 2004: CRC press.

2. Staack, D.A., *Characterization and stabilization of atmospheric pressure DC microplasmas and their application to thin film deposition.* 2009.

3. Vanraes, P. and A. Bogaerts, *Plasma physics of liquids—A focused review.* Applied Physics Reviews, 2018. **5**(3): p. 031103.

4. Bruggeman, P., M.J. Kushner, B.R. Locke, J.G. Gardeniers, W. Graham, D.B. Graves, R. Hofman-Caris, D. Maric, J.P. Reid, and E. Ceriani, *Plasma–liquid interactions: a review and roadmap.* Plasma sources science and technology, 2016. **25**(5): p. 053002.

5. Zhou, L. and Y. Jiang, *Recent progress in dielectric nanocomposites.* Materials Science and Technology, 2020. **36**(1): p. 1-16.

6. Bruggeman, P., D. Schram, M.Á. González, R. Rego, M.G. Kong, and C. Leys, *Characterization of a direct dc-excited discharge in water by optical emission spectroscopy.* Plasma Sources Science and Technology, 2009. **18**(2): p. 025017.

7. Fortov, V., I. Iakubov, and A. Khrapak, *Physics of strongly coupled plasma*. Vol. 135. 2006: OUP Oxford.

8. Boates, B. and S.A. Bonev, *Electronic and structural properties of dense liquid and amorphous nitrogen.* Physical Review B, 2011. **83**(17): p. 174114.

9. Martinez-Vega, J., *Dielectric materials for electrical engineering*. 2013: John Wiley & Sons.

10. Vanraes, P., A. Nikiforov, A. Bogaerts, and C. Leys, *Study of an AC dielectric barrier single micro-discharge filament over a water film.* Scientific reports, 2018. **8**(1): p. 1-11.

11.   Setsuhara, Y., *Low-temperature atmospheric-pressure plasma sources for plasma medicine.* Archives of biochemistry and biophysics, 2016. **605**: p. 3-10.

12.   Miralai, S., E. Monette, R. Bartnikas, G. Czeremuszkin, M. Latreche, and M. Wertheimer, *Electrical and optical diagnostics of dielectric barrier discharges (DBD) in He and N2 for polymer treatment.* Plasmas and Polymers, 2000. **5**(2): p. 63-77.

13.   Li, X., D. Niu, P. Jia, N. Zhao, and N. Yuan, *Investigation on the Micro-Discharge Characteristics of Dielectric Barrier Discharge in a Needle-Plate Geometry.* Plasma Science and Technology, 2011. **13**(2): p. 213.

14.   Cserfalvi, T. and P. Mezei, *Operating mechanism of the electrolyte cathode atmospheric glow discharge.* Fresenius' journal of analytical chemistry, 1996. **355**(7): p. 813-819.

15.   Gaisin, A.F. and E.E.e. Son, *Vapor-air discharges between electrolytic cathode and metal anode at atmospheric pressure.* High temperature, 2005. **43**(1): p. 1-7.

16.   Baba, K., T. Kaneko, and R. Hatakeyama, *Ion irradiation effects on ionic liquids interfaced with rf discharge plasmas.* Applied physics letters, 2007. **90**(20): p. 201501.

17.   Yamamoto, Y.-i., Y.-I. Suzuki, G. Tomasello, T. Horio, S. Karashima, R. Mitríc, and T. Suzuki, *Time-and angle-resolved photoemission spectroscopy of hydrated electrons near a liquid water surface.* Physical review letters, 2014. **112**(18): p. 187603.

18.   Verhaart, H. and P. Van der Laan, *The influence of water vapor on avalanches in air.* Journal of applied physics, 1984. **55**(9): p. 3286-3292.

19.   Gallimberti, I., *The mechanism of the long spark formation.* Le Journal de Physique Colloques, 1979. **40**(C7): p. C7-193-C7-250.

20.   Liu, S., S. Oshita, S. Kawabata, Y. Makino, and T. Yoshimoto, *Identification of ROS produced by nanobubbles and their positive and negative effects on vegetable seed germination.* Langmuir, 2016. **32**(43): p. 11295-11302.

21.   Vanraes, P., A. Nikiforov, M. Lessiak, and C. Leys. *Time-resolved characterization of a pulsed discharge in a stationary bubble*. in *Journal of Physics: Conference Series*. 2012. IOP Publishing.

22.   Bruggeman, P. and D.C. Schram, *On OH production in water containing atmospheric pressure plasmas.* Plasma Sources Science and Technology, 2010. **19**(4).

23.   Kanazawa, S., H. Tanaka, A. Kajiwara, T. Ohkubo, Y. Nomoto, M. Kocik, J. Mizeraczyk, and J.-S. Chang, *LIF imaging of OH radicals in DC positive streamer coronas.* Thin Solid Films, 2007. **515**(9): p. 4266-4271.

24.   Ono, R. and T. Oda, *Measurement of gas temperature and OH density in the afterglow of pulsed positive corona discharge.* Journal of Physics D: Applied Physics, 2008. **41**(3): p. 035204.

25.   Ono, R. and T. Oda, *OH radical measurement in a pulsed arc discharge plasma observed by a LIF method.* IEEE Transactions on Industry applications, 2001. **37**(3): p. 709-714.

26.   Schröter, S., A. Wijaikhum, A.R. Gibson, A. West, H.L. Davies, N. Minesi, J. Dedrick, E. Wagenaars, N. De Oliveira, and L. Nahon, *Chemical kinetics in an*

atmospheric pressure helium plasma containing humidity. Physical Chemistry Chemical Physics, 2018. **20**(37): p. 24263-24286.

27.   Bruggeman, P., G. Cunge, N.J.P.S.S. Sadeghi, and Technology, *Absolute OH density measurements by broadband UV absorption in diffuse atmospheric-pressure He–H2O RF glow discharges.* 2012. **21**(3): p. 035019.

28.   Laux, C.O., T. Spence, C. Kruger, and R. Zare, *Optical diagnostics of atmospheric pressure air plasmas.* Plasma Sources Science and Technology, 2003. **12**(2): p. 125.

29.   Du, Y., G. Nayak, G. Oinuma, Z. Peng, and P.J. Bruggeman, *Effect of water vapor on plasma morphology, OH and H2O2 production in He and Ar atmospheric pressure dielectric barrier discharges.* Journal of Physics D: Applied Physics, 2017. **50**(14): p. 145201.

30.   Verreycken, T., N. Sadeghi, and P.J. Bruggeman, *Time-resolved absolute OH density of a nanosecond pulsed discharge in atmospheric pressure He–H2O: absolute calibration, collisional quenching and the importance of charged species in OH production.* Plasma Sources Science and Technology, 2014. **23**(4): p. 045005.

31.   Verreycken, T., R. Van der Horst, A. Baede, E. Van Veldhuizen, and P. Bruggeman, *Time and spatially resolved LIF of OH in a plasma filament in atmospheric pressure He–H2O.* Journal of Physics D: Applied Physics, 2012. **45**(4): p. 045205.

32.   Luque, J., *LIFBASE, Database and spectral simulation for diatomic molecules.* SRI International Report, 1999. **99**.

33. Verreycken, T., R. Van Der Horst, N. Sadeghi, and P. Bruggeman, *Absolute calibration of OH density in a nanosecond pulsed plasma filament in atmospheric pressure He–H2O: comparison of independent calibration methods.* Journal of Physics D: Applied Physics, 2013. **46**(46): p. 464004.

34. Adamovich, I., S. Baalrud, A. Bogaerts, P. Bruggeman, M. Cappelli, V. Colombo, U. Czarnetzki, U. Ebert, J. Eden, and P. Favia, *The 2017 Plasma Roadmap: Low temperature plasma science and technology.* Journal of Physics D: Applied Physics, 2017. **50**(32): p. 323001.

35. Bruggeman, P. and C. Leys, *Non-thermal plasmas in and in contact with liquids.* Journal of Physics D: Applied Physics, 2009. **42**(5): p. 053001.

36. Liu, D.-X., P. Bruggeman, F. Iza, M.-Z. Rong, and M.G. Kong, *Global model of low-temperature atmospheric-pressure He+ H2O plasmas.* Plasma Sources Science and Technology, 2010. **19**(2): p. 025018.

37. Sakiyama, Y., D.B. Graves, H.-W. Chang, T. Shimizu, and G.E. Morfill, *Plasma chemistry model of surface microdischarge in humid air and dynamics of reactive neutral species.* Journal of Physics D: Applied Physics, 2012. **45**(42): p. 425201.

38. Wilson, A., D. Staack, T. Farouk, A. Gutsol, A. Fridman, and B. Farouk, *Self-rotating dc atmospheric-pressure discharge over a water-surface electrode: regimes of operation.* Plasma Sources Science and Technology, 2008. **17**(4): p. 045001.

39. Verreycken, T., D. Schram, C. Leys, and P. Bruggeman, *Spectroscopic study of an atmospheric pressure dc glow discharge with a water electrode in atomic and molecular gases.* Plasma Sources Science and Technology, 2010. **19**(4): p. 045004.

40. Xiong, Q., Z. Yang, and P.J. Bruggeman, *Absolute OH density measurements in an atmospheric pressure dc glow discharge in air with water electrode by broadband UV absorption spectroscopy.* Journal of Physics D: Applied Physics, 2015. **48**(42): p. 424008.

41. Itikawa, Y. and N. Mason, *Cross sections for electron collisions with water molecules.* Journal of Physical and Chemical reference data, 2005. **34**(1): p. 1-22.

42. Commission, U.S.N.R., *Standard Review Plan for Dry Cask Storage*. 1997, Office of Nuclear Material Safety and Safeguards: Washington, DC 20555-0001.

43. X. He, R.B., Y.-M. C. L. Pan, P. Shukla, K. Chiang, R. Pabalan, G. Willden and D. Vickers, *Available Methods for Functional Monitoring of Dry Cask Storage Systems*. 2014, U.S. Nuclear Regulatory Commission Contract NRC–HQ–12–C–02–0089.

44. Ren, Y., C. Wang, and Y. Qiu, *Aging of surface properties of ultra high modulus polyethylene fibers treated with He/O 2 atmospheric pressure plasma jet.* Surface and Coatings Technology, 2008. **202**(12): p. 2670-2676.

45. O'Connell, D., L. Cox, W. Hyland, S. McMahon, S. Reuter, W. Graham, T. Gans, and F. Currell, *Cold atmospheric pressure plasma jet interactions with plasmid DNA.* Applied Physics Letters, 2011. **98**(4): p. 043701.

46. Tian, L., H. Nie, N.P. Chatterton, C.J. Branford-White, Y. Qiu, and L. Zhu, *Helium/oxygen atmospheric pressure plasma jet treatment for hydrophilicity improvement of grey cotton knitted fabric.* Applied Surface Science, 2011. **257**(16): p. 7113-7118.

47.   H. S. Uhm, Y.C.H., *Various microplasma jets and their sterilization of microbes.* Thin Solid Films, 2011. **519**: p. 6974-6980.

48.   Fukuhara, D., S. Namba, K. Kozue, T. Yamasaki, and K. Takiyama, *Characterization of a Microhollow Cathode Discharge Plasma in Helium or Air with Water Vapor.* Plasma Science and Technology, 2013. **15**(2): p. 129-132.

49.   Yonemori, S., Y. Nakagawa, R. Ono, and T. Oda, *Measurement of OH density and air–helium mixture ratio in an atmospheric-pressure helium plasma jet.* Journal of Physics D: Applied Physics, 2012. **45**(22): p. 225202.

50.   Levko, D., A. Shuaibov, I. Shevera, R. Gritzak, and A. Tsymbaliuk, *Use of a low pressure helium/water vapor discharge as a mercury-free source of ultraviolet emission.* Journal of Applied Physics, 2014. **116**(11): p. 113303.

51.   Andrawes, F.F., *Determination of trace levels of water in gaseous samples by gas chromatography with helium ionization detection.* Analytical Chemistry, 1983. **55**: p. 1869-1872.

52.   S. Hanamura, B.K., J. D. Winefordner, *Determination of trace levels of water in solid samples by evolved gas analysis/helium microwave plasma emission spectrometry.* Analytical Chemistry, 1985. **57**: p. 9-13.

53.   Verreycken, T., R.M. van der Horst, A.H.F.M. Baede, E.M. Van Veldhuizen, and P.J. Bruggeman, *Time and spatially resolved LIF of OH in a plasma filament in atmospheric pressure He–H2O.* Journal of Physics D: Applied Physics, 2012. **45**(4): p. 045205.

54.	Liu, D.X., P. Bruggeman, F. Iza, M.Z. Rong, and M.G. Kong, *Global model of low-temperature atmospheric-pressure He + H 2 O plasmas.* Plasma Sources Science and Technology, 2010. **19**(2): p. 025018.

55.	Mayeresse, Y., R. Veillon, P. Sibille, and C. Nomine, *Freeze-drying process monitoring using a cold plasma ionization device.* PDA Journal of Pharmaceutical Science and Technology, 2007. **61**(3): p. 160.

56.	Sainct, F., D. Lacoste, M. Kirkpatrick, E. Odic, and C. Laux, *Experimental study of nanosecond repetitively pulsed discharges in water vapor.*

57.	Sainct, F.P., D.A. Lacoste, M.J. Kirkpatrick, E. Odic, and C.O. Laux, *Temporal evolution of temperature and OH density produced by nanosecond repetitively pulsed discharges in water vapour at atmospheric pressure.* Journal of Physics D: Applied Physics, 2014. **47**(7): p. 075204.

58.	Farouk, T., B. Farouk, D. Staack, A. Gutsol, and A. Fridman, *Simulation of dc atmospheric pressure argon micro glow-discharge.* Plasma Sources Science and Technology, 2006. **15**(4): p. 676.

59.	Knight, T.W., J. Khan, T. Farouk, J. Tulenko. *Experimental Determination of Used Fuel Vacuum Drying Using a Mock Fuel Assembly*. in *International High-Level Radioactive Waste Management Conference*. 2017. Charlotte, NC: American Nuclear Society.

60.	Shalloo, M., T. Knight, J. Khan, T. Farouk, J. Tulenko. *Vacuum Drying Experiments using a Mock Used Fuel Assembly*. in *Transactions Of the American Nuclear Society 2017 Winter Meeting*. 2017. Washington, DC: American Nuclear Society.

61.   Oleson, N.L. and A.W. Cooper, *Moving striations.* Advances in Electronics and Electron Physics, 1968. **24**: p. 155 - 278.

62.   Kolobov, V.I., *Striations in rare gas plasmas.* Journal of Physics D: Applied Physics, 2006. **39**(24): p. R487-R506.

63.   Golubovskii, Y.B., V. Nekuchaev, and A.Y. Skoblo, *Advances in the study of striations in inert gases.* Technical Physics, 2014. **59**(12): p. 1787-1800.

64.   Kolobov, V., *Glow Discharges: Stratification*, in *Encyclopedia of Plasma Technology*. 2016. p. 529-539.

65.   Liu, Y.X., E. Schungel, I. Korolov, Z. Donko, Y.N. Wang, and J. Schulze, *Experimental observation and computational analysis of striations in electrocnegative capacitively coupled radio-frequency plasmas.* Physical Review Letters, 2016. **116**: p. 255002.

66.   Gudmundsson, J.T. and A. Hecimovic, *Foundations of DC plasma sources.* Plasma Sources Science and Technology, 2017. **26**(12): p. 123001-1-20.

67.   Lisovskiy, V.A., V.A. Koval, E.P. Artushenko, and V.D. Yegorenkov, *Validating the Goldstein–Wehner law for the stratified positive column of dc discharge in an undergraduate laboratory.* European Journal of Physics, 2012. **33**(6): p. 1537-1545.

68.   Pollard, W., P. Suzuki, and D. Staack, *Striations in high-pressure hydrogen microplasma.* IEEE Transactions on Plasma Science, 2014. **42**(10): p. 2650-2651.

69.   Kawamura, E., M.A. Lieberman, and A.J. Lichtenberg, *Ionization instability induced striations in atmospheric pressure He/H2O RF and DC discharges.* Journal of Physics D: Applied Physics, 2017. **50**(14).

70. Goldstein, R.A., M.A. Huerta, and J.C. Nearing, *Stationary striations in an argon plasma as a bifurcation phenomenon.* Physics of Fluids, 1979. **22**(2).

71. Pekarek, L., *Ionization waves (striations) in a discharge plasma* Soviet Physics Uspekhi, 1968. **11**(2): p. 188.

72. Allis, W.P., *Review of glow discharge instabilities.* Physica B+C, 1976. **82**(1): p. 43- 51.

73. Nighan, W.L. and W.J. Wiegand, *Influence of negative-ion processes on steady-state properties and striations in molecular gas discharges.* Phyical Review A, 1974. **10**: p. 922-945.

74. Haas, R.A., *Plasma Stability of Electric Discharges in Molecular Gases.* Physical Review A, 1973. **8**(2): p. 1017-1043.

75. Arslanbekov, R.R. and V.I. Kolobov, *2-D Simulations of striations in direct current glow discharges in argon.* IEEE Transactions on Plasma Science 2005. **33**(2): p. 354-355.

76. Golubovskii, Y.B., A.Y. Skoblo, C. Wilke, R.V. Kozakov, J. Behnke, and V.O. Nekutchaev, *Kinetic resonances and stratification of the positive column of a discharge.* Phys Rev E Stat Nonlin Soft Matter Phys, 2005. **72**(2 Pt 2): p. 026414.

77. Golubovskii, Y.B., V.I. Kolobov, and V.O. Nekutchaev, *On electron bunching and stratification of glow discharges.* Physics of Plasmas, 2013. **20**: p. 101602.

78. Arslanbekov, R.R. and V.I. Kolobov, *Advances in simulations of moving striations in DC discharges of noble gases.* Physics of Plasmas, 2019. **26**(10).

79. Désangles, V., J.-L. Raimbault, A. Poyé, P. Chabert, and N. Plihon, *Pattern formation in low-pressure radio-frequency plasmas due to a transport instability.* Physical review letters, 2019. **123**(26): p. 265001.

80. Urbankova, H. and K. Rohlena, *Electron thermal diffusion instability and standing striations in the plasma of a dc discharge in molecular gases.* Czechoslovak Journal of Physics B, 1980. **30**: p. 1227 - 1235.

81. Mulders, H.C., W.J. Brok, and W.W. Stoffels, *Striations in a low-pressure RF-driven argon plasma.* IEEE transactions on plasma science, 2008. **36**(4): p. 1380-1381.

82. Liu, Y.-X., E. Schüngel, I. Korolov, Z. Donkó, Y.-N. Wang, and J. Schulze, *Experimental observation and computational analysis of striations in electronegative capacitively coupled radio-frequency plasmas.* Physical review letters, 2016. **116**(25): p. 255002.

83. Iza, F., S. Yang, H. Kim, and J.K. Lee, *The mechanism of striation formation in plasma display panels.* Journal of applied physics, 2005. **98**(4): p. 043302.

84. Levko, D. and L.L. Raja, *Magnetized direct current microdischarge I. Effect of the gas pressure.* Journal of Applied Physics, 2017. **121**(9): p. 093302.

85. Golubovskii, Y.B., V. Maiorov, I. Porokhova, and J. Behnke, *On the non-local electron kinetics in spatially periodic striation-like fields.* Journal of Physics D: Applied Physics, 1999. **32**(12): p. 1391.

86. Tsendin, L., *Electron kinetics in non-uniform glow discharge plasmas.* Plasma Sources Science and Technology, 1995. **4**(2): p. 200.

87.   Golubovskii, Y., S. Valin, E. Pelyukhova, V. Nekuchaev, and F. Sigeneger, *Discharge stratification in noble gases as convergence of electron phase trajectories to attractors.* Physics of Plasmas, 2016. **23**(12): p. 123518.

88.   Levko, D., *Electron kinetics in standing and moving striations in argon gas.* Physics of Plasmas, 2021. **28**(1): p. 013506.

89.   Sigeneger, F., G. Sukhinin, and R. Winkler, *Kinetics of the electrons in striations of spherical glow discharges.* Plasma Chemistry and Plasma Processing, 2000. **20**(1): p. 87-110.

90.   Mahamud, R. and T.I. Farouk, *Ion kinetics and self pulsing in DC microplasma discharges at atmospheric and higher pressure.* Journal of Physics D: Applied Physics, 2016. **49**(14): p. 145202.

91.   Farouk, T., B. Farouk, D. Staack, A. Gutsol, and A. Fridman, *Simulation of dc atmospheric pressure argon micro glow-discharge.* Plasma Sources Science and Technology, 2006. **15**(2006): p. 676-688.

92.   Kolobov, V.I., R.R. Arslanbekov, D. Levko, and V.A. Godyak, *Plasma stratification in radio-frequency discharges in argon gas.* Journal of Physics D: Applied Physics, 2020. **53**(25): p. 25LT01.

93.   Raizer, Y.P. and J.E. Allen, *Gas discharge physics*. Vol. 2. 1997: Springer Berlin.

94.   *COMSOL Multiphysics*, in *Multiphysics Reference Guide for COMSOL 5.5*. 2019: Burlington, MA, USA.

95.   Biagi, S.F., FORTRAN Program, MAGBOLTZ v8.97. Oct 2012.

96.   Alves, L. *The IST-LISBON database on LXCat*. in *Journal of Physics: Conference Series*. 2014. IOP Publishing.

97. Kushner, M., *Electron Impact Processes Hybrid Plasma Equipment Model*. Personal Communication.

98. Van Gaens, W. and A. Bogaerts, *Kinetic modelling for an atmospheric pressure argon plasma jet in humid air.* Journal of Physics D: Applied Physics, 2013. **46**(27): p. 275201.

99. Peterson, J., A. Le Padellec, H. Danared, G. Dunn, M. Larsson, A. Larson, R. Peverall, C. Strömholm, S. Rosén, and M. Af Ugglas, *Dissociative recombination and excitation of N 2+: Cross sections and product branching ratios.* The Journal of chemical physics, 1998. **108**(5): p. 1978-1988.

100. Sommerer, T.J. and M.J. Kushner, *Numerical investigation of the kinetics and chemistry of rf glow discharge plasmas sustained in He, N2, O2, He/N2/O2, He/CF4/O2, and SiH4/NH3 using a Monte Carlo-fluid hybrid model.* Journal of applied physics, 1992. **71**(4): p. 1654-1673.

101. Appleton, J., M. Steinberg, and D. Liquornik, *Shock-Tube Study of Nitrogen Dissociation using Vacuum-Ultraviolet Light Absorption.* The Journal of Chemical Physics, 1968. **48**(2): p. 599-608.

102. Billing, G.D. and E. Fisher, *VV and VT rate coefficients in N2 by a quantum-classical model.* Chemical Physics, 1979. **43**(3): p. 395-401.

103. Ahn, T., I.V. Adamovich, and W.R. Lempert, *Determination of nitrogen V–V transfer rates by stimulated Raman pumping.* Chemical Physics, 2004. **298**(1-3): p. 233-240.

104. Biagi, S.F., *Monte carlo simulation of electron drift and diffusion in counting gases under the influence of electic and magnetic field.* Nuclear Instruments and Methods in Physical Research Section A, 1999. **421**: p. 234 - 240.

105. Biagi, *www.LxCat.net*. retrieved on June 11, 2018.

106. IST-Lisbon, *www.LxCat.net*. retrieved on June 11, 2018.

107. Farouk, T., B. Farouk, A. Gutsol, and A. Fridman, *Atmospheric pressure methane–hydrogen dc micro-glow discharge for thin film deposition.* Journal of Physics D: Applied Physics, 2008. **41**(17): p. 175202.

108. Farouk, T., B. Farouk, and A. Fridman, *Computational studies of atmospheric pressure methane-hydrogen DC micro glow discharges.* IEEE Transactions on Plasma Science, 2010. **38**(2): p. 73 - 85.

109. White, R.D., R.E. Robson, B. Schmidt, and M.A. Morrison, *Is the classical two-term approximation of electron kinetic theory satisfactory for swarms and plasmas?* Journal of Physics D: applied physics, 2003. **36**(24): p. 3125.

110. Pitchford, L., S. ONeil, and J. Rumble Jr, *Extended Boltzmann analysis of electron swarm experiments.* Physical Review A, 1981. **23**(1): p. 294.

111. Pitchford, L. and A. Phelps, *Comparative calculations of electron-swarm properties in N 2 at moderate E N values.* Physical Review A, 1982. **25**(1): p. 540.

112. Dujko, S., A. Markosyan, R. White, and U. Ebert, *High-order fluid model for streamer discharges: I. Derivation of model and transport data.* Journal of Physics D: applied physics, 2013. **46**(47): p. 475202.

113.   Markosyan, A., S. Dujko, and U. Ebert, *High-order fluid model for streamer discharges: II. Numerical solution and investigation of planar fronts.* Journal of Physics D: Applied Physics, 2013. **46**(47): p. 475203.

114.   Stephens, J., *A multi-term Boltzmann equation benchmark of electron-argon cross-sections for use in low temperature plasma models.* Journal of Physics D: Applied Physics, 2018. **51**(12): p. 125203.

115.   Hagelaar, G. and L. Pitchford, *Solving the Boltzmann equation to obtain electron transport coefficients and rate coefficients for fluid models.* Plasma Sources Science and Technology, 2005. **14**(4): p. 722.

116.   Lisovskiy, V., V. Koval, E. Artushenko, and V. Yegorenkov, *Validating the Goldstein–Wehner law for the stratified positive column of dc discharge in an undergraduate laboratory.* European Journal of Physics, 2012. **33**(6): p. 1537.

117.   Cacciatore, M., M. Capitelli, and C. Gorse, *Non-equilibrium dissociation and ionization of nitrogen in electrical discharges: the role of electronic collisions from vibrationally excited molecules.* Chemical Physics, 1982. **66**(1-2): p. 141-151.

118.   Boeuf, J. and E. Kunhardt, *Energy balance in a nonequilibrium weakly ionized nitrogen discharge.* Journal of applied physics, 1986. **60**(3): p. 915-923.

119.   Yao, J., C. Yuan, S. Eliseev, A. Kudryavtsev, and Z. Zhou, *Longitudinal structure and plasma parameters of an entire DC glow discharge as obtained using a 1D fluid-based model with non-local ionization.* Plasma Sources Science and Technology, 2020. **29**(7).

120. Lisovskiy, V., V. Derevyanko, E. Artushenko, and V. Yegorenkov, *Stratification of the Positive Column of a DC Discharge in Nitrogen.* East European Journal of Physics, 2012(1017 (3)): p. 95-101.

121. Li, Y., R. Atif, K. Chen, J. Cheng, Q. Chen, Z. Qiao, G. Fridman, A. Fridman, and H.-F. Ji, *Polymerization of d-ribose in dielectric barrier discharge plasma.* Plasma, 2018. **1**(1): p. 144-149.

122. Na, Y.H., G. Park, E.H. Choi, and H.S. Uhm, *Effects of the physical parameters of a microwave plasma jet on the inactivation of fungal spores.* Thin solid films, 2013. **547**: p. 125-131.

123. Laurita, R., A. Miserocchi, M. Ghetti, M. Gherardi, A. Stancampiano, V. Purpura, D. Melandri, P. Minghetti, E. Bondioli, and V. Colombo, *Cold atmospheric plasma treatment of infected skin tissue: evaluation of sterility, viability, and integrity.* IEEE Transactions on Radiation and Plasma Medical Sciences, 2017. **1**(3): p. 275-279.

124. Yan, D., J.H. Sherman, and M. Keidar, *Cold atmospheric plasma, a novel promising anti-cancer treatment modality.* Oncotarget, 2017. **8**(9): p. 15977.

125. Laroussi, M., M. Kong, G. Morfill, and W. Stolz, *Plasma medicine: applications of low-temperature gas plasmas in medicine and biology.* 2012: Cambridge University Press.

126. Ercan, U.K., S.S. Joshi, A. Yost, S. O'Toole, M. Paff, E. Melchior, S.G. Joshi, and N. Gogotsi, *Inhibition of biofilms by non-thermal plasma treated novel solutions.* Advances in Microbiology, 2014. **4**(16): p. 1188.

127.   Fridman, G., M. Peddinghaus, M. Balasubramanian, H. Ayan, A. Fridman, A. Gutsol, and A. Brooks, *Blood coagulation and living tissue sterilization by floating-electrode dielectric barrier discharge in air.* Plasma Chemistry and plasma processing, 2006. **26**(4): p. 425-442.

128.   Kalghatgi, S.U., G. Fridman, M. Cooper, G. Nagaraj, M. Peddinghaus, M. Balasubramanian, V.N. Vasilets, A.F. Gutsol, A. Fridman, and G. Friedman, *Mechanism of blood coagulation by nonthermal atmospheric pressure dielectric barrier discharge plasma.* IEEE Transactions on plasma science, 2007. **35**(5): p. 1559-1566.

129.   Kalghatgi, S., G. Friedman, A. Fridman, and A.M. Clyne, *Endothelial cell proliferation is enhanced by low dose non-thermal plasma through fibroblast growth factor-2 release.* Annals of biomedical engineering, 2010. **38**(3): p. 748-757.

130.   Coulombe, S., V. Léveillé, S. Yonson, and R. Leask, *Miniature atmospheric pressure glow discharge torch (APGD-t) for local biomedical applications.* Pure and Applied Chemistry, 2006. **78**(6): p. 1147-1156.

131.   Shekhter, A.B., V.A. Serezhenkov, T.G. Rudenko, A.V. Pekshev, and A.F. Vanin, *Beneficial effect of gaseous nitric oxide on the healing of skin wounds.* Nitric oxide, 2005. **12**(4): p. 210-219.

132.   Smith, J.B., I. Adams, and H.-F. Ji, *Biomolecule response to nonthermal plasma.* Plasma Medicine, 2017. **7**(4).

133.   Alekseev, O., K. Donovan, V. Limonnik, and J. Azizkhan-Clifford, *Nonthermal dielectric barrier discharge (DBD) plasma suppresses herpes simplex virus type 1*

(HSV-1) replication in corneal epithelium. Translational vision science & technology, 2014. **3**(2): p. 2-2.

134. Kalghatgi, S., C.M. Kelly, E. Cerchar, B. Torabi, O. Alekseev, A. Fridman, G. Friedman, and J. Azizkhan-Clifford, *Effects of non-thermal plasma on mammalian cells.* PloS one, 2011. **6**(1): p. e16270.

135. Filipić, A., I. Gutierrez-Aguirre, G. Primc, M. Mozetič, and D. Dobnik, *Cold plasma, a new hope in the field of virus inactivation.* Trends in Biotechnology, 2020. **38**(11): p. 1278-1291.

136. Laroussi, M., I. Alexeff, and W.L. Kang, *Biological decontamination by nonthermal plasmas.* IEEE Transactions on Plasma Science, 2000. **28**(1): p. 184-188.

137. Lloyd, G., G. Friedman, S. Jafri, G. Schultz, A. Fridman, and K. Harding, *Gas plasma: medical uses and developments in wound care.* Plasma Processes and Polymers, 2010. **7**(3-4): p. 194-211.

138. Haque, M., M. Sartelli, J. McKimm, and M.A. Bakar, *Health care-associated infections–an overview.* Infection and drug resistance, 2018. **11**: p. 2321.

139. Fridman, G., G. Friedman, A. Gutsol, A.B. Shekhter, V.N. Vasilets, and A. Fridman, *Applied plasma medicine.* Plasma processes and polymers, 2008. **5**(6): p. 503-533.

140. Malyavko, A., D. Yan, Q. Wang, A.L. Klein, K.C. Patel, J.H. Sherman, and M. Keidar, *Cold atmospheric plasma cancer treatment, direct versus indirect approaches.* Materials Advances, 2020. **1**(6): p. 1494-1505.

141. Hong, Y., J. Kang, H. Lee, H. Uhm, E. Moon, and Y. Park, *Sterilization effect of atmospheric plasma on Escherichia coli and Bacillus subtilis endospores.* Letters in applied microbiology, 2009. **48**(1): p. 33-37.

142. Laroussi, M., C. Tendero, X. Lu, S. Alla, W.L.J.P.P. Hynes, and Polymers, *Inactivation of bacteria by the plasma pencil.* 2006. **3**(6-7): p. 470-473.

143. Shi, X.-M., G.-J. Zhang, X.-L. Wu, Z.-Y. Peng, Z.-H. Zhang, X.-J. Shao, and Z.-S. Chang, *Effect of low-temperature plasma on deactivation of hepatitis B virus.* IEEE Transactions on Plasma Science, 2012. **40**(10): p. 2711-2716.

144. Joshi, S.G., M. Paff, G. Friedman, G. Fridman, A. Fridman, and A.D. Brooks, *Control of methicillin-resistant Staphylococcus aureus in planktonic form and biofilms: a biocidal efficacy study of nonthermal dielectric-barrier discharge plasma.* American journal of infection control, 2010. **38**(4): p. 293-301.

145. Purevdorj, D., N. Igura, O. Ariyada, and I.J.L.i.a.m. Hayakawa, *Effect of feed gas composition of gas discharge plasmas on Bacillus pumilus spore mortality.* 2003. **37**(1): p. 31-34.

146. Hanbal, S.E., K. Takashima, S. Miyashita, S. Ando, K. Ito, M.M. Elsharkawy, T. Kaneko, and H. Takahashi, *Atmospheric-pressure plasma irradiation can disrupt tobacco mosaic virus particles and RNAs to inactivate their infectivity.* Archives of virology, 2018. **163**(10): p. 2835-2840.

147. Falkenstein, Z. and J.J.J.J.o.P.D.A.P. Coogan, *Microdischarge behaviour in the silent discharge of nitrogen-oxygen and water-air mixtures.* 1997. **30**(5): p. 817.

148. Maeda, Y., N. Igura, M. Shimoda, and I.J.A.b. Hayakawa, *Inactivation of Escherichia coli K12 using atmospheric gas plasma produced from humidified working gas.* 2003. **23**(4): p. 389-395.

149. Venezia, R.A., M. Orrico, E. Houston, S.-M. Yin, and Y.Y. Naumova, *Lethal activity of nonthermal plasma sterilization against microorganisms.* Infection Control & Hospital Epidemiology, 2008. **29**(5): p. 430-436.

150. Moldgy, A., G. Nayak, H.A. Aboubakr, S.M. Goyal, and P.J. Bruggeman, *Inactivation of virus and bacteria using cold atmospheric pressure air plasmas and the role of reactive nitrogen species.* Journal of Physics D: Applied Physics, 2020. **53**(43): p. 434004.

151. Schinköthe, J., H.A. Scheinemann, S. Diederich, H. Freese, M. Eschbaumer, J.P. Teifke, and S. Reiche, *Airborne Disinfection by Dry Fogging Efficiently Inactivates Severe Acute Respiratory Syndrome Coronavirus 2 (SARS-CoV-2), Mycobacteria, and Bacterial Spores and Shows Limitations of Commercial Spore Carriers.* Applied and Environmental Microbiology, 2021. **87**(3): p. e02019-20.

152. Rattanakul, S. and K. Oguma, *Inactivation kinetics and efficiencies of UV-LEDs against Pseudomonas aeruginosa, Legionella pneumophila, and surrogate microorganisms.* Water research, 2018. **130**: p. 31-37.

153. Zhang, C., Y. Li, C. Wang, and X. Zheng, *Different inactivation behaviors and mechanisms of representative pathogens (Escherichia coli bacteria, human adenoviruses and Bacillus subtilis spores) in g-C3N4-based metal-free visible-light-enabled photocatalytic disinfection.* Science of The Total Environment, 2021. **755**: p. 142588.

154. Gershman, S., M.B. Harreguy, S. Yatom, Y. Raitses, P. Efthimion, and G. Haspel, *A low power flexible dielectric barrier discharge disinfects surfaces and improves the action of hydrogen peroxide.* Scientific reports, 2021. **11**(1): p. 1-12.

155. Qazi, H., Q.-Y. Nie, H.-P. Li, X.-F. Zhang, and C.-Y. Bao, *Comparison of electrical and optical characteristics in gas-phase and gas-liquid phase discharges.* Physics of Plasmas, 2015. **22**(12): p. 123512.

156. Georgescu, N., C.P. Lungu, A.R. Lupu, and M. Osiac, *Atomic oxygen maximization in high-voltage pulsed cold atmospheric plasma jets.* IEEE transactions on plasma science, 2010. **38**(11): p. 3156-3162.

157. Ceriani, E., E. Marotta, V. Shapoval, G. Favaro, and C. Paradisi, *Complete mineralization of organic pollutants in water by treatment with air non-thermal plasma.* Chemical Engineering Journal, 2018. **337**: p. 567-575.

158. Ma, R., G. Wang, Y. Tian, K. Wang, J. Zhang, and J. Fang, *Non-thermal plasma-activated water inactivation of food-borne pathogen on fresh produce.* Journal of hazardous materials, 2015. **300**: p. 643-651.

159. Penetrante, B., M. Hsiao, J. Bardsley, B. Merritt, G. Vogtlin, A. Kuthi, C. Burkhart, and J. Bayless, *Identification of mechanisms for decomposition of air pollutants by non-thermal plasma processing.* Plasma sources science and technology, 1997. **6**(3): p. 251.

160. Baik, K.Y., H.L. Kang, J. Kim, S.Y. Park, J.Y. Bang, H.S. Uhm, E.H. Choi, and G. Cho, *Non-thermal plasma jet without electrical shock for biomedical applications.* Applied Physics Letters, 2013. **103**(16): p. 164101.

161. Kim, Y.H., Y.J. Hong, K.Y. Baik, G.C. Kwon, J.J. Choi, G.S. Cho, H.S. Uhm, D.Y. Kim, and E.H. Choi, *Measurement of reactive hydroxyl radical species inside the biosolutions during non-thermal atmospheric pressure plasma jet bombardment onto the solution.* Plasma Chemistry and Plasma Processing, 2014. **34**(3): p. 457-472.

162. Karuppiah, J., E.L. Reddy, P.M.K. Reddy, B. Ramaraju, R. Karvembu, and C. Subrahmanyam, *Abatement of mixture of volatile organic compounds (VOCs) in a catalytic non-thermal plasma reactor.* Journal of hazardous materials, 2012. **237**: p. 283-289.

163. Magureanu, M., N.B. Mandache, and V.I. Parvulescu, *Degradation of pharmaceutical compounds in water by non-thermal plasma treatment.* Water research, 2015. **81**: p. 124-136.

164. Vandenbroucke, A.M., R. Morent, N. De Geyter, and C. Leys, *Non-thermal plasmas for non-catalytic and catalytic VOC abatement.* Journal of hazardous materials, 2011. **195**: p. 30-54.

165. Verreycken, T. and P.J. Bruggeman, *OH density measurements in nanosecond pulsed discharges in atmospheric pressure N2–H2O mixtures.* Plasma Sources Science and Technology, 2014. **23**(1): p. 015009.

166. Bruggeman, P., D. Schram, M.Á. González, R. Rego, M.G. Kong, C.J.P.S.S. Leys, and Technology, *Characterization of a direct dc-excited discharge in water by optical emission spectroscopy.* 2009. **18**(2): p. 025017.

167. Dilecce, G., P. Ambrico, M. Simek, and S. De Benedictis, *LIF diagnostics of hydroxyl radical in atmospheric pressure He-H2O dielectric barrier discharges.* Chemical physics, 2012. **398**: p. 142-147.

168. Larsson, K., *Development of photofragmentation-based diagnostics*. 2018: Division of Combustion Physics, Department of Physics, Lund University.

169. Larsson, K., O. Johansson, M. Aldén, and J. Bood, *Simultaneous visualization of water and hydrogen peroxide vapor using two-photon laser-induced fluorescence and photofragmentation laser-induced fluorescence.* Applied Spectroscopy, 2014. **68**(12): p. 1333-1341.

170. Johansson, O., J. Bood, M. Aldén, and U. Lindblad, *Detection of hydrogen peroxide using photofragmentation laser-induced fluorescence.* Applied spectroscopy, 2008. **62**(1): p. 66-72.

171. Li, B., M. Jonsson, M. Algotsson, J. Bood, Z. Li, O. Johansson, M. Aldén, M. Tunér, and B. Johansson, *Quantitative detection of hydrogen peroxide in an HCCI engine using photofragmentation laser-induced fluorescence.* Proceedings of the Combustion Institute, 2013. **34**(2): p. 3573-3581.

172. Luque, J. and D.R. Crosley, *LIFBASE: Database and spectral simulation program (version 1.5).* SRI international report MP, 1999. **99**(009).

173. Aul, C.J., M.W. Crofton, J.D. Mertens, and E.L. Petersen, *A diagnostic for measuring H2O2 concentration in a shock tube using tunable laser absorption near 7.8 μm.* Proceedings of the Combustion Institute, 2011. **33**(1): p. 709-716.

APPENDIX A

TRANSITIONS IN HE-H$_2$O PLASMA

Table A.1 Prominent spectral lines in the optical emission spectrum of humid helium

Species	Wavelength(nm)	Transition
From H₂O		
OH	282.8	0.06
OH	309.0	1.13
O	777.4	37.50
O	844.6	9.27
O	926.3	3.60
H	486.1	0.13
H	656.3	4.62
From He		
He	388.9	0.87
He	447.1	0.14
He	501.6	1.78
He	587.6	11.45
He	667.8	18.80
He	706.5	100.00
He	728.1	16.46
He	1083.0	28.10

APPENDIX B

LIST OF INSTRUMENTS

Table B.1 Catalogue of Instruments used

Instrument	Make	Accuracy
Mass flow controller(s)	MKS	± 1% of F.S.
Vacuum pump	Agilent IDP-15 dry scroll pump	N/A
Pressure gauge	Teledyne Hastings 760s	+/-(0.3% of Reading + 1 Torr) for P<$\leq$ 760 Torr
Cathode ray oscilloscope	Agilent Technologies InfiniiVision MSO7054B	DC vertical gain accuracy: ± 2.0% full scale DC vertical offset accuracy: $\leq$ 200 mV/div: ± 0.1 div ± 2.0 mV ± 0.5% offset value > 200 mV/div: ± 0.1 div ± 2.0 mV ± 1.5% offset value Resolution: 2.5 ps
High voltage probe	North Star PVM-4	DC - 2 Hz: < 0.1% 2 Hz. - 200 Hz.: < 1.5 % 200 Hz. - 5 Mhz.: < 2% > 5 Mhz.: < 5%
Optical emission spectrometer	Ocean Optics HR4000CG-UV-NIR	Signal-to-noise ratio: 300:1 (at full signal) Optical resolution: <1.0 nm FWHM
Optical fiber	QP450-2-XSR	N/A
Syringe	Hamilton 10 ml	N/A
Syringe pump	KD Scientific KDS 200	Accuracy: ± < 1%

APPENDIX C

REACTION KINETICS IN N$_2$ PLASMA

Table C.1 List of N_2 reactions considered in the EEDF calculation. Cross-section data are from [95, 105]

#	Reaction
01	$e + N_2 \rightarrow e + N_2$
02	$e + N_2 \rightarrow e + N_{2,v=1}$
03	$e + N_2 \rightarrow e + N_{2,v=2}$
04	$e + N_2 \rightarrow e + N_{2,v=3}$
05	$e + N_2 \rightarrow e + N_{2,v=4}$
06	$e + N_2 \rightarrow e + N_{2,v=5}$
07	$e + N_2 \rightarrow e + N_{2,v=6}$
08	$e + N_2 \rightarrow e + N_{2,v=7}$
09	$e + N_2 \rightarrow e + N_{2,v=8}$
10	$e + N_2 \rightarrow e + N_{2,v=9}$
11	$e + N_2 \rightarrow e + N_{2,v=10}$
12	$e + N_2 \rightarrow e + N_{2,v=11}$
13	$e + N_2 \rightarrow e + N_{2,v=12}$
14	$e + N_2 \rightarrow e + N_{2,v=13}$
15	$e + N_2 \rightarrow e + N_{2,v=14}$
16	$e + N_2 \rightarrow e + N_{2,v=15}$
17	$e + N_2 \rightarrow e + N_2(A^3\Sigma, v = 0 - 4)$
18	$e + N_2 \rightarrow e + N_2(A^3\Sigma, v = 5 - 9)$
19	$e + N_2 \rightarrow e + N_2(B^3\Pi, v = 0 - 3)$
20	$e + N_2 \rightarrow e + N_2(W^3\Delta, v = 0 - 5)$
21	$e + N_2 \rightarrow e + N_2(A^3\Sigma, v = 10 - 21)$
22	$e + N_2 \rightarrow e + N_2(B^3\Pi, v = 4 - 16)$
23	$e + N_2 \rightarrow e + N_2(W^3\Delta, v = 6 - 10)$
24	$e + N_2 \rightarrow e + N_2(A^1\Pi, v = 0 - 3)$
25	$e + N_2 \rightarrow e + N_2(B!^3\Sigma, v = 0 - 6)$
26	$e + N_2 \rightarrow e + N_2(A!^1\Sigma, v = 0 - 6)$
27	$e + N_2 \rightarrow e + N_2(W^3\Delta, v = 11 - 19)$
28	$e + N_2 \rightarrow e + N_2(W^1\Delta, v = 0 - 5)$
29	$e + N_2 \rightarrow e + N_2(A^1\Pi, v = 4 - 15)$
30	$e + N_2 \rightarrow e + N_2(B!^3\Sigma, v = 7 - 18)$
31	$e + N_2 \rightarrow e + N_2(A!^1\Sigma, v = 7 - 19)$
32	$e + N_2 \rightarrow e + N_2(W^1\Delta, v = 6 - 18)$
33	$e + N_2 \rightarrow e + N_2(C^3\Pi, v = 0 - 4)$
34	$e + N_2 \rightarrow e + N_2(E^3\Sigma)$
35	$e + N_2 \rightarrow e + N_2(A!!^1\Sigma, v = 0 - 1)$
36	$e + N_2 \rightarrow e + N_2(B^1\Pi, v = 0 - 6)$
37	$e + N_2 \rightarrow e + N_2(C!^1\Sigma, v = 0 - 3)$
38	$e + N_2 \rightarrow e + N_2(G^3\Pi, v = 0 - 3)$
39	$e + N_2 \rightarrow e + N_2(C^{3\ 1}\Pi, v = 0 - 3)$
40	$e + N_2 \rightarrow e + N_2(F^3\Pi, v = 0 - 3)$
41	$e + N_2 \rightarrow e + N_2(B!^1\Sigma, v = 0 - 10)$

42	$e + N_2 \rightarrow e + N_2(B^1\Pi, v = 7 - 14)$
43	$e + N_2 \rightarrow e + N_2(O^{3\,1}\Pi, v = 0 - 3)$
44	$e + N_2 \rightarrow e + N_2(B!^{3\,1}\Sigma, v = 10 - H)$
45	$e + N_2 \rightarrow e + N_2(\text{sum singlets})$
46	$e + N_2 \rightarrow 2e + N_2^+$

Table C.2 List of N reactions considered in the EEDF calculation. Cross-section data are from [96, 106]

Process	Reaction
01	$e + N \rightarrow e + N$
02	$e + N \rightarrow e + N(2D)$
03	$e + N \rightarrow e + N(2P)$
04	$e + N \rightarrow 2e + N^+$

C.1 REFERENCES

95.   Biagi, S.F., FORTRAN Program, MAGBOLTZ v8.97. Oct 2012.

96.   Alves, L. *The IST-LISBON database on LXCat*. in *Journal of Physics: Conference Series*. 2014. IOP Publishing.

105.   Biagi, *www.LxCat.net*. retrieved on June 11, 2018.

106.   IST-Lisbon, *www.LxCat.net*. retrieved on June 11, 2018.

APPENDIX D

ACADEMIC VITAE

MALIK MOHAMMAD TAHIYAT

Contact: mtahiyat@cec.sc.edu; malik_tahiyat_bd@outlook.com;
https://www.linkedin.com/in/mtahiyat/

Education

Ph.D. Mechanical Engineering   03/2022
University of South Carolina, SC, USA
Dissertation title: Characterization of Nonequilibrium Plasma
                        Discharge in High Water Vapor Concentration
Academic Advisor: Tanvir I Farouk, Ph.D.

M.Sc. Chemical Engineering   08/2015
Bangladesh University of Engineering and Technology
Thesis title: Data-Based Quantification of Process Nonlinearity
Academic Advisor: Md. Ali Ahammad Shoukat Choudhury, Ph.D.

B.Tech. Chemical Engineering   11/2011
West Bengal University of Technology

Research Interests

Experimental Plasma Physics	Plasma Instabilities Modeling	Laser diagnostics
Reactor Design	Process Control	Process Nonlinearity Analysis

Honors Society Affiliation
      Pi-Tau-Sigma-Theta-Tau Honors society, Mechanical Engineering, U of SC

Grants and Awards
Visiting Researcher-ship
      Advanced Imaging Lab, CRF, Sandia National Laboratories (10/2021-12/2021)
Presidential Fellowship
      U of SC Graduate School (2015-2019)
Conference Travel Grants
      GEC (2018, 2019, 2021)
      U of SC Graduate School (2018, 2019)
Graduate Student Research Grant
      U of SC Office of the Vice President for Research (SPARC, 2019-2020)
      Hamilton Syringe Grant (2016)
Scholarships
      Michael and Ann Sutton Research Scholarship, 2021
      Bangladesh Chemical Engineering Forum, 2014

List of Publications

1. **Malik Tahiyat**, Jacob Stephens, Vladimir Kolobov, and Tanvir Farouk. '*Striations in moderate pressure dc driven nitrogen glow discharge*' (J. Phys. D: Appl. Phys., 55 (2022) 085201)

2. Shamia Hoque, **Malik M Tahiyat**, Nouf Z Abbas, Sudipta Saha, Nicole D Berge, Tanvir I Farouk. '*Atmospheric pressure dielectric barrier discharge for siloxane reformation*' (J. Phys. D: Appl. Phys. 53 (2020) 015202)

3. **Malik M Tahiyat***, Ibrahim Sarikaya*, Ramy Harik, Tanvir Farouk, and John Connell. '*Surface functionalization of automated fiber placement manufactured composites by atmospheric pressure plasma jet*' (International Journal of Adhesion and Adhesives, 99, (2020), 102570 (* equally contributed)

4. **MM Tahiyat**, TW Knight, T Farouk. '*Note: Plasma optical emission spectroscopy for water vapor quantification and detection during vacuum drying process*' (Review of Scientific Instruments, 89, (2018), 116108)

5. Mohammad Aminul Islam Khan, **Malik M. Tahiyat**, Syed Ahmad Imtiaz, Faisal Khan, M.A.A Shoukat Choudhury. '*Experimental evaluation of control performance of MPC as a regulatory controller*' (ISA Transactions, 70, (2017), 512-520)

6. **Malik M Tahiyat**, Dirk van den Bekerom, Erxiong Huang, Jonathan H Frank, and Tanvir I Farouk. '*Absolute OH and H_2O_2 density measurements in nanosecond pulsed He-H_2O and He-H_2O-O_2 in near atmospheric pressure dielectric barrier discharge afterglow by photo-fragmentation laser-induced fluorescence*' (in works)

7. **Malik M Tahiyat**, Nathan A Ramanjulu, Yvonne Hui, Tanvir I Farouk, Traci L Testerman, and Shamia Hoque. '*Application of Dielectric Barrier Discharge in Misty Plasma systems for disinfection of surfaces and equipment in health settings*' (in works)

List of Patents

1. Shamia Hoque, Tanvir Farouk, **Malik Tahiyat**. '*Siloxane removal off landfill gas using dielectric barrier discharge plasma*', US Patent# US20210093999A1, 2021

2. Tanvir Farouk, **Malik Tahiyat**, Travis Knight. '*Water vapor quantification methodology during drying of spent nuclear fuel*', US Patent# US20200135350A1, 2020

3. **Malik Tahiyat**, Tanvir Farouk, Traci Testerman, Shamia Hoque, '*Misty Plasma Dielectric Barrier Discharge Plasma System for Disinfection*' (in works)

4. **Malik Tahiyat**, Tanvir Farouk, '*Dielectric Barrier Discharge Humid Plasma System for in-situ Hydrogen Peroxide Production*' (in works)